Combustion in Radiant Tube Heaters

Numerical and Parametric Studies

Prashant R. Mewani

Technische Universiteit Delft

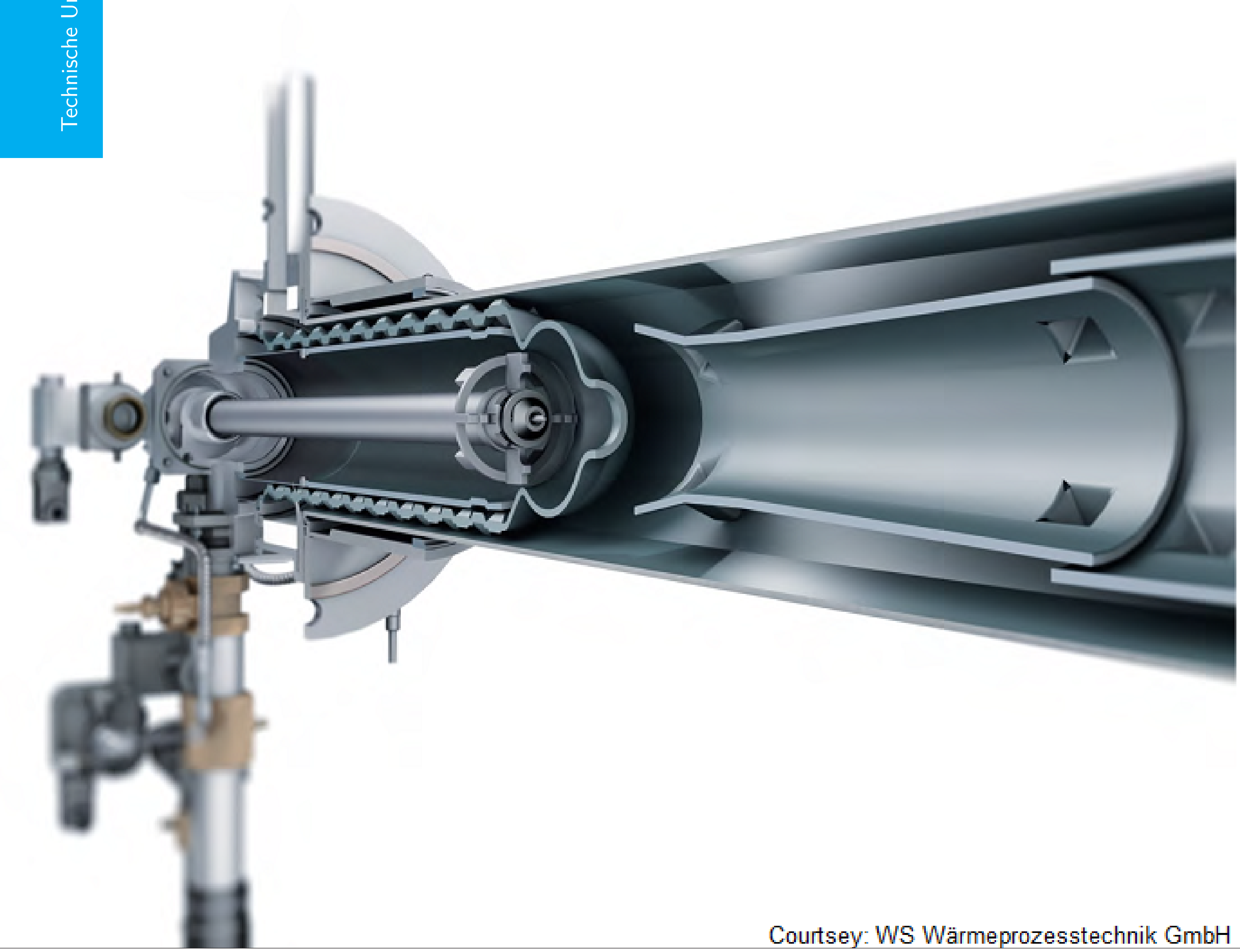

Courtsey: WS Wärmeprozesstechnik GmbH

Delft University of Technology

Challenge the future

COMBUSTION IN RADIANT TUBE HEATERS

NUMERICAL AND PARAMETRIC STUDIES

by

Prashant R. Mewani

in partial fulfillment of the requirements for the degree of

Master of Science
in Sustainable Energy Technology

at the Delft University of Technology,
to be defended publicly on Tuesday August 21, 2018 at 02:00 PM.

Student number:	4517075	
Supervisor:	Prof. dr. ir. Wiebren de Jong,	Delft University of Technology
Thesis committee:	Prof. dr. D. J. E. M. Roekaerts,	Delft University of Technology
	Dr. A. Gangoli Rao,	Delft University of Technology
	Ir. Mara del Grosso,	Delft University of Technology

ACKNOWLEDGEMENT

It would be unfair to say that this thesis is completely mine, as any scientific project of such scale is impossible for one person to complete alone. Hence, I would like to take this opportunity to thank various people for their help, guidance, mentorship and support during the course of this thesis.

First of all, I express deep gratitude to my supervisors Prof. dr. ir. Wiebren de Jong and Prof. dr. D. J. E. M. Roekaerts for their constant guidance, feedback and the freedom they gave me during to decide the course of this thesis. I am quite fortunate to work under their supervision.

I would also like to thank my daily supervisor Mara del Grosso for her constant support and patience for helping me throughout this thesis. She has been instrumental in shaping it into its current form. I also appreciate the time she has spent on reading and correcting the drafts of this report, for it would have been impossible for me to complete it without her endless help.

Additionally, I would like to thank Dr. Arvind Gangoli Rao for agreeing to join my graduation committee and for taking time to read this report.

I would also like to thank my friends for their company. I have enjoyed my stay in this country because of their friendship. They have helped me through tough times and have constantly cheered me whenever I got low. I surely have made some fond colourful memories of our times together.

Last, but not the least, I would like to thank my family for always being there for me. They form the foundation of my life, have always supported me and encouraged me to take independent decisions, including the one to pursue higher education at this university. I realise how tough it has been for them to send me thousands of miles away but they have respected my decision and I can only be grateful to them for understanding me, my dreams and my aspirations.

Prashant R. Mewani
Delft, August 15, 2018

ABSTRACT

The Process and Energy department of the Mechanical, Maritime and Materials faculty of TU Delft and the Dutch company Petrogas Gas-Systems B.V. are working together on the commissioning of a small 50 kW_{th} Indirectly Heated Bubbling Fluidised Bed Steam Reformer (IHBFBSR) which will be used to gasify the energy crop Miscanthus. However, the new feature is that this fluidised bed will be heated indirectly using radiant tube heaters installed in the reactor. These heaters are made by assembling radiant tubes with self-recuperative burners fired using Dutch Natural Gas. All the tubes and burners have been manufactured by the German company WS Wärmeprozesstechnik GmbH. This thesis consists of the study of two such distinct burner-tube assemblies, both of different heating capacity. The smaller capacity is of the C80 burner assembled with C100 tube while the larger is of the C100 burner assembled with C150 tube. The heat transfer and fluid dynamics inside both the tubes have been numerically modelled using CFD techniques. The models of the burners have been done using the commercially available software ANSYS® Fluent version 18.2.

The main objective of this thesis has been to analyse the heat transfer from both the assemblies and calculation of their respective efficiency. To this end, the temperature, velocity, species and turbulence fields have been calculated for inside both the tubes. Also, the total heat output from the radiant tubes has been calculated. However, the mechanism of heat transfer from the radiant tube to the fluidised bed was not known at the time of these calculations. Hence, appropriate boundary conditions have been used to simulate the outer environment. The total heat transfer from the combusting flow to the inner surface of the radiant tube has been calculated. This total heat input has been equated to heat transfer from the outer surface of the tube to the fluidised bed, assuming steady state condition. The variation of all these parameters has been studied with air factor and preheat temperature. The air factor has been varied from 1.0 to 1.5 for both tubes, by reducing the fuel inlet keeping the air inlet constant. The air preheat temperature has been varied from 300°C to 700°C for C80-C100 assembly and from 300°C to 800°C for C100-C150 assembly. This has been done to calculate an optimum operating condition for both the burner-tube assemblies in terms of maximising heat transfer and radiant tube efficiency and minimising fuel wastage. It has been found that operating at lean condition of 20% excess air by mass at highest air preheat temperature would be the optimum operating condition.

The last part of this thesis is the analysis of the robustness of calculations. Three grid sizes have been chosen other than the main grid and all the parameters have been checked for variations, if any. The variation is found to be within scientifically acceptable limits. Hence, it is concluded that the calculations are robust at this level.

Prashant R. Mewani
Delft, August 15, 2018

CONTENTS

LIST OF FIGURES

LIST OF TABLES

NOMENCLATURE

Abbreviations

BFB	Bubbling Fluidised Bed
Btu	British thermal units
CARS	Coherent anti-Stokes Raman Spectroscopy
CFB	Circulating Fluidised Bed
CFD	Computational Fluid Dynamics
CMC	Conditional Moment Closure
CV	Control Volume
DNS	Direct Numerical Simulation
DO	Discrete Ordinates
DTRM	Discrete Transfer Radiation Method
EDC	Eddy Dissipation Concept
EF	Entrained Flow
IHBFBSR	Indirectly Heated Bubbling Fluidised Bed Steam Reformer
ISAT	In-Situ Adaptive Tabulation
LES	Large Eddy Simulation
LHS	Left Hand Side
MC	Monte Carlo
OECD	Organisation for Economic Co-operation and Development
pdf	probability density function
PV	Photovoltaics
RANS	Reynolds Averaged Navier-Stokes
RHS	Right Hand Side
RNG	Renormalisation Group
RTE	Radiative Transport Equation
SiSiC	Siliconized Silicon Carbide
SST	Shear Stress Transport

TFC	Turbulent Flame Closure
WSGGM	Weighted Sum of Grey Gases Model

English symbols

C	Constant depending upon context given	[-]
C_f	Fanning friction factor	[-]
C_μ	Model constant for turbulent viscosity	[-]
$c_{p,k}$	Specific heat at constant pressure for species k	J/(kg.K)
D	Representative diffusion coefficient	m^2/s
D_k	Diffusion coefficient for species k into the rest of the mixture	m^2/s
Da	Damköhler number	[-]
E	Total energy	J/kg
ER	Equivalence ratio	[-]
F	Blending function	[-]
h	Enthalpy	J/kg
I/I_b	Radiative intensity/Blackbody radiative intensity	$W/(m^2.sr)$
k	Turbulent kinetic energy	m^2/s^2
K_{eq}	Equilibrium constant	depending upon context
l_m	Mixing length	m
l_{pk}	Characteristic length for Prandtl Kolmogorov model	m
l_t	Turbulent length scale	m
$\dot{m}$	Mass flow rate	kg/s
p	Pressure	Pa
$p(z)$	Probability density function (pdf) for mixture fraction	[-]
$p(z,\chi)$	Joint pdf for mixture fraction and scalar dissipation rate	s
q	Heat flux	W/m^2
$\dot{Q}$	Power in the specified context	W
Re	Reynolds number	[-]
Re_{crit}	Critical Reynolds number	[-]
Re_D	Reynolds number calculated using hydraulic diameter	[-]
Re_t, Re_y	Turbulent Reynolds number	[-]

s_{ij}	individual strain rate in plane i in direction j	1/s
S_{ij}	Mean strain rate tensor constructed using individual strain rates	1/s
S_M	Body force	N/m^3
s_M	Term analogous to body forces	N/m^3
S_{tot}	Total force	N/m^3
Sc_{kt}	Turbulent Schmidt number for species k	[-]
T	Temperature	K
u	Velocity in x-direction	m/s
U^*	[-] velocity	[-]
u_i	Velocity in i-th direction	m/s
u_∞	Mean bulk velocity	m/s
u_τ	Velocity calculated using wall viscous stress	m/s
v	Velocity in y-direction	m/s
$V_{k,i}$	Diffusion velocity for species i	m/s
w	Velocity in z-direction	m/s
Y_k	Mass fraction of species k	[-]
y^+, y^*	[-] distance from wall	[-]
z	Mixture fraction	[-]

Greek symbols

α^*	Damping coefficient for low-Reynolds numbers	[-]
α_ε	Inverse Prandtl number for turbulent dissipation rate	[-]
α_k	Inverse Prandtl number for turbulent kinetic energy	[-]
β	Extinction coefficient	1/m
χ	Scalar dissipation rate	1/s
$\dot{\omega}_k$	Chemical reaction rate for species k	$kg/(m^3.s)$
$\dot{\omega}_T$	Heat release rate caused by combustion	$J/(m^3.s)$
ϵ	Emissivity	[-]
κ	Absorption coefficient	1/m
λ	Thermal conductivity	W/(m.K)
λ	Volumetric deformation rate constant	kg/(m.s)

μ	Dynamic viscosity	kg/(m.s)
μ_{eff}	Effective turbulent viscosity	kg/(m.s)
μ_t	Turbulent viscosity	kg/(m.s)
ν	Kinematic viscosity	m^2/s
ω	Turbulent specific dissipation rate	1/s
Ω_{ij}	Vorticity tensor	1/s
ϕ	General flow property	
$\Phi(\mathbf{s}_i,\mathbf{s})$	Scattering phase function	[-]
ρ	Density	kg/m^3
σ	Stefan-Boltzmann constant	W/(m^2.K^4)
σ_ε	Turbulent Prandtl number for turbulent dissipation rate	[-]
σ_k	Turbulent Prandtl number for turbulent kinetic energy	[-]
σ_s	Scattering coefficient	1/m
τ^*	Time scale at fine scale	s
τ_c	Chemical time scale	s
τ_f	Flow time scale	s
τ_{ij}	Viscous stress tensor	kg/(m.s^2)
τ_{wall}	Wall viscous stress	kg/(m.s^2)
$\tilde{\nu}$	Conserved quantity in Spalart-Allmaras model	m^2/s
ε	Turbulent dissipation rate	m^2/s^3
ε_h	Dilatational turbulent dissipation rate	m^2/s^3
ε_s	Solenoidal turbulent dissipation rate	m^2/s^3
ξ^*	Length fraction at fine scales	[-]

Mathematical symbols

Δt	Incremental time	s
δx	Incremental distance in x-direction	m
δy	Incremental distance in y-direction	m
δz	Incremental distance in z-direction	m
δ_{ij}	Kronecker delta function	[-]
$\Gamma(x)$	Gamma function	[-]

$B(a,b)$	Normalisation factor	[-]
t	Time	s
x	Distance in x-direction	m
x_i	Distance in i-th direction	m
y	Distance in y-direction	m
z	Distance in z-direction	m

Subscripts

i	i-th component
j	j-th component
k	Species k
max	Maximum value of the quantity
min	Minimum value of the quantity
s	Sensible component of the quantity
ref	Reference value of the quantity
P	Product species P
$\mathscr{R}$	Reactant species $\mathscr{R}$

Superscripts

–	Reynolds decomposition mean value
~	Favre averaged mean value
$'$	Reynolds decomposition fluctuation
$''$	Favre decomposition fluctuation
$*$	Fine structures
$\cdot$	Rate of the quantity

1

INTRODUCTION

In this rapidly changing world, one of the top challenges that humanity faces is the conversion of sufficient energy into useful form and its equitable distribution to all the people. The total world energy consumption was estimated to be 575 quadrillion British thermal units (Btu) in 2015 and it is expected to rise by 28% to 736 quadrillion Btu by 2040 [78]. The contribution from renewable sources of energy are expected to rise rapidly at a rate of 2.3% per year from 2015 to 2040. However, even by 2040 fossil fuels will remain the major source of world energy supply with a contribution of approximately 77% to the global consumption [78]. Natural gas is expected to grow rapidly at 1.4% per year during that period, which can be attributed to large natural gas reserves and rising production facilities including tight gas, shale gas and coalbed methane. It is predicted that liquid fossil fuels will be the largest source of energy supply till 2040, at which point natural gas will become the second largest source [78]. However, the demand for coal is expected to remain constant during this period owing to many countries reducing their usage switching over to natural gas, renewables and nuclear power (in case of China) [78]. The total projections from different energy sources are shown in Figure (1.1):

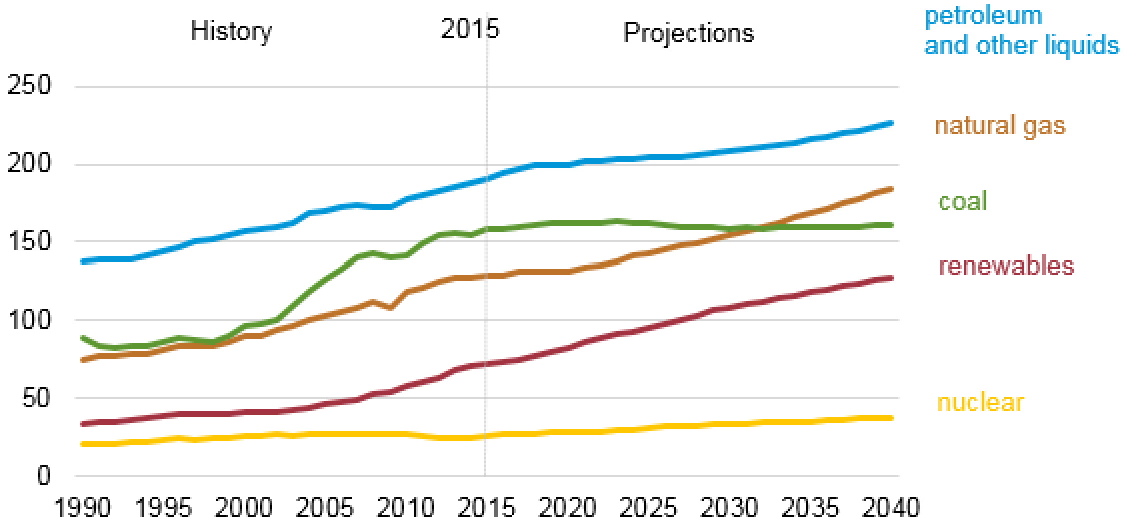

Figure 1.1: World energy consumption by energy source (quadrillion Btu) [78]

1.1. RENEWABLE ENERGY SOURCES

The population of the world in 2015 was estimated to be 7349472000 [77]. Thus, even at the global consumption rate of 2015, the average consumption should have been approximately 78.24 million Btu per person. However, it was estimated that approximately 1.2 billion people (about 16% of the global population) were living without electricity and approximately 2.7 billion people (about 38% of the global population) lack access to clean cooking facilities in that year [66]. This inequality provides incentive to tap into the renewable sources of energy, rather than depending on just conventional fossil fuels. The share of various sources for the year 2015 is shown in Figure (1.2):

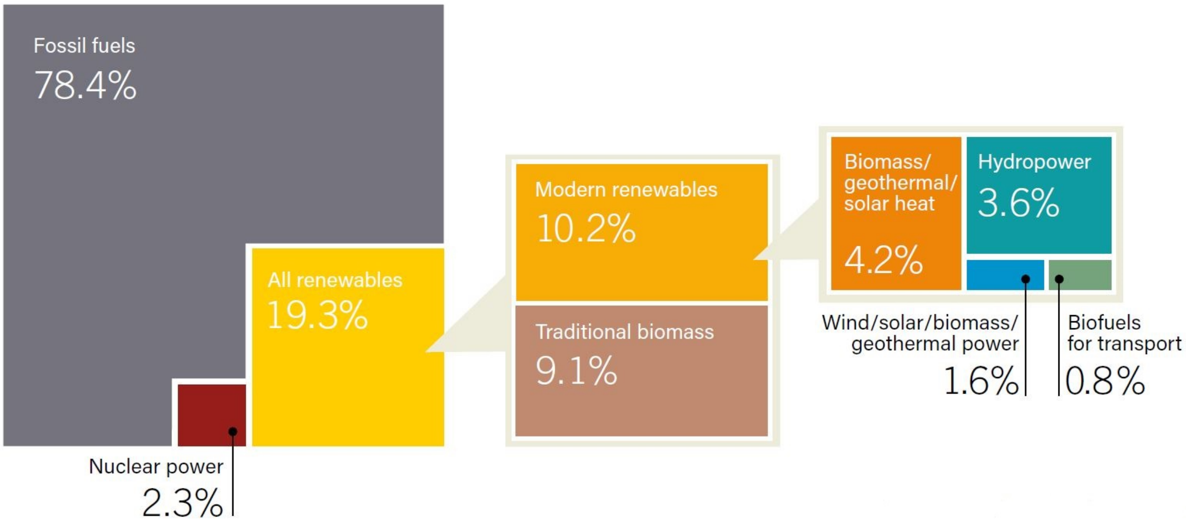

Figure 1.2: Share of various energy sources in 2015 [66]

It can be seen that fossil fuels form the major contribution to the global final energy consumption while renewables contribute only 19.3%. The overall share of renewables is expected to increase modestly till 2040 because the overall energy demand is expected to rise significantly. However, the increase in the renewable capacity is appreciable throughout till 2040. The power sector experienced the greatest increase in renewable energy capacity in 2016. Renewables contributed 62% of the added global power generating capacity in that year. The maximum contribution has been from solar PV, followed by wind energy and hydro-power. Traditional biomass sources supplied around 9% of the global heat demand, followed by solar thermal and geothermal sources. The transport sector was dominated by fossil fuels. However, small contributions from liquid biofuels were recorded. In 2016, they provided around 4% of world road transport fuels, which account for majority of transport energy use. The use biogas for transportation has increased in the United States and Europe, while being limited in other regions. Electrification of transport sector has expanded. This is due to increase in the share of renewables in electrified transport as the share of renewables in grid power increases. However, the policy support to renewable energy in transport sector is less than that in power sector [66].

1.1.1. RENEWABLE POWER GENERATION

A major portion of the global power capacity is still composed of non-renewable sources. By the end of 2016, 75.5% of total global capacity was composed of non-renewables, the rest 24.5% of renewable sources. However, the new capacity addition is dominated by renewable sources. The total renewable global capacity increased by approximately 9% as compared to 2015 and reached almost 2017 GW by the end of 2016 with an estimated 161 GW of capacity added in 2016 itself. Within the newly added renewable power capacity, solar PV represents the largest share of about 47%, followed by wind and hydropower at 34% and 15.5% respectively [66]. The contribution of various sources to total global power capacity by the end of 2016 is shown in Figure (1.3).

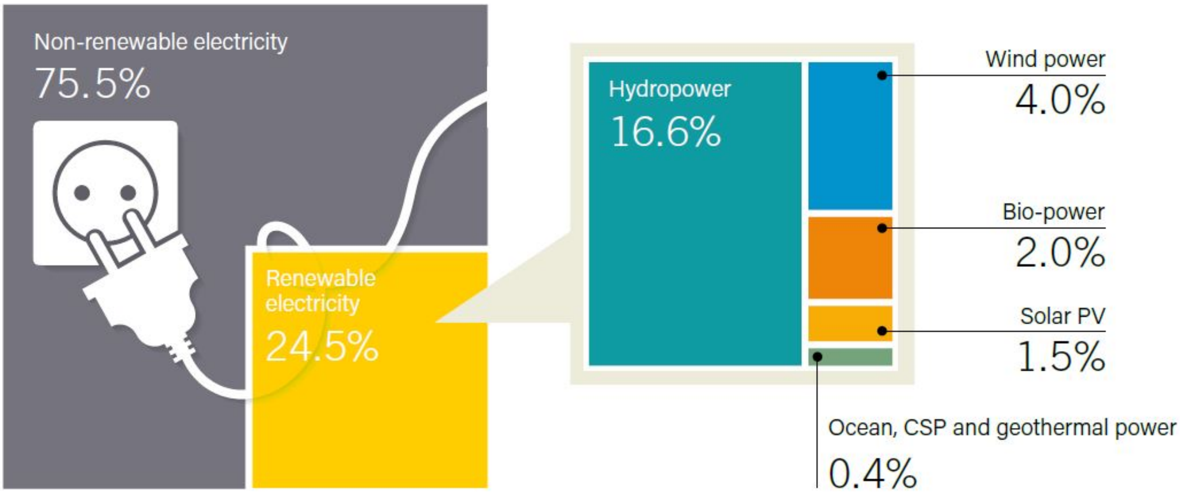

Figure 1.3: Global electricity production at 2016 end [66]

The global electricity generation was estimated to be 23.4 trillion kWh in 2015 and is expected to increase by 45% to 34.0 trillion kWh by 2040. The major growth is expected in non-OECD Asian countries where electricity generation increases by 1.9% per year, as living standards rise continuously. In OECD nations, the increase is relatively slower at about 1.0% per year. The share of renewable sources in electricity generation is expected to rapidly rise at 2.8% till 2040 [78]. However, the share of non-renewable sources is not expected to fall, as the global demand rises. The estimation of contribution of various sources of electricity generation till 2040 is presented in Figure (1.4).

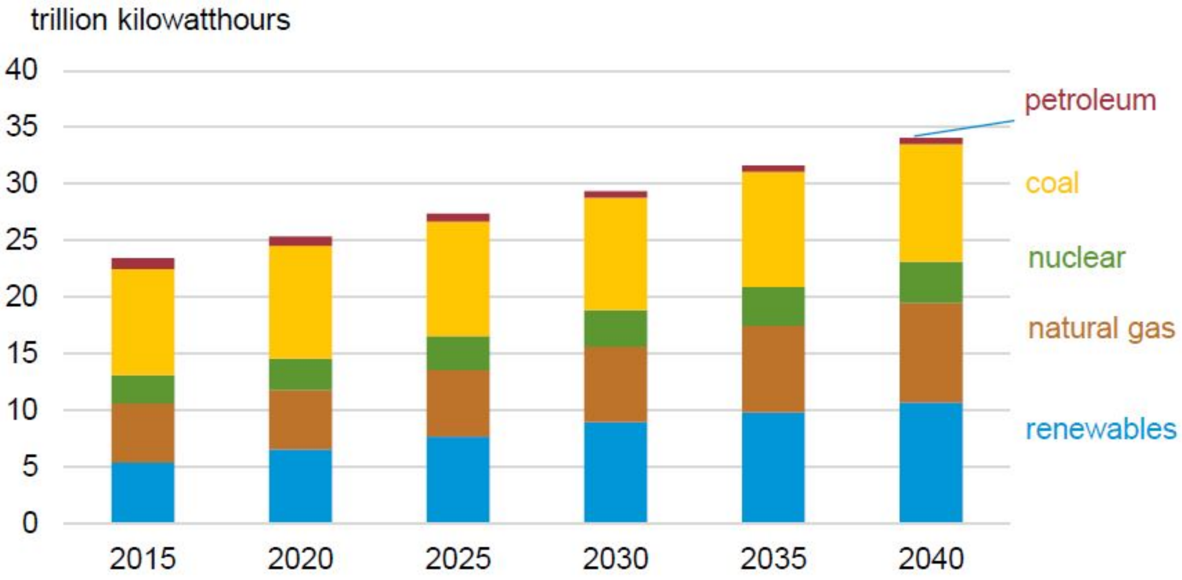

Figure 1.4: Global electricity estimation till 2040

As can be seen from Figure (1.3), 2% of the total global power capacity is composed of bio-power sources. These sources have grown as compared to 2015 despite low oil prices and policy uncertainty in some markets. The most prominent growth and overall bioenergy production has happened in India, with several promising developments in Africa [66].

1.2. ENERGY FROM BIOMASS

There is no worldwide accepted definition of the term "biomass". Any organic material derived from living or recently dead plants or animals can be termed as biomass [42]. However, the definition adopted by the United Nations Framework Convention on Climate Change (UNFCCC, 2005) [3] is the most relevant:

Biomass means non-fossilized and biodegradable organic material originating from plants, animals and micro-organisms. This shall also include products, by-products, residues and waste from agriculture, forestry and related industries as well as the non-fossilized biodegradable organic fractions of industrial and municipal wastes. Biomass also includes gases and liquids recovered from the decomposition of non-fossilized and biodegradable organic material.

Biomass includes various organic sources of energy, including wastes, residues and crops grown for energy purposes. The wastes and residues can be industrial, municipal and agricultural. Crops grown for energy purposes are generally used for producing biofuels, which are mainly used in transport sector. Organic matter from forests and biological organisms is also included. Three types of primary fuels can be produced from biomass [3]:

- **Liquid fuels** like ethanol, biodiesel, methanol, vegetable oil and pyrolysis oil.
- **Gaseous fuels** like biogas, producer gas, syngas and substitute natural gas.
- **Solid fuels** like charcoal, torrified biomass, biocoke, biochar and hydrochar.

As mentioned before, solar PV is the fastest growing source of renewable energy, followed by wind and hydropower. However, the present largest source of global renewable energy is biomass. In 2016, the total primary energy supplied from biomass was approximately 62.5 exajoules (EJ). The supply of bioenergy has been growing globally at 2.5% per year since 2010. However, the global energy demand has also increased by 21% during the last ten years. Hence, the share of primary energy supply from biomass has remained approximately constant at 10.5% since 2005. The majority of bioenergy is used in industrial and building heating, with much less being used in electricity generation and transport sector [66]. The share of bioenergy in overall total energy consumption and sector-wise consumption globally is shown in Figure (1.5).

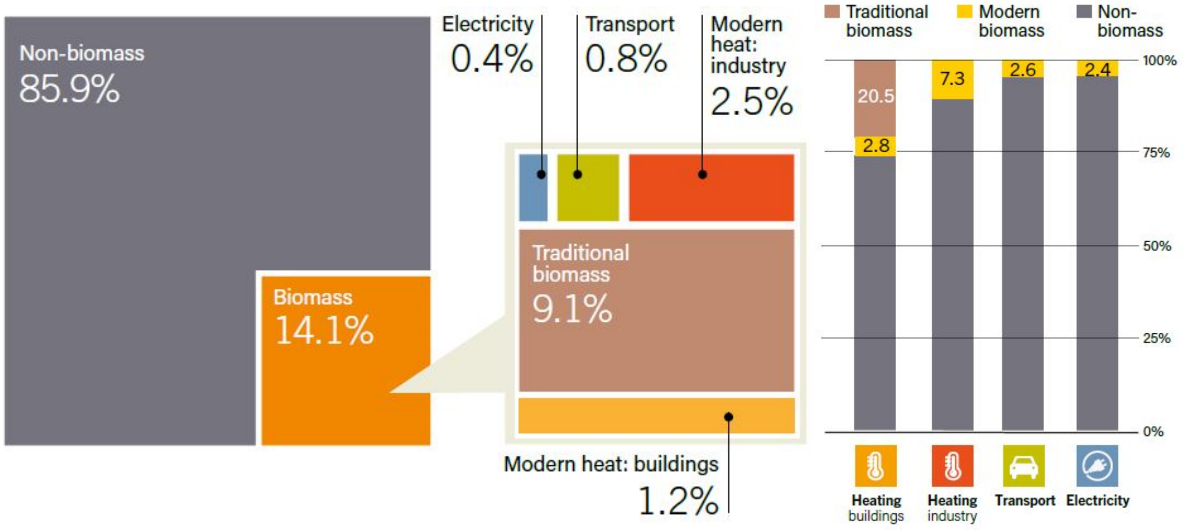

(a) Total share of bioenergy

(b) Sector-wise share of bioenergy

Figure 1.5: Share of bioenergy in global consumption [66]

As mentioned before, energy carriers can be extracted from biomass via various conversion technologies. However, all these methods can be classified into two categories [29]:

- Thermochemical: They involve the application of heat to extract energy from biomass. They include combustion, gasification, liquefaction and pyrolysis. Torrefaction is another thermochemical method used for pretreating biomass to improve its physical and chemical properties as a fuel or feedstock.

- Biochemical: They involve the use of microscopic organisms to convert the complex organic structure of biomass into simpler biofuels. They include industrial fermentation and anaerobic digestion. These two processes are carried out in absence of any oxidising agent or external energy source.

Physical extraction of vegetable oils from energy crops like rapeseed, soybean, jatropha, mustard, jojoba, flax, sunflower and others and their subsequent trans-esterification (with methanol, for instance) into biodiesel may also be considered as an additional energy carrier extraction method.

1.2.1. BIOMASS GASIFICATION

Gasification is one of the thermochemical conversion technologies to extract energy carriers from biomass. It is used to convert solid or fluid biomass into a combustible product gas. This process is carried out at high temperatures using a gaseous agent (mostly oxidising, sometimes also reducing). The product gases have different names depending on the gaseous agent being used. When atmospheric air is used, the product gas is called “producer gas” and it contains hydrogen (H_2), carbon-monoxide (CO) and methane (CH_4) as combustible components with some fraction of inert components like carbon-dioxide (CO_2) and water vapour (H_2O) and a bulk nitrogen (N_2) concentration. Other gaseous agents are also used like steam, high-purity oxygen, CO_2 or steam/oxygen mixtures. The product gas thus formed is called biosyngas [35] [52].

Gasification of biomass may be carried out separately or along with other fuels (e.g. coal) in various kinds of reactors. These reactors are classified on the basis of the transport process occuring inside them [6]. Each category of gasifiers are used for a certain scale of operations in terms of thermal power capacity as shown in Figure (1.8).

- Fixed bed gasifiers: They are called so because the relative positions of various distinct reaction zones remain fixed and the gasifying bed remains stationary. They are used for relatively small scale operations of the order of a few MW_{th}. There are three basic configurations in this category: updraft, downdraft and cross-draft gasifiers (as shown in Figure (1.6)).

- Fluidised bed gasifiers: They are called so because the bed of small inert (or catalytic) particles is kept in fluidised state (against gravity) by blowing a gasification agent through it. Hence, there are no distinct reaction zones like in fixed bed, resulting in an even temperature and species distribution. They are used for medium to large scale operations ranging from 10 MW_{th} to 100 MW_{th}. Three types of gasifiers are available in this category: bubbling fluidised bed (BFB), circulating fluidised bed (CFB) and interconnected (indirect) fluidised bed gasifiers (as shown in Figure (1.7)). These gasifiers may be driven by direct (autothermal) or indirect (allothermal) heating systems, depending whether the heating agent comes in contact with the fluidised bed or not.

- Entrained flow (EF) gasifiers: They are designed for large scale operation (more than 100 MW_{th}), resulting in economical production of biofuels or power generation using advanced and efficient cycles. When biomass used as feedstock, it must first be fine powdered or pyrolysed and converted to slurry. The powder/slurry is then mixed with steam, or steam and oxygen, to be gasified in a flame.

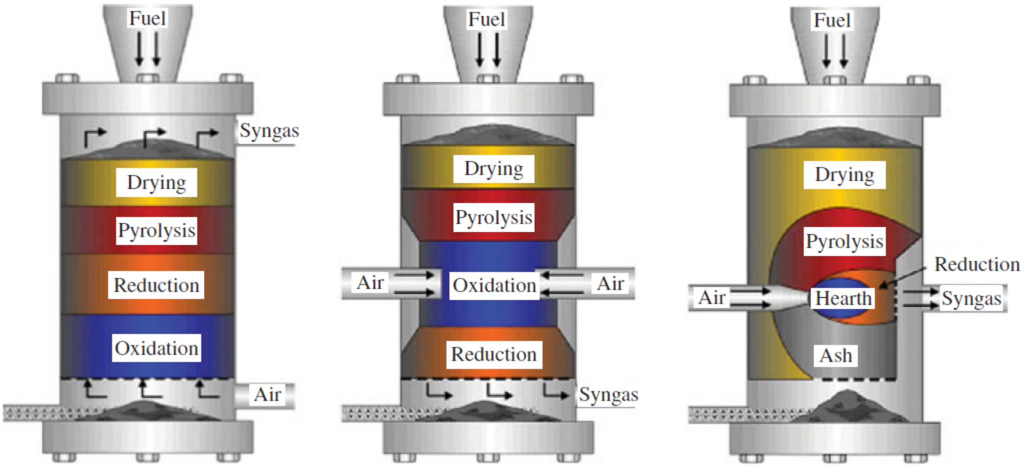

Figure 1.6: Fixed bed gasifiers: updraft (left), downdraft (center) and cross-draft (right) [29]

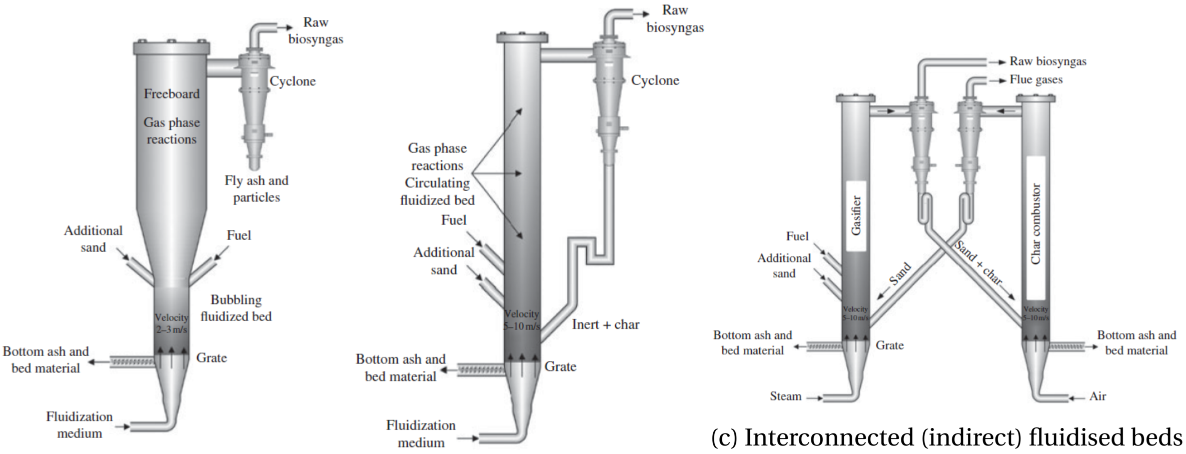

(a) BFB gasifier

(b) CFB gasifier

(c) Interconnected (indirect) fluidised beds

Figure 1.7: Various fluidised bed gasifiers [29]

There are various factors that need to be taken into account while selecting the type of gasifier for any given kind of biomass [29]:

- Scale of operations: This is the primary criterion for selection. Small scale gasifiers may be easy to set up and maintain but may only be used for local operations, with a particular kind of feedstock. However, large scale operations may prove economical for mass production of biofuels or power generation.

- Feedstock flexibility: Gasifiers which are able to run on various kinds of biomass are always preferred over single-type gasifiers. However, the physical and chemical properties of biomass may also need to be modified for proper operation of gasifiers.

- Ash and composition sensitivity: The inorganic component of biomass (ash) depends upon its relative mineral content and has appreciable impact on the operation of gasifiers. High ash content may affect fluidised bed gasifiers (in the form of agglomeration) and EF gasifiers (in terms of slagging and fouling). It may also lead to other difficulties in process operation and unscheduled maintenance stops.

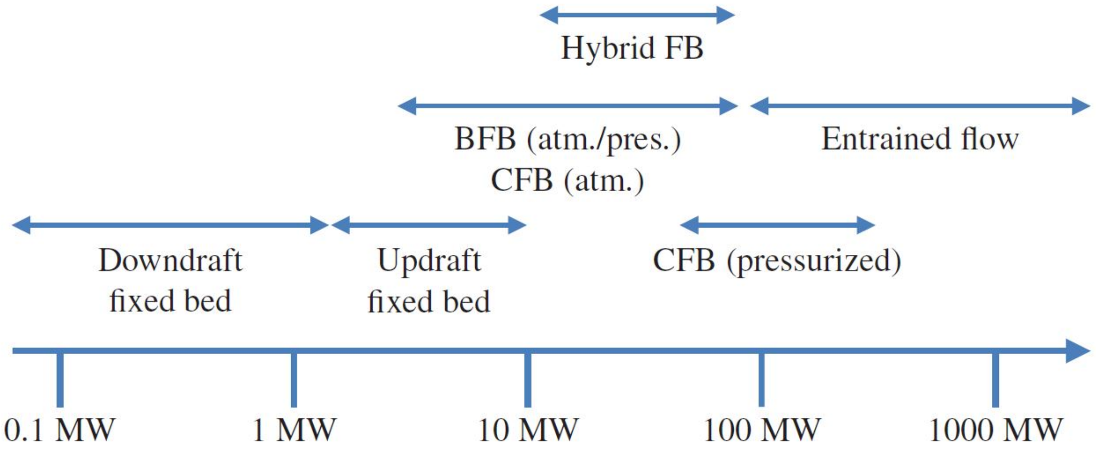

Figure 1.8: Different scales of biomass gasifiers [29]

- Tar generation characteristics: Tar is the generic term for heavy polyaromatic hydrocarbon species that are generated during the gasification process. These tars may adversely affect the equipment downstream of the gasifiers, but also significantly contributing to the heating value of the product gas. Therefore, adequate amount of gas cleaning and upgrading is necessary with respect to this class of contaminants.

1.2.2. INDIRECTLY HEATED BUBBLING FLUIDISED BED STEAM REFORMER

TU Delft Process and Energy department and the Dutch company Petrogas Gas-Systems B.V. are working together on the commissioning of a small 50 kW_{th} Indirectly Heated Bubbling Fluidised Bed Steam Reformer (IHBFBSR). The bed of this reactor will be comprised of corundrum, which is aluminium oxide (Al_2O_3) with traces of iron oxide and silica. It will be accompanied by the additive kaolin ($Al_2Si_2O_5(OH)_4$) which reduces the agglomeration problem in fluidised beds. This reactor will be first tested for gasification using high purity woody biomass, causing minimum problems. Finally, it will be commissioned for the gasification of the energy crop Miscanthus.

In this reactor, the gasification agent is blown from the bottom throughout the bed at intermediate velocities, such that it forms bubbles within the bed zone. The gas velocity is significantly above (approximately 2.5 times) the minimum fluidisation velocity (approximately 0.5-2.0 m/s) and below the maximum terminal velocity so that the bed material remains within the reactor [29].

The main difference between this reactor and other fluidised bed reactors is the use of indirect heating methods for the required energy input. The heating is done by two self-recuperative flame burners fitted with one recirculating (single-ended) radiant tube each. The main advantage of using such radiant tube burners is the even heat distribution along the whole radiant surface, leading to high quality of product gas. These burners are explained briefly in the following section.

1.3. RADIANT TUBE BURNERS

In many heating processes, the object to be heated must not come in direct contact with the products of combustion or the flame. In such cases, radiant tube burners provide excellent heating. These burners are mainly used in metallurgical heat treatment field, as those processes may require special atmospheres or extremely clean conditions in the furnace. The main advantage of using these burners is that the combustion process is completely contained inside the radiant tube. The combusting flow transfers energy to the walls of the tube, where it gets conducted and finally radiated out to the required load. Radiant tube burners are normally fired using gaseous fuels, although oil-fired burners are also available [30].

1.3.1. TYPES OF RADIANT TUBES

Radiant tubes have to be designed to provide as uniform temperature as possible for uniform heating while always remaining within the maximum temperature limits of the design materials. To this end, various configurations are commercially available, as shown in Figure (1.9). These configurations have been broadly categorised into recirculating and non-recirculating types [30] [64].

- Recirculating tubes are designed for mixing of fresh combusting mixture ejected from the burner with the mixture already present in the tube. They use high-velocity burners to entrain combustion products from the exhaust and their jet action to inject fresh mixture into the tube. The main advantage is the reduction of peak temperatures and increased temperature and heat uniformity due to highly dilute combustion.
- Non-recirculating tubes are designed for only a single pass of the combusting flow along the length of the tube. However, the shape of the tube may not necessarily be straight, curved ones are also possible. These tubes are more common than recirculating ones in the industry.

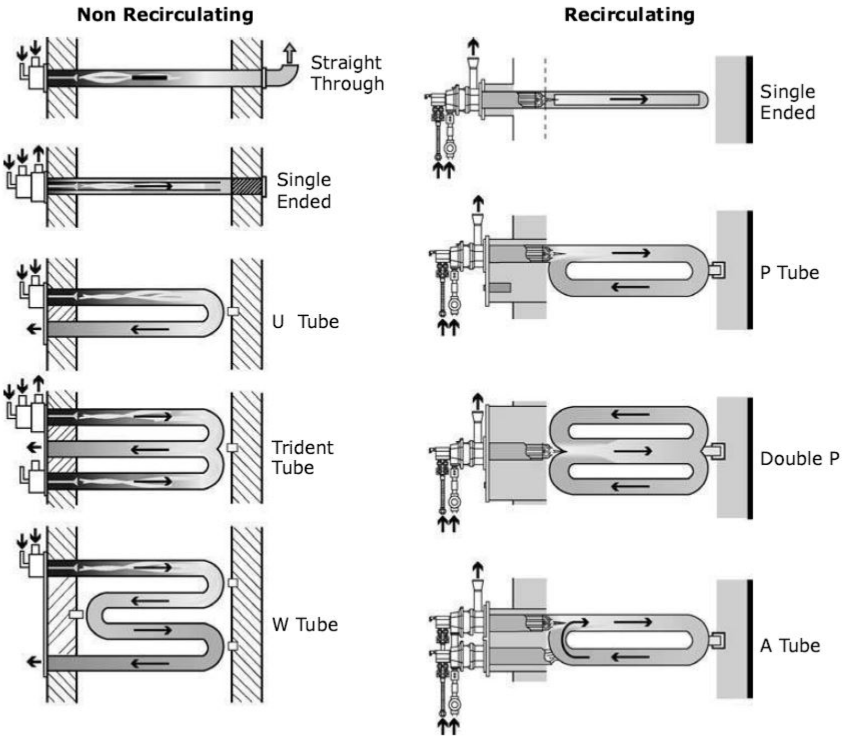

Figure 1.9: Recirculating and non-recirculating radiant tube configurations [30]

1.3.2. TYPES OF BURNERS FOR RADIANT TUBES

The burners for radiant tubes are typically classified on the basis of heat recovery system and inlet configurations for fuel and air. Small burners with low exhaust temperatures and/or firing rates usually use cold (ambient) air for combustion, where the use of heat recovery system is not economically feasible. Larger temperatures and/or firing rates necessitate the use of recuperators, self-recuperative burners or regenerative burners [30].

The interior of the radiant tube forms the combustion chamber for the fuel and it may be operated at higher, lower or the same pressure as the furnace in which the tube provides heating. This pressure inside the tube is controlled by the inlet mechanism of the air and fuel. Both air and fuel may be controlled and pressurised. Hence, the following types of burners are available [30]:

- Inspirator and pull-through burners: These burners pressurise only the fuel at the inlet and ambient air is pulled in by the entrainment action of a high-pressure fuel jet. Hence, the air flow is difficult to control in order to maintain the required air-fuel ratio. Consequently, the temperature and heating uniformity of the tubes is not controlled properly when using these burners.

- Forced-draft burners: These burners control the inlet conditions of the combustion air, providing a greater control over the overall stoichiometry of the combustion process. Consequently, the desired temperature and heat uniformity is achieved over the radiant tube surface. In such burners, recuperative or regenerative modes of heat recovery from the exhaust gases are usually employed for greater thermal efficiency and minimal wastage. Regenerative burners are usually used with non-recirculating tubes and recuperative burners are usually used with recirculating tubes.

The gasifier commissioned by TU Delft and the Dutch company involves the use of two different models of forced-draft self-recuperative burners, installed vertically at the top and bottom of the reactor. These burners integrate the burner components and heat exchanger into a single package, minimizing air-side heat losses and achieving reduction in size. Each burner is fitted with a single-ended recirculating type of radiant tube. The burners and radiant tubes have been provided by the German company WS Wärmeprozesstechnik GmbH.

1.4. RESEARCH OBJECTIVES

This thesis is an attempt to study the working of both self-recuperative burners fitted with appropriate radiant tubes. The main focus is on the quantification of heat transfer from the tubes and its variation with various parameters. To analyse this mechanism, numerical modelling of the fluid flow and heat transfer processes has been done using the commercially available software ANSYS® Fluent version 18.2. The main research objectives are as follows:

- **Heat transfer analysis:** Estimate the heat transfer rate and its efficiency from both the tubes and study its variation with air factor and preheat temperature.

- **Optimum condition determination:** Determine the optimum condition for operating the equipment in terms of maximising the heat transfer, efficiency and minimising fuel wastage.

- **Robustness check:** Check the robustness of the calculations by conducting tests on different grid sizes and analysing the variation of the results, if any.

Please note that this study is concerned with only the interior of the radiant tubes. The heat transfer mechanism from the outer surface of the tubes to the fluidised bed was not known at the time of this study. Hence, the outer conditions have been accounted for using simplified assumptions, which may lead to disagreement between the results of this study and experimental data. Hence, this study is only the first step towards a proper understanding of radiant tubes.

The next chapter provides the fundamentals of Computational Fluid Dynamics procedures, including the various turbulence models, combustion models and combustion mechanisms available in the literature. Chapter 3 then provides a brief summary of the previous work done on radiant tubes and burners by various authors at various institutes. Chapter 4 contains the description of the current case, stating various assumptions made for the calculations along with preliminary analysis of flow. This leads to the choice of appropriate turbulence and combustion models, along with combustion mechanism. It also describes the geometric model used along with the meshing procedure, finally ending with the material properties of the tubes. Chapter 5 first explains the scheme of calculations to provide an overview of the work, followed by the results and appropriate discussion. Finally, chapter 6 presents the conclusions drawn from this work and recommendations for future studies, both computational and experimental, thus ending this report.

2

A BRIEF OVERVIEW OF CFD

Computational Fluid Dynamics (CFD) is a method of analysing systems which involve fluid flow, heat transfer and associated phenomena such as chemical reactions by means of a computer-based simulation [79]. This is a very powerful branch of fluid flow analysis and has witnessed copious research on the academic and industrial front over the decades with scales reaching from that of flow of blood in arteries and veins to that of aerodynamics of aircrafts and land vehicles and that of flow of rivers and oceanic currents. With the advent of new and powerful computers and faster and more robust numerical techniques, knowledge in this area has increased manifold.

As mentioned above, CFD techniques can be used to analyse systems involving length and time scales of great variety. However, every analysis follows the solution of partial differential governing equations using the following method [79]:

- Integration of the governing equations of fluid flow over all the (finite) control volumes of the computational domain.
- Conversion of resulting integral equations into a system of algebraic equations, a process known as discretization.
- Solution of algebraic equations by an iterative method.

2.1. GOVERNING EQUATIONS

Let us first understand what governing equations are solved by the code. In any kind of fluid flow, two quantities are always conserved: mass and momentum of the fluid. In the case of heat transfer from non-reacting fluids, the total energy is also conserved. In the case of a reacting flow, the energy of the fluid will also be conserved and the individual chemical species will be produced or consumed according to the overall rate of the reaction.

2.1.1. CONSERVATION OF MASS

The principle of conservation of mass states that mass can neither be created nor destroyed. This is certainly true for any fluid flow, reacting or non-reacting. This principle can be translated into a mathematical equation by considering the mass balance of a small control volume of dimensions $\delta x, \delta y$ and δz as shown in Figure (2.1).

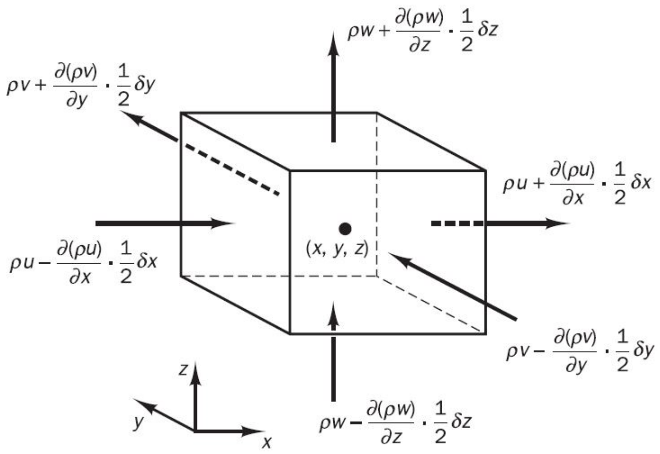

Figure 2.1: Mass flows in and out of fluid element [79]

Summing the mass flow over all the faces and equating it to zero (to ensure that there is no net change in the mass), we get, upon simplifying:

$$\frac{\partial \rho}{\partial t} + \frac{\partial(\rho u)}{\partial x} + \frac{\partial(\rho v)}{\partial y} + \frac{\partial(\rho w)}{\partial z} = 0 \tag{2.1}$$

In vector form, it can be expressed as follows:

$$\frac{\partial \rho}{\partial t} + \operatorname{div}(\rho \mathbf{u}) = 0 \tag{2.2}$$

This is the unsteady, three-dimensional mass conservation equation or "continuity equation". It is valid at any point in a compressible fluid. For an incompressible fluid or at steady state, the first term has no contribution, as the density is constant, so the equation becomes as follows:

$$\operatorname{div} \mathbf{u} = 0 \tag{2.3}$$

2.1.2. CONSERVATION OF MOMENTUM

The principle of conservation of momentum states that in absence of an external force, the total momentum of the fluid remains conserved. This principle can be converted into a mathematical statement by applying the Newton's second law to a single fluid particle. Since the momentum of every fluid particle is conserved, the momentum of the complete fluid flow shall remain conserved. Consider a fluid element with the forces acting on it as shown in Figure (2.2):

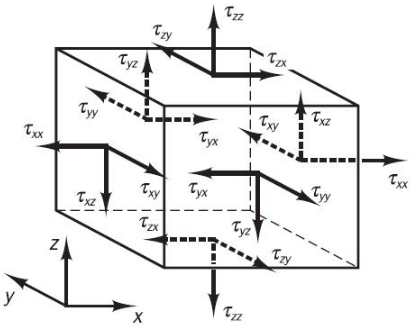

Figure 2.2: Stress components on three faces of fluid element [79]

First we consider the x-component of the forces due to pressure p and stress components τ_{xx}, τ_{yx} and τ_{zx} as shown in Figure (2.3):

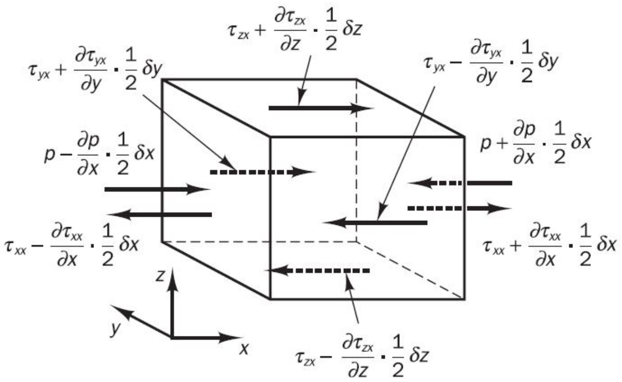

Figure 2.3: Stress components in x-direction [79]

Summing the forces on all the faces and equating the result to the net change of x-momentum, we get the following:

$$\rho \frac{Du}{Dt} = \frac{\partial(-p + \tau_{xx})}{\partial x} + \frac{\partial \tau_{yx}}{\partial y} + \frac{\partial \tau_{zx}}{\partial z} + S_{Mx} \tag{2.4}$$

Similarly, the y-component and z-component of the momentum equation can be obtained by a similar analysis as follows:

$$\rho \frac{Dv}{Dt} = \frac{\partial \tau_{xy}}{\partial x} + \frac{\partial(-p + \tau_{yy})}{\partial y} + \frac{\partial \tau_{zy}}{\partial z} + S_{My} \tag{2.5}$$

$$\rho \frac{Dw}{Dt} = \frac{\partial \tau_{xz}}{\partial x} + \frac{\partial \tau_{yz}}{\partial y} + \frac{\partial(-p + \tau_{zz})}{\partial z} + S_{Mz} \tag{2.6}$$

Here, the components S_{Mx}, S_{My} and S_{Mz} denote the contributions due to body forces like gravity force, centrifugal force, Coriolis force, electromagnetic force etc. However, such equations have the stress terms as unknowns. Fortunately, most fluids are Newtonian in nature. For such fluids, stress terms can be expressed in terms of linear deformation rates and volumetric deformation rate. There are nine linear deformation rates, six of which are independent of each other. There are three independent linear strain rates are as follows:

$$s_{xx} = \frac{\partial u}{\partial x} \qquad s_{yy} = \frac{\partial v}{\partial y} \qquad s_{zz} = \frac{\partial w}{\partial z} \tag{2.7}$$

There are six shearing rates, three of which are independent as follows:

$$s_{xy} = s_{yx} = \frac{1}{2}\left(\frac{\partial u}{\partial y} + \frac{\partial v}{\partial x}\right) \qquad s_{yz} = s_{zy} = \frac{1}{2}\left(\frac{\partial v}{\partial z} + \frac{\partial w}{\partial y}\right) \qquad s_{xz} = s_{zx} = \frac{1}{2}\left(\frac{\partial u}{\partial z} + \frac{\partial w}{\partial x}\right) \tag{2.8}$$

The volumetric rate of deformation is given by:

$$\frac{\partial u}{\partial x} + \frac{\partial v}{\partial y} + \frac{\partial w}{\partial z} = \operatorname{div} \mathbf{u} \tag{2.9}$$

For a Newtonian fluid, the stresses are related to the linear deformation rate by the constant of proportionality μ, called the dynamic viscosity, and to the volumetric deformation rate by λ as follows:

$$\tau_{xx} = 2\mu \frac{\partial u}{\partial x} + \lambda \operatorname{div} \mathbf{u} \qquad \tau_{yy} = 2\mu \frac{\partial v}{\partial y} + \lambda \operatorname{div} \mathbf{u} \qquad \tau_{zz} = 2\mu \frac{\partial w}{\partial z} + \lambda \operatorname{div} \mathbf{u} \tag{2.10}$$

$$\tau_{xy} = \tau_{yx} = \mu\left(\frac{\partial u}{\partial y} + \frac{\partial v}{\partial x}\right) \qquad \tau_{yz} = \tau_{zy} = \mu\left(\frac{\partial v}{\partial z} + \frac{\partial w}{\partial y}\right) \qquad \tau_{xz} = \tau_{zx} = \mu\left(\frac{\partial u}{\partial z} + \frac{\partial w}{\partial x}\right) \tag{2.11}$$

For most fluids, the Stokes assumption is valid which states that $\lambda = -\frac{2}{3}\mu$ [37]. For incompressible flows, div $\vec{u} = 0$ and the viscous stresses depend only upon the linear deformation rates. Substituting the above rates into the momentum conservation laws:

$$\rho\frac{Du}{Dt} = -\frac{\partial p}{\partial x} + \frac{\partial}{\partial x}\left[2\mu\frac{\partial u}{\partial x} + \lambda \operatorname{div}\vec{u}\right] + \frac{\partial}{\partial y}\left[\mu\left(\frac{\partial u}{\partial y} + \frac{\partial v}{\partial x}\right)\right] + \frac{\partial}{\partial z}\left[\mu\left(\frac{\partial u}{\partial z} + \frac{\partial w}{\partial x}\right)\right] + S_{Mx} \tag{2.12}$$

$$\rho\frac{Dv}{Dt} = -\frac{\partial p}{\partial y} + \frac{\partial}{\partial x}\left[\mu\left(\frac{\partial u}{\partial y} + \frac{\partial v}{\partial x}\right)\right] + \frac{\partial}{\partial y}\left[2\mu\frac{\partial v}{\partial y} + \lambda \operatorname{div}\vec{u}\right] + \frac{\partial}{\partial z}\left[\mu\left(\frac{\partial v}{\partial z} + \frac{\partial w}{\partial y}\right)\right] + S_{My} \tag{2.13}$$

$$\rho\frac{Dw}{Dt} = -\frac{\partial p}{\partial z} + \frac{\partial}{\partial x}\left[\mu\left(\frac{\partial u}{\partial z} + \frac{\partial w}{\partial x}\right)\right] + \frac{\partial}{\partial y}\left[\mu\left(\frac{\partial v}{\partial z} + \frac{\partial w}{\partial y}\right)\right] + \frac{\partial}{\partial z}\left[2\mu\frac{\partial w}{\partial z} + \lambda \operatorname{div}\vec{u}\right] + S_{Mz} \tag{2.14}$$

The above equations can be simplified by arranging viscous stress terms as follows:

$$\frac{\partial}{\partial x}\left[2\mu\frac{\partial u}{\partial x} + \lambda \operatorname{div}\vec{u}\right] + \frac{\partial}{\partial y}\left[\mu\left(\frac{\partial u}{\partial y} + \frac{\partial v}{\partial x}\right)\right] + \frac{\partial}{\partial z}\left[\mu\left(\frac{\partial u}{\partial z} + \frac{\partial w}{\partial x}\right)\right] = \operatorname{div}(\mu \operatorname{grad} u) + [s_{Mx}] \tag{2.15}$$

Now, the smaller source terms ($[s_{Mx}]$) can be clubbed with body forces to give the total source term as follows:

$$S_{tot} = S_M + [s_M] \tag{2.16}$$

Hence, the final form of the momentum equations can be written as follows:

$$\rho\frac{Du}{Dt} = -\frac{\partial p}{\partial x} + \operatorname{div}(\mu \operatorname{grad} u) + S_{tot,x} \tag{2.17}$$

$$\rho\frac{Dv}{Dt} = -\frac{\partial p}{\partial y} + \operatorname{div}(\mu \operatorname{grad} v) + S_{tot,y} \tag{2.18}$$

$$\rho\frac{Dw}{Dt} = -\frac{\partial p}{\partial z} + \operatorname{div}(\mu \operatorname{grad} w) + S_{tot,z} \tag{2.19}$$

The above equations are known as Navier-Stokes equations after Claude-Louis Navier and George Gabriel Stokes, who derived them independently in the nineteenth-century. The equations written in the above form are the most suitable for finite volume method [79].

2.1.3. TURBULENCE MODELLING

Analysis of turbulence is one of the most important and difficult challenges encountered while studying fluid flows. It is important because almost all of the flows of practical importance are turbulent in nature. It is difficult because there has not been a single theory that can numerically model the behaviour of all the turbulent flows of practical importance. Although many theories have been proposed to understand such processes, they are limited to their respective specific applications and may produce unacceptable results in other applications.

Any fluid flow can be categorised as laminar, transitioning or turbulent on the basis of a non-dimensional quantity called the Reynolds number (Re). It is defined as the ratio of inertia forces to viscous forces. Below a critical value Re_{crit}, the flow is smooth and adjacent layers of fluid slide past each other in orderly fashion. Such a flow is called laminar flow. Above the critical value, the flow becomes random and chaotic, characterised by intrinsic unsteadiness even with steady boundary conditions. All the flow properties vary continuously with time and such a flow is called turbulent flow. Currently, the most widely accepted theory to understand the physical process of turbulence was proposed by Kolmogorov in 1941 [36]. This theory states that the random nature of turbulence can be understood in terms of rotating lumps of fluid mass called eddies. The size and velocity of these eddies in a turbulent flow can range from the largest scale to the smallest. The largest eddies

can have the size and velocity of the order of the size and velocity of the mean flow, called the integral scale. The smallest eddies are of the size where the inertia and viscous forces balance out each other and this results in the dissipation of the kinetic energy of the eddy into thermal energy. The scale at which this happens is called the Kolmogorov scale. This process of transfer of kinetic energy from the largest to the smallest eddy and its eventual dissipation into thermal energy is called energy cascade.
The numerical modelling of turbulence is achieved via three different approaches, each involving different levels of detail and computational requirements. These approaches differ in the extent to and the manner in which the eddies in the turbulent flow are modelled in the CFD code. They are briefly explained below:

- **Reynolds Averaged Navier Stokes (RANS) approach**: This is the simplest and the most widely used apprach in industry as well as academia. It involves the decomposition of the flow properties into a steady mean value with a fluctuating component superimposed on it. This is called the Reynolds decomposition, hence the name. Any general flow property ϕ can be decomposed as:

  $$\phi(t) = \bar{\Phi}(t) + \phi'(t) \tag{2.20}$$

  where $\phi(t)$ is the instantaneous value, $\bar{\Phi}(t)$ is the mean value and $\phi'(t)$ is the temporal fluctuation of the property ϕ. The unknowns in the conservation equations are replaced by their decomposed form and equations are derived for their mean values with algebraic expressions to account for the contributions from the fluctuations.

- **Large Eddy Simulation (LES) approach**: This approach involves the numerical modelling of large eddies directly via conservation equations and modelling of smaller eddies via subgrid closure rules. The size of eddies to be directly modelled and those via closure rules is determined by spatial filters embedded in the CFD code. These can be manually set to the requirement of the user and the accuarcy required. This approach captures low frequency variations in flow properties.

- **Direct Numerical Simulation (DNS) approach**: This approach involves direct simulation of all the eddies upto the Kolmogorov scale via the conservation equations, without any algebraic or subgrid closure models. Hence, it can capture all variations in the flow properties. However, it is computationally the most expensive amongst all the approaches and requires high performance computing systems to run for long periods of time. Hence, it has been limited to academic research purposes till now.

The difference between RANS, LES and DNS is summarised in Figure (2.4). It shows the difference in the temperature predicted via the three different approaches in a turbulent flame.

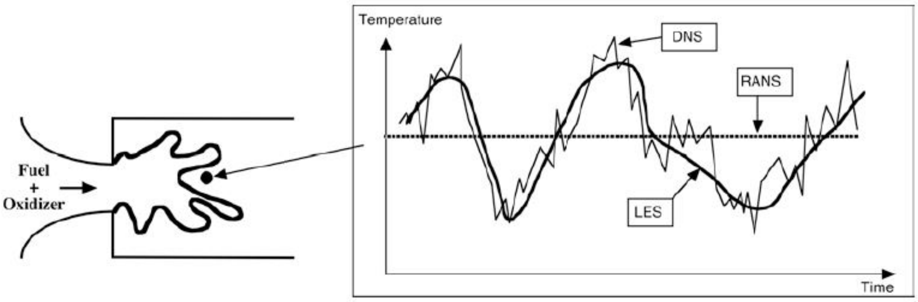

Figure 2.4: Difference between RANS, LES and DNS [61]

This thesis involves the RANS simulation of turbulent combustion in radiant tube heaters. Hence, the approach is explained in detail as follows.

As mentioned before, RANS approach involves decomposing of any fluid property into a mean value and fluctuating component. There are two types of means defined for RANS approach, time average and Favre average. The former is used for incompressible flows while the latter for compressible flows. The time average is defined as follows:

$$\bar{\Phi} = \frac{1}{\Delta t} \int_0^{\Delta t} \phi(t) dt \tag{2.21}$$

For incompressible flows, the continuity ad Navier-Stokes equations for averaged quantities are as follows:

$$\frac{\partial \bar{u}}{\partial x} + \frac{\partial \bar{v}}{\partial y} + \frac{\partial \bar{w}}{\partial z} = 0 \qquad \text{or} \qquad \operatorname{div} \bar{\mathbf{U}} = 0 \tag{2.22}$$

$$\frac{\partial \bar{u}}{\partial t} + \operatorname{div}(\bar{u}\bar{\mathbf{U}}) = -\frac{1}{\rho}\frac{\partial P}{\partial x} + \nu \operatorname{div}(\operatorname{grad}(\bar{u})) + \frac{1}{\rho}\left[\frac{\partial(-\rho\overline{u'^2})}{\partial x} + \frac{\partial(-\rho\overline{u'v'})}{\partial y} + \frac{\partial(-\rho\overline{u'w'})}{\partial z}\right] \tag{2.23}$$

$$\frac{\partial \bar{v}}{\partial t} + \operatorname{div}(\bar{v}\bar{\mathbf{U}}) = -\frac{1}{\rho}\frac{\partial P}{\partial y} + \nu \operatorname{div}(\operatorname{grad}(\bar{v})) + \frac{1}{\rho}\left[\frac{\partial(-\rho\overline{u'v'})}{\partial x} + \frac{\partial(-\rho\overline{v'^2})}{\partial y} + \frac{\partial(-\rho\overline{v'w'})}{\partial z}\right] \tag{2.24}$$

$$\frac{\partial \bar{w}}{\partial t} + \operatorname{div}(\bar{w}\bar{\mathbf{U}}) = -\frac{1}{\rho}\frac{\partial P}{\partial z} + \nu \operatorname{div}(\operatorname{grad}(\bar{w})) + \frac{1}{\rho}\left[\frac{\partial(-\rho\overline{u'w'})}{\partial x} + \frac{\partial(-\rho\overline{v'w'})}{\partial y} + \frac{\partial(-\rho\overline{w'^2})}{\partial z}\right] \tag{2.25}$$

The last terms in the Navier-Stokes equations represent contributions from the fluctuating components of the flow properties. They are called the Reynolds stresses and must be modelled. There are three normal stresses:

$$\tau_{xx} = -\rho\overline{u'^2} \qquad \tau_{yy} = -\rho\overline{v'^2} \qquad \tau_{zz} = -\rho\overline{w'^2} \tag{2.26}$$

and three shear stresses:

$$\tau_{xy} = \tau_{yx} = -\rho\overline{u'v'} \qquad \tau_{xz} = \tau_{zx} = -\rho\overline{u'w'} \qquad \tau_{yz} = \tau_{zy} = -\rho\overline{v'w'} \tag{2.27}$$

When compressible equations are averaged using time average methods, it results in an unclosed correlation between density and velocity fluctuations as follows:

$$\frac{\partial \bar{\rho}}{\partial t} + \frac{\partial(\bar{\rho}\bar{u})}{\partial x} + \frac{\partial(\bar{\rho}\bar{v})}{\partial y} + \frac{\partial(\bar{\rho}\bar{w})}{\partial z} = -\frac{\partial(\overline{\rho' u'})}{\partial x} - \frac{\partial(\overline{\rho' v'})}{\partial y} - \frac{\partial(\overline{\rho' w'})}{\partial z} \tag{2.28}$$

The RHS term of the above equation is awkward to handle in CFD codes, hence mass-weighted averages (i.e the Favre averages) are introduced.The Favre average is defined as follows:

$$\tilde{\Phi} = \frac{\overline{\rho\phi}}{\bar{\rho}} \tag{2.29}$$

Any quantity may be split into Favre average and its fluctuation as follows:

$$\phi(t) = \tilde{\Phi}(t) + \phi''(t) \qquad \text{with} \qquad \widetilde{\phi''} = 0 \tag{2.30}$$

Now, we can write the continuity and Navier-Stokes equations for Favre averaged quantities as folows:

$$\frac{\partial \bar{\rho}}{\partial t} + \frac{\partial(\bar{\rho}\tilde{u})}{\partial x} + \frac{\partial(\bar{\rho}\tilde{v})}{\partial y} + \frac{\partial(\bar{\rho}\tilde{w})}{\partial z} = 0 \qquad \text{or} \qquad \frac{\partial \bar{\rho}}{\partial t} + \operatorname{div}(\bar{\rho}\tilde{\mathbf{U}}) = 0 \tag{2.31}$$

$$\frac{\partial \bar{\rho}\tilde{u}}{\partial t} + \mathrm{div}(\bar{\rho}\tilde{u}\tilde{\mathbf{U}}) = -\frac{\partial \bar{P}}{\partial x} + \mathrm{div}(\mu \,\mathrm{grad}\, \tilde{u}) + \left[-\frac{\partial(\bar{\rho}\widetilde{u''^2})}{\partial x} - \frac{\partial(\bar{\rho}\widetilde{u''v''})}{\partial y} - \frac{\partial(\bar{\rho}\widetilde{u''w''})}{\partial z} \right] \tag{2.32}$$

$$\frac{\partial \bar{\rho}\tilde{v}}{\partial t} + \mathrm{div}(\bar{\rho}\tilde{v}\tilde{\mathbf{U}}) = -\frac{\partial \bar{P}}{\partial y} + \mathrm{div}(\mu \,\mathrm{grad}\, \tilde{v}) + \left[-\frac{\partial(\bar{\rho}\widetilde{u''v''})}{\partial x} - \frac{\partial(\bar{\rho}\widetilde{v''^2})}{\partial y} - \frac{\partial(\bar{\rho}\widetilde{v''w''})}{\partial z} \right] \tag{2.33}$$

$$\frac{\partial \bar{\rho}\tilde{w}}{\partial t} + \mathrm{div}(\bar{\rho}\tilde{w}\tilde{\mathbf{U}}) = -\frac{\partial \bar{P}}{\partial z} + \mathrm{div}(\mu \,\mathrm{grad}\, \tilde{w}) + \left[-\frac{\partial(\bar{\rho}\widetilde{u''w''})}{\partial x} - \frac{\partial(\bar{\rho}\widetilde{v''w''})}{\partial y} - \frac{\partial(\bar{\rho}\widetilde{w''^2})}{\partial z} \right] \tag{2.34}$$

Here too, the last terms on the RHS of Navier-Stokes equations represent contributions from the fluctuating components of the flow properties, which must be modelled.
There are two approaches to model such Reynolds stresses: via Boussinesq hypothesis and via Reynolds stress transport equations. They are explained briefly below:

- Boussinesq hypothesis: Proposed by Boussinesq in 1877 [79], it states that the Reynolds stresses may be proportional to the mean rates of deformation. Mathematically, it is expressed as follows:

  $$-\rho\overline{u_i'u_j'} = \mu_t\left(\frac{\partial \bar{u}_i}{\partial x_j} + \frac{\partial \bar{u}_j}{\partial x_i}\right) - \frac{2}{3}\left(\rho k + \mu_t \frac{\partial \bar{u}_k}{\partial x_k}\right)\delta_{ij} \tag{2.35}$$

  where $k = \frac{1}{2}(\overline{u'^2} + \overline{v'^2} + \overline{w'^2})$ is the turbulent kinetic energy pr unit mass, μ_t is the turbulent/eddy viscosity and δ_{ij} is the Kronecker delta function. This approach inherently assumes that the turbulence is homogeneous, i.e., same in all directions. There are many theories proposed to calculate turbulent viscosity, which are discussed later.

- Reynolds stress transport approach: This approach involves the calculation of each of the Reynolds stress terms via their respective conservation equations. It is computationally more expensive than Boussinesq approach and is used only in the cases where the assumption of homogeneous turbulence is invalid such as highly swirling flows and stress driven secondary flows. Otherwise, the additional computational effort is not justified by the little improvement achieved in accuracy. Even in the conservation equations for each stress terms, there are some unclosed terms which may require further modelling. Hence, the use of this approach is advised only when absolutely required.

The Boussinesq approach, as mentioned above, requires the calculation of turbulent viscosity and there have been many theories proposed for that purpose. They are categorised on the basis of the number of equations required to calculate the parameters required for the calculation of the viscosity. They are mentioned below:

- **Zero equation model: Prandtl mixing length model**: This model was proposed by Ludwig Prandtl in 1925 [63] and links turbulent viscosity with the mean stress tensor as follows:

  $$\mu_t = \bar{\rho} l_m^2 |\bar{S}| \tag{2.36}$$

  Here, $\bar{S}$ is the mean stress tensor as follows:

  $$\bar{S}_{ij} = \frac{1}{2}\left(\frac{\partial \bar{u}_i}{\partial x_j} + \frac{\partial \bar{u}_j}{\partial x_i}\right) \tag{2.37}$$

  and l_m is the mixing length to be given beforehand. Various models have been proposed to calculate the mixing length but it strongly depends on the geometry of the flow.

- **One equation model: Prandtl-Kolmogorov model**: This model requires one conservation equation of turbulent kinetic energy. The turbulent viscosity is then calculated as follows:

  $$\mu_t = \bar{\rho} C_\mu l_{pk} \sqrt{k} \tag{2.38}$$

Here, C_μ is an empirical constant (usually taken as 0.09) and l_{pk} is the characteristic length to be provided beforehand. Again, empirical relations are required for l_{pk}.

- **One equation model: Spalart-Allmaras model**: This model was proposed by P.R. Spallart and S.R. Allmaras in 1992 [74]. It was specifically designed for aerospace applications where pressure gradients are quite adverse and the effect of boundary layers is significant. This model involves the conservation equation for a parameter $\tilde{\nu}$ (not to be confused with the Favre average of some quantity ν), identical to kinematic turbulent viscosity and the turbulent viscosity is calculated from this parameter. The conservation equation for $\tilde{\nu}$ is as follows:

  $$\frac{\partial \rho\tilde{\nu}}{\partial t} + \frac{\partial}{\partial x_i}(\rho\tilde{\nu}\bar{u}_i) = \frac{1}{\sigma_{\tilde{\nu}}}\left[\frac{\partial}{\partial x_j}\left\{(\mu+\rho\tilde{\nu})\frac{\partial\tilde{\nu}}{\partial x_j}\right\} + C_{b2}\rho\left(\frac{\partial\tilde{\nu}}{\partial x_j}\right)^2\right] + C_{b1}\rho\tilde{\nu}\tilde{\Omega} - C_{w1}\rho\left(\frac{\tilde{\nu}}{\kappa y}\right)f_w \quad (2.39)$$

  Here, $\sigma_{\tilde{\nu}}, \kappa, C_{b1}$ and C_{b2} are numerical constants, C_{w1} is a constant calculated using these four constants and $\tilde{\Omega}$ is related to the mean vorticity tensor as follows:

  $$\tilde{\Omega} = \Omega + \frac{\tilde{\nu}}{(\kappa y)^2}f_{v2}; \quad \Omega = \sqrt{2\Omega_{ij}\Omega_{ij}}; \quad \Omega_{ij} = \frac{1}{2}\left(\frac{\partial\bar{u}_i}{\partial x_j} - \frac{\partial\bar{u}_j}{\partial x_i}\right) \text{ (mean vorticity tensor)} \quad (2.40)$$

  The turbulent viscosity is calculated as $\mu_t = \rho\tilde{\nu}f_{v1}$ and the functions f_{v1}, f_{v2} and f_w are wall-damping functions.

- **Two equation models**: There are multiple two-equation models available for turbulence modelling and are the most popular models for that purpose. They are popular because of their robustness and ease of computation. The most popular models are the $k-\varepsilon$ model and the $k-\omega$ model. There are multiple variations available for the two models and each has its own advantages and disadvantages. A general overview of these models is given below.

$k-\varepsilon$ MODELS

These are the most popular models used in industry and academia for the purpose of turbulence modelling and prediction. There are three variations available for general use: Standard, RNG and Realisable $k-\varepsilon$ model. They are described in detail below.

Standard $k-\varepsilon$ model:

This model was proposed by Launder and Spalding in 1972 [40] and has since become the most popular model for turbulence modelling in academia and industry. It is popular because of its computational ease, robustness and reasonable accuracy for a wide range of flows. It involves the transport equations for two quantities, turbulent kinetic energy (k) and its dissipation rate (ε). Turbulent kinetic energy is calculated as the kinetic energy per mass due to velocity fluctuations as follows:

$$k = \frac{1}{2}\left(\overline{u'^2} + \overline{v'^2} + \overline{w'^2}\right) \quad (2.41)$$

The transport equations for k and ε respectively are given below:

$$k \text{ equation}: \quad \frac{\partial(\rho k)}{\partial t} + \frac{\partial(\rho k\bar{u}_i)}{\partial x_i} = \frac{\partial}{\partial x_i}\left[\left(\frac{\mu_t}{\sigma_k}\right)\frac{\partial k}{\partial x_i}\right] + 2\mu_t\bar{S}_{ij}\bar{S}_{ij} - \rho\varepsilon \quad (2.42)$$

$$\varepsilon \text{ equation}: \quad \frac{\partial(\rho\varepsilon)}{\partial t} + \frac{\partial(\rho\varepsilon\bar{u}_i)}{\partial x_i} = \frac{\partial}{\partial x_i}\left[\left(\frac{\mu_t}{\sigma_\varepsilon}\right)\frac{\partial\varepsilon}{\partial x_i}\right] + 2C_{1\varepsilon}\frac{\varepsilon}{k}\mu_t\bar{S}_{ij}\bar{S}_{ij} - C_{2\varepsilon}\rho\frac{\varepsilon^2}{k} \quad (2.43)$$

The turbulent viscosity is calculated as folows:

$$\mu_t = \rho C_\mu\frac{k^2}{\varepsilon} \quad (2.44)$$

Here, $C_{1\varepsilon}, C_{2\varepsilon}$ and C_μ are model constants and σ_k and σ_ε are turbulent Prandtl numbers for k and ε respectively. Their values are given below:

$$C_{1\varepsilon} = 1.44 \qquad C_{2\varepsilon} = 1.92 \qquad C_{1\mu} = 0.09 \qquad \sigma_k = 1.00 \qquad \sigma_\varepsilon = 1.30$$

When used for high Reynolds number flows, this model uses the wall functions to bridge the gap between the fully turbulent fluid core and the stationary wall. These wall functions are semi-empirical formulas relating the local wall shear stress to the mean velocity, turbulent kinetic energy and rate of dissipation. Usually, logarithmic functions are used for this purpose. However, at low Reynolds numbers, the logarithmic wall functions are not valid and wall damping functions are used to ensure that viscous stresses dominate in the near-wall region. The transport equations for k and ε are changed to the following to incorporate the effects of wall damping functions [56]:

$$k \text{ equation}: \quad \frac{\partial(\rho k)}{\partial t} + \frac{\partial(\rho k \bar{u}_i)}{\partial x_i} = \frac{\partial}{\partial x_i}\left[\left(\mu + \frac{\mu_t}{\sigma_k}\right)\frac{\partial k}{\partial x_i}\right] + 2\mu_t \bar{S}_{ij}\bar{S}_{ij} - \rho\varepsilon \tag{2.45}$$

$$\varepsilon \text{ equation}: \quad \frac{\partial(\rho \varepsilon)}{\partial t} + \frac{\partial(\rho \varepsilon \bar{u}_i)}{\partial x_i} = \frac{\partial}{\partial x_i}\left[\left(\mu + \frac{\mu_t}{\sigma_\varepsilon}\right)\frac{\partial \varepsilon}{\partial x_i}\right] + 2 f_1 C_{1\varepsilon}\frac{\varepsilon}{k}\mu_t \bar{S}_{ij}\bar{S}_{ij} - C_{2\varepsilon} f_2 \rho \frac{\varepsilon^2}{k} \tag{2.46}$$

The turbulent viscosity is calculated as follows:

$$\mu_t = \rho C_\mu f_\mu \frac{k^2}{\varepsilon} \tag{2.47}$$

Here, the wall functions f_μ, f_1 and f_2 are themselves functions of turbulence Reynolds numbers (Re_t and Re_y). The following wall damping functions have been proposed [38]:

$$f_\mu = [1 - \exp(-0.0165 Re_y)]^2 \left(1 + \frac{20.5}{Re_t}\right) \qquad f_1 = \left(1 + \frac{0.05}{f_\mu}\right)^3 \qquad f_2 = 1 - \exp(-Re_t^2) \tag{2.48}$$

The modified form of $k - \varepsilon$ equations must be integrated all the way till the wall. The buffer layer between the fully turbulent flow and viscous sublayer near the wall has large gradients of turbulent kinetic energy and dissipation rates. Hence, the mesh must be fine enough to accurately capture such gradients in that region. This places large requirements on the computing system in terms of memory and computational speed to quickly solve the large set of equations for the highly refined mesh. Furthermore, the results can be grid dependent, so multiple simulations may give different results for the same geometric domain and boundary conditions [79].

RNG $k - \varepsilon$ model:
The standard $k - \varepsilon$ model fails to accurately describe the relationship between the turbulence parameters and strain rates. The RNG $k - \varepsilon$ model has been developed for this purpose. This model was derived using a statistical technique called the renormalization group (RNG) theory in 1992. The transport equations for k and ε are given below [82]:

$$k \text{ equation}: \quad \frac{\partial(\rho k)}{\partial t} + \frac{\partial(\rho k \bar{u}_i)}{\partial x_i} = \frac{\partial}{\partial x_i}\left(\alpha_k \mu_{eff}\frac{\partial k}{\partial x_i}\right) + 2\mu_t \bar{S}_{ij}\bar{S}_{ij} - \rho\varepsilon \tag{2.49}$$

$$\varepsilon \text{ equation}: \quad \frac{\partial(\rho \varepsilon)}{\partial t} + \frac{\partial(\rho \varepsilon \bar{u}_i)}{\partial x_i} = \frac{\partial}{\partial x_i}\left(\alpha_\varepsilon \mu_{eff}\frac{\partial \varepsilon}{\partial x_i}\right) + 2C^*_{1\varepsilon}\frac{\varepsilon}{k}\mu_t \bar{S}_{ij}\bar{S}_{ij} - C_{2\varepsilon}\rho\frac{\varepsilon^2}{k} \tag{2.50}$$

The main differences between the standard and the RNG $k - \varepsilon$ models appear in the calculation of effective viscosity (μ_{eff}), analytical formulae for inverse turbulent Prandtl numbers (α_k and α_ε) and the coefficient of turbulent dissipation rate production ($C^*_{1\varepsilon}$) which incorporates the effects of rapid strain rates. The effective viscosity is calculated as the sum of molecular and turbulent viscosity:

$$\mu_{eff} = \mu + \mu_t; \quad \text{where} \quad \mu_t = \rho C_\mu \frac{k^2}{\varepsilon} \quad \text{with} \quad C_\mu = 0.0845 \tag{2.51}$$

The coefficients α_k and α_ε are computed using the following formula derived analytically by the RNG theory:

$$\left|\frac{\alpha-1.3929}{\alpha_0-1.3929}\right|^{0.6321}\left|\frac{\alpha+2.3929}{\alpha_0+2.3929}\right|^{0.3679}=\frac{\mu}{\mu_{eff}} \tag{2.52}$$

Here, $\alpha_0 = 1.0$ and in the limit of high Reynolds number (i.e. when $\mu << \mu_{eff}$), $\alpha_k = \alpha_\varepsilon \approx 1.393$. The major difference between the two $k-\varepsilon$ models is the modification of the term $C_{1\varepsilon}$ to $C^*_{1\varepsilon}$ as follows:

$$C^*_{1\varepsilon} = C_{1\varepsilon} - \frac{\eta(1-\eta/\eta_0)}{1+\beta\eta^3} \qquad \eta = \frac{k}{\varepsilon}\sqrt{2\bar{S}_{ij}\bar{S}_{ij}} \qquad \eta_0 = 4.377 \qquad \beta = 0.012 \tag{2.53}$$

In the above equation, only the constant β can be adjusted, other constants are calculated as a part of the RNG process. This model has been shown to provide accurate predictions using the backward-facing step [82]. However, this model does not always provide accurate results because of the parameter η. This parameter is sensitive to the magnitude strain rate which causes inaccuracy in the dissipation rate prediction [79].

Realisable $k-\varepsilon$ model:
This model is another variation in the $k-\varepsilon$ model family and was proposed by Shih et al. in the year 1995 [70]. It is called "Realisable" because it satisfies certain mathematical conditions derived using the physics of turbulent flows. It differs from the standard model in the following ways:

1. Turbulent viscosity (μ_t) is calculated using the constant C_μ sensitised to the mean strain rate.
2. Transport equation for dissipation rate (ε) is derived from an exact equation for the transport of the mean – square vorticity fluctuation.

The transport equations for k and ε are as follows:

$$k \text{ equation}: \quad \frac{\partial(\rho k)}{\partial t} + \frac{\partial(\rho k \bar{u}_i)}{\partial x_i} = \frac{\partial}{\partial x_i}\left[\left(\mu + \frac{\mu_t}{\sigma_k}\right)\frac{\partial k}{\partial x_i}\right] + 2\mu_t \bar{S}_{ij}\bar{S}_{ij} - \rho\varepsilon \tag{2.54}$$

$$\varepsilon \text{ equation}: \quad \frac{\partial(\rho \varepsilon)}{\partial t} + \frac{\partial(\rho \varepsilon \bar{u}_i)}{\partial x_i} = \frac{\partial}{\partial x_i}\left[\left(\mu + \frac{\mu_t}{\sigma_k}\right)\frac{\partial \varepsilon}{\partial x_i}\right] + \rho C_1 S\varepsilon - \rho C_2 \frac{\varepsilon^2}{k+\sqrt{\nu\varepsilon}} \tag{2.55}$$

where

$$C_1 = \max\left[0.43, \frac{\eta}{\eta+5}\right] \qquad \eta = S\frac{k}{\varepsilon} \qquad S = \sqrt{2\bar{S}_{ij}\bar{S}_{ij}} \tag{2.56}$$

In this model as well, as for other $k-\varepsilon$ models, the turbulent viscosity is calculated as follows:

$$\mu_t = \rho C_\mu \frac{k^2}{\varepsilon} \tag{2.57}$$

The only difference is that C_μ is no longer a constant but now a function of the mean strain and mean rotation rates. It is calculated as follows:

$$C_\mu = \frac{1}{A_0 + A_s\frac{kU^*}{\varepsilon}} \tag{2.58}$$

Here, the quantity U^* is a function of mean strain and mean rotation rates. The effect of mean rotation rate is included only when the frame of reference itself of rotating with some finite angular velocity. The quantity A_s is also a function of mean strain rate. The model constants are as follows:

$$C_2 = 1.90 \qquad \sigma_k = 1.00 \qquad \sigma_\varepsilon = 1.20 \qquad A_0 = 4.04 \tag{2.59}$$

The Realisable $k-\varepsilon$ model is shown to display superior performance over the standard and RNG versions for many kinds of flows. It has produced accurate results for flows involving strong streamline curvature, vortices and rotation. It has also been validated for homogeneous shear flows, free flows, planar and axisymmetric jets, mixing layers, boundary layers and separated flows [70] [32]. However, for all their advantages, usefulness and wide applicability, the $k-\varepsilon$ models do have some well known disadvantages:

- Modification is required for compressible flows. Usually, this is achieved using modification to the model constant C_μ which then becomes a function of the convective Mach numbers and splitting the turbulent kinetic energy dissipation into solenoidal (ε_s) and dilatational (ε_h) contributions [68] [83].
- A more accurate description of the energy exchanges from the integral to the Kolmogorov scale is provided by splitting the energy spectrum into multiple zones each having their own turbulent kinetic energy k_i and dissipation rate ε_i [33]. This is not the case in the standard $k-\varepsilon$ model as it assumes a singular description of the entire spectrum.

$k-\omega$ MODELS

The $k-\varepsilon$ models maybe the widely used models in industry for turbulence modelling but are by no means the only class of two-equation models available for that purpose. Another widely used class of models are the $k-\omega$ models. These models use the turbulent kinetic energy k and the turbulence frequency ω as the two parameters to calculate the turbulent viscosity. As in the $k-\varepsilon$ class, transport equations for the two parameters k and ω are solved to calculate their respective values and eventually, evaluate the turbulent viscosity. The turbulence frequency ω can be thought of as the ratio of the turbulent dissipation rate and turbulent kinetic energy ($\omega = \varepsilon/k$). There are two variations of the $k-\omega$ model widely used for turbulence modelling and are described below.

Standard $k-\omega$ model:
This model was proposed by Wilcox [81] and incorporates modifications for low-Reynolds numbers, compressibility and shear flow spreading. It involves the transport equations for turbulent kinetic energy (k) and turbulence frequency (ω) given below:

$$k\text{-equation}: \quad \frac{\partial(\rho k)}{\partial t} + \frac{\partial(\rho k \bar{u}_i)}{\partial x_i} = \frac{\partial}{\partial x_i}\left[\left(\mu + \frac{\mu_t}{\sigma_k}\right)\frac{\partial k}{\partial x_i}\right] + P_k - Y_k \tag{2.60}$$

$$\omega\text{-equation}: \quad \frac{\partial(\rho \omega)}{\partial t} + \frac{\partial(\rho \omega \bar{u}_i)}{\partial x_i} = \frac{\partial}{\partial x_i}\left[\left(\mu + \frac{\mu_t}{\sigma_\omega}\right)\frac{\partial \omega}{\partial x_i}\right] + P_\omega - Y_\omega \tag{2.61}$$

Here, the terms P_k and P_ω represent the production terms for the two turbulence quantities and Y_k and Y_ω represent their respective dissipation. They are calculated as follows:

$$P_k = 2\mu_t \bar{S}_{ij}\bar{S}_{ij} - \frac{2}{3}\rho k \frac{\partial \bar{u}_i}{\partial x_j}\delta_{ij} \qquad Y_k = \beta^* \rho k \omega \tag{2.62}$$

$$P_\omega = \gamma_1 \left(2\rho \bar{S}_{ij}\bar{S}_{ij} - \frac{2}{3}\rho \omega \frac{\partial \bar{u}_i}{\partial x_j}\delta_{ij}\right) \qquad Y_\omega = \beta_1 \rho \omega^2 \tag{2.63}$$

The model constants are as follows:

$$\sigma_k = 2.000 \qquad \sigma_\omega = 2.000 \qquad \gamma_1 = 0.553 \qquad \beta_1 = 0.075 \qquad \beta^* = 0.090 \tag{2.64}$$

The turbulent viscosity (μ_t) is calculated as follows:

$$\mu_t = \alpha^* \frac{\rho k}{\omega} \tag{2.65}$$

Here, the coefficient α^* is the damping coefficient used for low-Reynolds number corrections. It is calculated as follows:

$$\alpha^* = \alpha^*_\infty \left(\frac{\alpha^*_0 + Re_t / R_k}{1 + Re_t / R_k} \right) \tag{2.66}$$

where

$$Re_t = \frac{\rho k}{\mu \omega} \qquad R_k = 6 \qquad \alpha^*_0 = \frac{\beta_i}{3} \qquad \beta_i = 0.072 \tag{2.67}$$

For high-Reynolds number limit, the coefficient $\alpha^* = \alpha^*_\infty = 1$.
To incorporate additional effects, the production and dissipation terms of the two turbulent quantities may be multiplied by coefficients which are functions of strain rate, rotation rate, frame angular velocity (in case the frame of reference is rotating) and Mach number. This model is useful because it can be directly integrated to the wall and does not require wall-damping functions in low-Reynolds number applications.

SST $k-\omega$ model:
The $k-\varepsilon$ model gives accurate results in the far field region (i.e. the turbulent core) but is inaccurate in the viscous region near the wall. The standard $k-\omega$ model gives accurate results for the near wall region. This has lead to the development of a hybrid model combining the best of both models. Such a model was proposed by Menter [49] [48] [50] [47] and it involves the transformation of standard $k-\varepsilon$ model for the turbulent core into $k-\omega$ model for the near-wall region. The transport equations are as follows:

$$\frac{\partial(\rho k)}{\partial t} + \frac{\partial(\rho k \bar{u}_i)}{\partial x_i} = \frac{\partial}{\partial x_i}\left[\left(\mu + \frac{\mu_t}{\sigma_k} \right) \frac{\partial k}{\partial x_i} \right] + \left(2\mu_t \bar{S}_{ij} \bar{S}_{ij} - \frac{2}{3} \rho k \frac{\partial \bar{u}_i}{\partial x_j} \delta_{ij} \right) - \beta^* \rho k \omega \tag{2.68}$$

$$\frac{\partial(\rho \omega)}{\partial t} + \frac{\partial(\rho \omega \bar{u}_i)}{\partial x_i} = \frac{\partial}{\partial x_i}\left[\left(\mu + \frac{\mu_t}{\sigma_{\omega,1}} \right) \frac{\partial \omega}{\partial x_i} \right] + \gamma_2 \left(2\rho \bar{S}_{ij} \bar{S}_{ij} - \frac{2}{3} \rho \omega \frac{\partial \bar{u}_i}{\partial x_j} \delta_{ij} \right) - \beta_2 \rho \omega^2 + 2 \frac{\rho}{\omega \sigma_{\omega,2}} \frac{\partial k}{\partial x_k} \frac{\partial \omega}{\partial x_k} \tag{2.69}$$

The difference between this $k-\omega$ model and the standard model is evident in the last term of the ω-equation: the cross-diffusion term. This term arises during the transformation of $k-\varepsilon$ model to $k-\omega$ model. There are a few modifications proposed to optimise the model for general purpose CFD application [51]. They are as follows:

1. Model constants are revised to the following:

$$\sigma_k = 1.000 \quad \sigma_{\omega,1} = 2.000 \quad \sigma_{\omega,2} = 1.170 \quad \gamma_2 = 0.440 \quad \beta_2 = 0.083 \quad \beta^* = 0.090 \tag{2.70}$$

2. Blending functions have been introduced to ensure smooth transition from $k-\varepsilon$ model in the turbulent core to $k-\omega$ model near the walls. These blending functions are functions of turbulent length (l_t), distance from the wall and turbulent Reynolds number (Re_y). They tend to unity in the turbulent core and evaluate to zero at the walls.

3. The turbulent viscosity is limited via mathematical restrictions to ensure accurate results in adverse pressure regions and wake regions. Turbulent kinetic energy production is also mathematically limited to prevent the build-up of turbulence in stagnation regions.

$$\mu_t = \frac{a_1 \rho k}{\max(a_1 \omega, S F_2)} \qquad P_k = \min\left(10 \beta^* \rho k \omega,\ 2\mu_t \bar{S}_{ij} \bar{S}_{ij} - \frac{2}{3} \rho k \frac{\partial \bar{u}_i}{\partial x_j} \delta_{ij} \right) \tag{2.71}$$

where $S = \sqrt{2 \bar{S}_{ij} \bar{S}_{ij}}$, a_1 = constant and F_2 is a blending function.

This model too can be integrated to the wall without the need for any wall-damping functions. It has shown superior performance for aerodynamic applications [48]. For general purpose CFD simulations, both standard and SST $k-\omega$ have similar advantages and disadvantages as $k-\varepsilon$ models. All of these models fail to subtly describe the individual Reynolds stresses, which can only be done using Reynolds stress model.

2.1.4. CONSERVATION OF ENERGY

Any reacting flow would involve the exchange of energy between the various species involved and also between the contents of the computational domain and the boundaries. The principle of conservation of energy states that energy must remain conserved during all such interactions. There are various forms of energy conservation equation that can be used for chemically reacting flows. Equations for conservation of internal energy, enthalpy and their sensible versions (component due to temperature changes) and total versions (sensible and kinetic energies) exist and the choice of equation depends upon the nature of the system to be analysed. This thesis involves the solution of the conservation equation for total non-chemical energy defined as follows:

$$E = h_s - \frac{p}{\rho} + \frac{v^2}{2} \qquad \text{(sum of sensible and kinetic energies)} \tag{2.72}$$

Here, h_s is the sensible enthalpy, p is pressure, ρ is density and v is the velocity. The total sensible enthalpy is the mass-weighted sum of individual sensible enthalpies for all the species involved. It is defined as follows:

$$h_s = \sum_{k=1}^{N} Y_k h_{s,k} + \frac{p}{\rho} \tag{2.73}$$

where the sensible enthalpy for an individual component is defined as the integral of specific heat capacity at constant pressure between the reference temperature (T_{ref}, usually 298.15 K) and given temperature (T) as follows:

$$h_{s,k} = \int_{T_{ref}}^{T} c_{p,k} dT \tag{2.74}$$

The energy conservation equation is given below:

$$\frac{\partial(\rho E)}{\partial t} + \frac{\partial(\rho u_i E)}{\partial x_i} = \dot{\omega}_T + \frac{\partial}{\partial x_i}\left(\lambda \frac{\partial T}{\partial x_i}\right) - \frac{\partial}{\partial x_i}\left(\rho \sum_{k=1}^{N} h_{s,k} Y_k V_{k,i}\right) + \frac{\partial}{\partial x_i}(\tau_{ij} u_j) + \dot{Q} \tag{2.75}$$

Here, the first term on the RHS represents the energy source due to chemical reactions. It is calculated as the sum of the formation enthalpies of individual species multiplied with their formation rates:

$$\dot{\omega}_T = -\sum_{k=1}^{N} \Delta h^0_{f,k} \dot{\omega}_k \tag{2.76}$$

The second term on the RHS represents energy exchange due to conduction and the third term represents energy exchange due to species diffusion. The last term ($\dot{Q}$) represents extra energy sources (for example due to lasers, electric spark, radiation etc.). When solving for turbulent flows, the effects of fluctuations of the flow properties also come into picture and must be accurately modelled to get acceptable results.

2.1.5. SPECIES TRANSPORT EQUATIONS

As the combustion proceeds inside a combustion chamber, the mass of individual species is not conserved. The reactants are consumed and the products are formed as the reaction proceeds.

However, the transport and net rate of production of each species must be mathematically documented for each control volume. For a species k, the transport equation solved over a control volume is as follows:

$$\frac{\partial(\rho Y_k)}{\partial t}+\frac{\partial(\rho u_i Y_k)}{\partial x_i}=-\frac{\partial}{\partial x_i}(V_{k,i}Y_k)+\dot{\omega}_k \tag{2.77}$$

Here, the quantity V_k represents the diffusion velocity of species k. The equation written above is valid for laminar flows containing no fluctuating terms. For turbulent flows, the equation modifies to as follows:

$$\frac{\partial(\bar{\rho}\tilde{Y}_k)}{\partial t}+\frac{\partial(\bar{\rho}\tilde{u}_i\tilde{Y}_k)}{\partial x_i}=-\frac{\partial}{\partial x_i}(\overline{V_{k,i}Y_k}+\bar{\rho}\widetilde{u_i''Y_k''})+\bar{\dot{\omega}}_k \tag{2.78}$$

The above equation holds true for compressible flows, hence Favre averages are used instead of Reynolds averages. There is an extra term adding to the diffusion velocity of the species. This species turbulent flux ($\bar{\rho}\widetilde{u_i''Y_k''}$) is an unclosed term and must be modelled accurately. It is modelled similar to the laminar diffusive term ($\overline{V_{k,i}Y_k}$), using the Fick's diffusion law as follows:

$$\overline{V_{k,i}Y_k}=-\overline{\rho D_k\frac{\partial Y_k}{\partial x_i}}\approx-\bar{\rho}\bar{D}_k\frac{\partial\tilde{Y}_k}{\partial x_i} \qquad \bar{\rho}\widetilde{u_i''Y_k''}=-\frac{\mu_t}{Sc_{kt}}\frac{\partial\tilde{Y}_k}{\partial x_i} \tag{2.79}$$

Here, D_k is the diffusion constant and Sc_{kt} is the turbulent Schmidt number for species k. In a turbulent flow, mass diffusion is dominated by turbulent transport and the Schmidt number does not usually vary for different species. The most important term in the turbulent equation is the species net production rate ($\bar{\dot{\omega}}_k$). It is an unclosed term and most turbulent combustion research has been devoted to accurate modelling of this term. There are two approaches proposed for this purpose:

- **Primitive variable method**: This method involves solving for only the flow variables and mixing of various species together. The mixing is calculated via a quantity called the mixture fraction (denoted by z), which can be thought of as the local ratio of burnt and unburnt fuel stream elements in all species involved. The various species mass fraction and temperature values are then calculated as a function of mixture fraction. Usually, the mixture fraction is related to all these variables via a probability density function ($p(z^*)$).

- **Reaction rate approach**: This method involves solving the balance equations for all the species and temperature individually. This leads to all these quantities being evaluated relatively independently of each other. This method is preferable in cases of compressible combustion and also when heat sources and sinks have to be taken into account [61].

For both these approaches, two types of chemistries can be considered: infinitely fast chemistry and finite-rate chemistry. Infinitely fast chemistry involves the assumption that chemical time scales are much shorter than flow and diffusion (both molecular and turbulent) time scales. Hence, the net rate of production of species is controlled only by flow and diffusion processes. Finite rate chemistry involves no such assumption and considers chemical reaction rates along with flow and diffusion rates while calculating the net rate of formation of all the species. The above mentioned two methods are described in detail below.

PRIMITIVE VARIABLE METHOD

As mentioned above, this method involves solving for only flow variables and calculating mixing of various species using the mixture fraction (z). Balance equations for mean mixture fraction ($\tilde{z}$) and its variance ($\widetilde{z''^2}$) are solved and corresponding species mass fractions and temperature are calculated. The balance equations for $\tilde{z}$ and $\widetilde{z''^2}$ are given below [28]:

$$\frac{\partial(\bar{\rho}\tilde{z})}{\partial t}+\frac{\partial(\bar{\rho}\tilde{u}_i\tilde{z})}{\partial x_i}=\frac{\partial}{\partial x_i}\left[\left(\frac{\mu_t}{\sigma_t}\right)\frac{\partial\tilde{z}}{\partial x_i}\right] \tag{2.80}$$

$$\frac{\partial(\bar{\rho}\widetilde{z''^2})}{\partial t} + \frac{\partial(\bar{\rho}\tilde{u}_i\widetilde{z''^2})}{\partial x_i} = \frac{\partial}{\partial x_i}\left[\left(\frac{\mu_t}{\sigma_t}\right)\frac{\partial\widetilde{z''^2}}{\partial x_i}\right] + 2\left(\frac{\mu_t}{\sigma_t}\right)\left(\frac{\partial\tilde{z}}{\partial x_i}\right)^2 - C_D\bar{\rho}\frac{\varepsilon}{k}\widetilde{z''^2} \tag{2.81}$$

Here, σ_t is the turbulent Schmidt number (default value 0.7) and C_D is a constant equal to 2.0.
For **infinitely fast chemistry**, the species mass fractions and temperature values are directly related to mean mixture fraction values via a probability density function $p(z)$ as follows:

$$\bar{\rho}\tilde{Y}_k = \int_0^1 \rho(z^*)Y_k(z^*)p(z^*)dz^* \qquad \bar{\rho}\tilde{T} = \int_0^1 \rho(z^*)T(z^*)p(z^*)dz^* \tag{2.82}$$

The average values of species mass fractions and temperatures can also be calculated in terms of mass-weighted probability function as follows:

$$\tilde{Y}_k = \int_0^1 Y_k(z^*)\tilde{p}(z^*)dz^* \qquad \tilde{T} = \int_0^1 T(z^*)\tilde{p}(z^*)dz^* \tag{2.83}$$

where $\tilde{p}(z^*)$ is evaluated as:

$$\tilde{p}(z^*) = \frac{\rho(z^*)p(z^*)}{\bar{\rho}} \tag{2.84}$$

The probability density function (pdf) may either be assumed or calculated by solving an appropriate balance equation. The most widely used probability density function is evaluated using the β-function. Its simplicity and popularity is attributed to its dependence on only two parameters: mean mixture fraction $\tilde{z}$ and its variance $\widetilde{z''^2}$ as follows:

$$\tilde{p}(z) = \frac{1}{B(a,b)}z^{a-1}(1-z)^{b-1} = \frac{\Gamma(a+b)}{\Gamma(a)\Gamma(b)}z^{a-1}(1-z)^{b-1} \tag{2.85}$$

Here, the normalisation factor $B(a,b)$ and the Gamma function $\Gamma(x)$ are defined as follows:

$$B(a,b) = \int_0^1 z^{a-1}(1-z)^{b-1}dz \qquad \Gamma(x) = \int_0^{+\infty} e^{-t}t^{x-1}dt \tag{2.86}$$

The pdf parameters a and b are also determined using the mean mixture fraction ($\tilde{z}$) and its variance ($\widetilde{z''^2}$) as follows:

$$a = \tilde{z}\left[\frac{\tilde{z}(1-\tilde{z})}{\widetilde{z''^2}} - 1\right] \qquad b = \frac{a}{\tilde{z}} - a \tag{2.87}$$

Once, the pdf is completely determined, the integrals in equations (2.82) and (2.83), are evaluated and stored in look-up tables. Once the flow variables (density, velocity and turbulence parameters) are evaluated using conservation equations and mixing is calculated using mixture fraction, the corresponding species and temperature values are simply interpolated from the look-up tables.
The **finite-rate chemistry** case is more complicated than the procedure explained above. In this case, the species mass fractions and temperature values are not uniquely related to the mixture fraction but also depend on the Damköhler number (Da). This number may be defined as

$$Da = \frac{\tau_f}{\tau_c} \qquad \text{where } \tau_f = \text{flow time scale and } \tau_c = \text{chemical time scale} \tag{2.88}$$

To incorporate this extra dependence, the laminar flamelet concept is extensively used and may be extended to Conditional Moment Closure (CMC) and pdf balance equations. These three approaches are described briefly below:

- **Flamelet approach**: This approach assumes turbulent flames to be composed of small laminar flamelets [57]. For sufficiently large Da values, the reaction zones are assumed thin compared to turbulent flow scales. The simplest approach in this case is to assume dependence on stoichiometric scalar dissipation rate (χ_{st}). Scalar dissipation rate is defined as follows:

$$\chi = 2D\left(\frac{\partial z}{\partial x_i}\frac{\partial z}{\partial x_i}\right) \qquad \text{where } D = \text{representative diffusion coefficient} \tag{2.89}$$

and χ_{st} is the above quantity evaluated at stoichiometric mixture fraction value (z_{st}). The mean species mass fractions and temperature values are calculated as follows:

$$\bar{\rho}\tilde{Y}_k = \int_0^{+\infty}\int_0^1 \rho Y_k(z,\chi_{st})p(z,\chi_{st})dzd\chi_{st} \tag{2.90}$$

$$\bar{\rho}\tilde{T} = \int_0^{+\infty}\int_0^1 \rho T(z,\chi_{st})p(z,\chi_{st})dzd\chi_{st} \tag{2.91}$$

where $p(z,\chi_{st})$ is the joint pdf for mixture fraction and stoichiometric scalar dissipation rate. Usually, statistical independence is assumed, leading to the following:

$$p(z,\chi_{st}) = p(z)p(\chi_{st}) \tag{2.92}$$

Here, as for infinitely fast chemistry, assumed functions are used to evaluate the appropriate probabilities. Usually β-function is used to evaluate $p(z)$. To evaluate $p(\chi_{st})$ Dirac-delta function may be used [59] or log normal distribution [16].

- **Conditional Moment Closure (CMC) approach**: This approach involves the derivation, closure and solution of exact balance equations for conditional species mass fractions [34]. The conditional mass fraction of any species k is the mean of the product $\left(\overline{\rho Y_k|z^*}\right)$ evaluated at $z = z^*$. The average mass fraction is evaluated as follows:

$$\bar{\rho}\tilde{Y}_k = \int_0^1 \left(\overline{\rho Y_k|z^*}\right) p(z^*)dz^* \tag{2.93}$$

  The above mentioned approaches invlove the assumption of statistical independence of density and species mass fractions:

$$\left(\overline{\rho Y_k|z^*}\right) = \rho(z^*)Y_k(z^*) \tag{2.94}$$

  whereas this approach involves exact evaluation of the conditional moments from their respective balance equations. The probability density function $p(z^*)$ is generally presumed from $\tilde{z}$ and $\widetilde{z''^2}$. Multiple balance equations for different values of z^* are required. Hence, this approach can be computationally quite expensive.

- **Balance equations for pdfs**: Balance equations for probability density functions can be derived and solved, but that requires additional assumptions to evaluate species mass fractions and temperatures from mixture fraction and scalar dissipation rate. Hence, this approach is generally adopted when explicitly calculating the mass fractions and temperature values using mean reaction rate approach.

REACTION RATE APPROACH

As mentioned above, this approach involves the explicitly solving the conservation equation for each species and for temperature. It is adopted for compressible combustion cases and also when heat loss/gain has to be calculated.
When assuming **infinitely fast chemistry**, several models are available to calculate the mean species production rate ($\bar{\dot{\omega}}_k$). They are explained as follows:

- **Eddy-Dissipation model**: This model was devised to estimate the net production rate of the various species from turbulent mixing time, estimated from integral length and time scales

[45]. The net rate of production of species k due to reaction r is taken as the smaller value amongst the following expressions:

$$\bar{\dot{\omega}}_{k,r} = \nu'_{k,r} M_{w,k} A \rho \frac{\varepsilon}{k} \min_{\mathscr{R}} \left(\frac{Y_{\mathscr{R}}}{\nu'_{\mathscr{R},r} M_{w,\mathscr{R}}} \right) \tag{2.95}$$

$$\bar{\dot{\omega}}_{k,r} = \nu'_{k,r} M_{w,k} A B \rho \frac{\varepsilon}{k} \left(\frac{\sum_P Y_P}{\sum_{j=1}^{N} \nu''_{j,r} M_{w,j}} \right) \tag{2.96}$$

Here, A and B are empirical constants equal to 4.0 and 0.5 respectively. Other symbols are:

$\nu'_{k,r}$ = stoichiometric coefficient of species k in reaction r

$\nu''_{j,r}$ = stoichiometric coefficient of product species j in reaction r

$M_{w,k}$ = molecular weight of species k

Y_P = mass fraction of any product species P

$Y_{\mathscr{R}}$ = mass fraction of a particular reactant $\mathscr{R}$

The only limiting factor in this case is the turbulence, which slowly convects and mixes fuel and oxidiser in the reaction zones, where they immediately form the products. The appearance of large-eddy mixing time scale (k/ε) signifies this assumption mathematically.

- **Finite-rate/Eddy-Dissipation model**: This model combines the Eddy-Dissipation model and Finite-Rate model based on Arrhenius expressions. The lower of the two rate expressions is used for calculations. This is especially useful for premixed combustion simulations, which would otherwise be uncontrolled as the reaction would immediately start as the reactants enter the computational domain. This provides a physical control for the reactants and prevents them from prematurely combusting.

Note: The Eddy-Dissipation model and Finite-rate/Eddy-Dissipation model are useful only for one or two-step mechanisms. For multi-step detailed mechanisms, they may provide incorrect results as all the reactions are controlled by the same turbulent rate parameters whereas the physical reactions are governed by different Arrhenius rates [2].

When assuming **finite-rate chemistry**, one popular model has been extensively used in industry and academia, the Eddy Dissipation Concept (EDC) model. It is an extension of the Eddy-Dissipation model to include detailed chemical mechanisms in turbulent flows [44]. The basic assumption is that chemical reactions take place in small turbulent scales called fine scales. Length and time scales have been defined as follows [23]:

$$\text{Length fraction}: \xi^* = C_\xi \left(\frac{\nu \varepsilon}{k} \right)^{1/4} \qquad \text{Time scale}: \tau^* = C_\tau \left(\frac{\nu}{\varepsilon} \right)^{1/2} \tag{2.97}$$

Volume fraction is calculated as $(\xi^*)^3$. The reaction is assumed to occur at constant pressure over the time scale τ^*, with initial conditions taken as the current species and temperature in the cell. Since detailed mechanisms are numerically stiff (because of large variation in time scales of different reactions), the In-Situ Adaptive Tabulation (ISAT) algorithm is used for numerical integration. ISAT has been reported to accelerate the calculations by two to three orders of magnitude, offering substantial reductions in run-times [62]. The net rate of production of species k is then calculated as follows:

$$\bar{\dot{\omega}}_k = \frac{\rho (\xi^*)^2}{\tau^* \left[1 - (\xi^*)^3 \right]} \left(Y_k^* - Y_k \right) \tag{2.98}$$

where Y_k^* is the fine-scale species mass fraction after reacting over the time τ^*. However, this method is computationally quite expensive, but can yield accurate results.

2.1.6. RADIATION MODELLING

Radiative heat transfer is the exchange of energy in the form of electromagnetic waves or streams of photons. When analysing any combustion equipment, it is necessary to account for radiative heat transfer as its magnitude is quite comparable to that of convective heat transfer. During combustion processes of engineering interest, the temperatures achieved generally fall between 1000-1500 K. For even higher temperatures, the electromagnetic radiation will be emitted at wavelengths visible to the naked eye [79]. Hence, industrial combustion is generally accompanied by emission of heat as well as visible light.

Atmospheric air at combustion temperatures does not participate in radiative heat transfer as it doesn't readily absorb infrared radiation. However, the product of combustion contains large amount of carbon dioxide and water vapour. These two gases readily absorb and emit infrared radiation. Hence, accounting for this energy exchange is necessary. There is no direct coupling between the flow properties and radiation as the radiation properties of fluids don't depend directly on fluid velocity. However, the flow modifies the distribution of temperature and various species. Hence, radiation and flow are indirectly coupled.

The net radiative exchange within a control volume appears as a source/sink term in the energy equation. Figure (2.5) shows the schematic diagram of a control volume indicating the steady state energy balance and the difference made by radiative heat transfer.

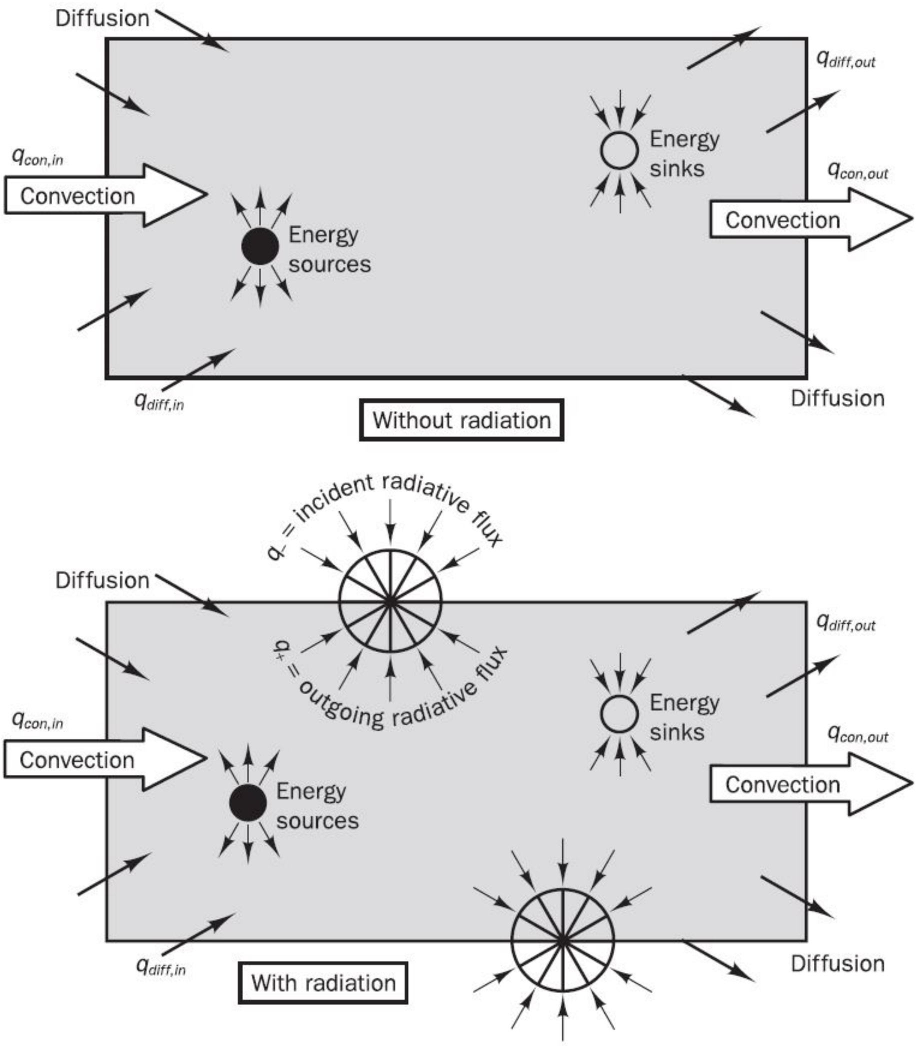

Figure 2.5: Energy balance with and without radiation [79]

The net energy source term without radiation is the balance between diffusion and convection as follows:

$$\int_{CV} S_h dV = \int_A \mathbf{q}_{conv}.\mathbf{n}dA + \int_A \mathbf{q}_{diff}.\mathbf{n}dA \tag{2.99}$$

However, when radiation is also considered, the source term modifies to as follows:

$$\int_{CV} S_h dV + \int_{CV} S_{h,rad} dV = \int_A \mathbf{q}_{conv}.\mathbf{n}dA + \int_A \mathbf{q}_{diff}.\mathbf{n}dA + \int_A \mathbf{q}_{rad}.\mathbf{n}dA \tag{2.100}$$

Here **q** represents the respective heat flux, which is then integrated over the whole area (A) and S_h represents the respective volumetric source term, which is then integrated over the whole control volume (CV). The mean volumetric radiative source term ($\bar{S}_{h,rad}$) can be expressed as follows:

$$\bar{S}_{h,rad} = \frac{1}{\Delta V}\int_A \mathbf{q}_{rad}.\mathbf{n}dA = \frac{1}{\Delta V}\int_A (q_- - q_+)dA \tag{2.101}$$

where q_- and q_+ are indicated in Figure (2.5). This source term can be substituted for the source term $\dot{Q}$ in the energy conservation equation (2.75). The incoming (q_-) and outgoing (q_+) radiative fluxes are calculated by integrating the incoming (I_-) and outgoing (I_+) radiative intensities over all the possible directions. Radiative intensity is defined as the heat flux per unit area perpendicular to the rays per unit solid angle and it varies with direction as well. The integration of intensity over a unit hemisphere just outside the control volume boundary. For incoming flux, the hemisphere outside the control volume is considered. For outgoing flux, the hemisphere inside the control volume is considered. The integrals are evaluated as follows:

$$q_- = \int_{2\pi} I_-(\mathbf{s})\mathbf{s}.\mathbf{n}d\Omega = \int_0^{2\pi}\int_0^{\pi/2} I_-(\theta,\phi)cos(\theta)sin(\theta)d\theta d\phi \tag{2.102}$$

$$q_+ = \int_{2\pi} I_+(\mathbf{s})\mathbf{s}.\mathbf{n}d\Omega = \int_0^{2\pi}\int_{\pi/2}^{\pi} I_+(\theta,\phi)cos(\theta)sin(\theta)d\theta d\phi \tag{2.103}$$

The co-ordinate system is shown in Figure (2.6). Here, **n** is the outward pointing normal to the surface. If we place this coordinate system at the required boundary point of the control volume, then the integrals in Equations (2.102) and (2.103) can be understood with proper integration limits. The intensity (I) is a function of the direction vector, **s** and the dot product (**s**.**n**) indicates the component of the intensity perpendicular to the area. The next step is to calculate the intensities (I_- and I_+) for integration. This is done by solving the **Radiative Transport Equation (RTE)** in a participating medium. It is derived by considering the balance for radiative energy at a position **r** travelling in the direction **s** within a small pencil of rays. The equation is as follows [79]:

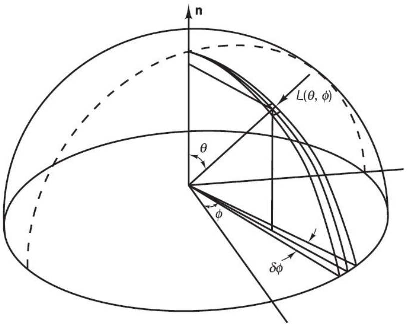

Figure 2.6: Spherical co-ordinates [79]

$$\frac{dI(\mathbf{r},\mathbf{s})}{ds} = \kappa I_b(\mathbf{r}) - \kappa I(\mathbf{r},\mathbf{s}) - \sigma_s I(\mathbf{r},\mathbf{s}) + \frac{\sigma_s}{4\pi}\int_{4\pi} I_-(\mathbf{s}_i)\Phi(\mathbf{s}_i,\mathbf{s})d\Omega_i \tag{2.104}$$

Here, $I(\mathbf{r},\mathbf{s})$ is the intensity at position **r** in the direction **s**, $I_b(\mathbf{r})$ is the blackbody intensity emitted by the fluid at position **r**, κ is the absorption coefficient σ_s is the scattering coefficient, $I_-(\mathbf{s}_i)$ is the incoming intensity and $\Phi(\mathbf{s}_i,\mathbf{s})$ is the scattering phase function. The second and third terms on RHS are clubbed together by an extinction coefficient β as follows [79]:

$$\frac{dI(\mathbf{r},\mathbf{s})}{ds} = \kappa I_b(\mathbf{r}) - \beta I(\mathbf{r},\mathbf{s}) + \frac{\sigma_s}{4\pi}\int_{4\pi} I_-(\mathbf{s}_i)\Phi(\mathbf{s}_i,\mathbf{s})d\Omega_i \tag{2.105}$$

where $\beta = \kappa + \sigma_s$. Equation (2.105) is solved to get the radiative intensity at all the points in the computational domain and the appropriate boundary conditions are applied. There are many general-purpose algorithms available for solving the equation.

- Monte Carlo Method [24]: This is a ray tracing method and involves simultaneous random release of a large number of energy particles (or rays) in the participating medium and tracking their progress. It is the most general and versatile of all the models and can be used to generate error estimates. Hence it is used for benchmarking and validation of other models. However, it is computationally very expensive, hence not available in commercial CFD codes.

- Discrete Transfer Radiation Method (DTRM) [41]: This is again a ray tracing method which involves discretizing the computational domain into homogeneous surface and volume elements. Rays are emitted from the centre of each boundary surface element in certain discretized angles and their progress is tracked. It is an economical general purpose algorithm and has been successfully applied to combustion problems. However, it is non-conservative in nature but a conservative version has been developed [13].

- Discrete Ordinates (DO) Method [7] [25]: This method involves the discretization of the total 4π solid angle into finite number of discrete directions and solving the equation for each direction. The integrals over the directions are replaced by numerical quadrature. Thus, the transfer equation is approximated by the following equation:

  $$\frac{dI(\mathbf{r},\mathbf{s}_i)}{ds} = \kappa I_b(\mathbf{r}) - \beta I(\mathbf{r},\mathbf{s}_i) + \frac{\sigma_s}{4\pi}\sum_{j=1}^{n} w_j I_-(\mathbf{s}_j)\Phi(\mathbf{s}_i,\mathbf{s}_j) \tag{2.106}$$

  where w_j are the quadrature weights associated with directions $\mathbf{s}_j$. The accuracy of the solution increases with the increase in number of discretized angles. The direction cosines of the directions $\mathbf{s}_j$ and their respective weights w_j have been tabulated in the literature [39]. This method is quite efficient in providing accurate results and can be used for scattering and non-scattering cases. However, it is non-conservative in nature and can suffer from 'ray effects', due to the nature of discretization and formulation.

- Finite volume method [12] [11] [10]: This method involves discretization of the whole computational domain into small control volumes and integration of the intensity equation for each volume. It is quite similar to the DO Method but the main difference is that this is conservative in nature. Like the DO method, it also involves the discretization of the total 4π solid angle into finite number of discrete directions and solution of intensity equations for each direction. However, the main difference is that this method involves the integration of the intensity equation over all control angles, instead of numerical quadrature and their respective weights. This method is flexible enough to be applied to arbitrary geometries.

Note: The above list mentions that some methods are conservative and others are non-conservative. Conservative methods ensure that the sum of all radiative fluxes over the boundary surfaces is zero whereas non-conservative methods don't ensure that. Hence, conservative methods ensure conservation of radiative energy whereas non-conservative methods don't.

The final step towards radiation modelling is the evaluation of the fluid radiative properties such as absorption coefficient (κ), scattering coefficient (σ_s) and the scattering phase function ($\Phi(\mathbf{s}_i,\mathbf{s})$). These properties depend upon the pressure, temperature and composition of the combusting mixture. The properties of individual species also depend upon its pressure and temperature. There are many methods available for estimating the total properties of individual species over the entire range and for estimating the average values of the mixture. The most widely used model for calculating mixture properties is the Weighted Sum of Grey Gases Model (WSGGM). It assumes the individual species to emit grey radiation and the total emissivity of the mixture over the distance s is calculated as follows:

$$\epsilon = \sum_{i=0}^{N} a_{\epsilon,i}(T)(1 - e^{-\kappa_i p s}) \tag{2.107}$$

where N is the total number of species, $a_{\epsilon,i}$ is the weighting factor for species i, κ_i is the absorption coefficient for species i and p is the sum of partial pressures of all the absorbing species. The weighting factors $a_{\epsilon,i}$ and absorption coefficients κ_i for various gases are tabulated in literature [72] [14]. The absorption coefficient for species $i = 0$ is assigned zero value to account for the gaps in the spectrum between high absorption regions and the weighting factor is calculated as follows:

$$a_{\epsilon,0} = 1 - \sum_{i=1}^{N} a_{\epsilon,i} \tag{2.108}$$

The temperature dependence of weighting factors is approximated by a polynomial function as follows:

$$a_{\epsilon,i} = \sum_{j=1}^{J} b_{\epsilon,i,j} T^{j-1} \tag{2.109}$$

where $b_{\epsilon,i,j}$ are the temperature coefficients for species i. The coefficients $b_{\epsilon,i,j}$ and κ_i are obtained by fitting the experimentally derived data of total emissivities into Equation (2.107) [72] [14] [15]. The absorptivity can be derived in the same manner but is assumed equal to emissivity [54]. The two main species participating in radiative exchange are carbon-dioxide (CO_2) and water vapour (H_2O). The values of various coefficients have been tabulated in literature [72] [14].

2.2. COMBUSTION MECHANISMS

In real combustion systems, the reaction hardly takes place in a single step or in a unidirectional irreversible manner. Hence, an accurate simulation of combustion involves choosing an appropriate mechanism that can properly predict the species, which indirectly controls the temperature values. An appropriate example is the use of proper mechanism to predict hydrogen combustion [60]. There are many mechanisms proposed in the literature for methane and higher hydrocarbons, along with proper transport coefficients. These mechanisms have been categorised on the basis of their level of detail into the following:

- Detailed mechanisms: They describe the detailed combustion process with tens of species and hundreds of reactions. Consequently, they are computationally very expensive and only used when detailed predictions of even the trace species are required.

- Intermediate mechanisms: They are analytically derived from global mechanisms by using mathematical reduction techniques and their reaction rates may contain species that are not present within the reduced set. They usually contain a couple of tens of species and steps.

- Global mechanisms: They consist of maximum a couple of steps with a couple of species. They are the simplest of mechanisms and computationally least expensive. The general structure is the reactant transforming into the product with a couple of intermediates.

Detailed mechanisms consist of the formation of all the species from building elements participating in elementary reactions. As mentioned above, they are computationally very expensive and provide accurate species and temperature predictions, also helping in pollutant predictions. The most famous set of detailed mechanisms are the GRI mechanisms consisting of three versions: GRI 1.2, GRI 2.11 and GRI 3.0. GRI 1.2 consists of 32 species participating in 175 reactions. It has been designed specifically for natural gas combustion [19] [20]. GRI 2.11 is an improvement over 1.2 by including the relevant nitrogen chemistry and reburning process. It consists of 49 species participating in 277 reactions [5]. GRI 3.0 is the latest available mechanism and is an improvement over 2.11, consisting of 53 species participating in 325 reactions [71]. Another contemporary detailed mechanism has been proposed by Glarborg et al. consisting of 65 species participating in 447 reversible reactions which models the interaction of C_1 and C_2 hydrocarbons with nitric oxide (NO) under reducing conditions in a flow reactor [22].

Intermediate mechanisms consist of reduced and skeletal mechanisms. They provide intermediate level of detail between global and detailed mechanisms. They do not capture the formation of every species from elementary reactions and elements, rather their net formation rate is calculated using complex expressions that may contain species not included in the intermediate set. These mechanisms are very popular in academia and industry as they provide the perfect balance between extreme detail and simplification. Quite a large number of intermediate mechanisms have been proposed in the literature. Most of them have been derived from GRI mechanisms, others have been independently formulated. The DRM mechanisms (DRM 19 and DRM 22) have been formulated by reducing GRI 1.2 mechanism [31]. Other mechanisms formulated by reducing GRI 1.2 mechanism have been proposed by Chang and Chen and are available in literature as well [8] [9]. Lu and Law's mechanisms have also been formulated by reducing GRI mechanisms. A 13-species reduced mechanism and a 17-species skeletal mechanism for lean methane-air flames are based on GRI 1.2 mechanism [67]. A 19-species reduced mechanism, and a 30-species skeletal mechanism for methane-air flames is based on GRI 3.0 mechanism [43]. Finally, a reduced mechanism has been derived from GRI 3.0 mechanism and proposed by Msaad et al, consisting of 13 species participating in 9 reactions. This mechanism has been validated against the parent detailed mechanism and is found accurate for a wide range of equivalence ratios and high pressures as well [55]. A reduced mechanism has been proposed by Mendiara et al. which is derived from the mechanism proposed by Glarborg et al. They first formulated a skeletal mechanism on the basis of sensitivity analysis and reaction-rate analysis, followed by systematic reduction based on steady-state hypothesis and partial equilibrium assumption. The resulting reduced mechanism consists of 22 species participating in 18 reactions and has been validated against the parent detailed mechanism [46]. Finally, an independently formulated mechanism was proposed by Smooke et. al. containing 16 species participating in 46 reactions [73].

Global mechanisms are derived from detailed mechanisms on the basis of two assumptions: quasi-steady state and partial equilibrium approximation. This involves assuming that some intermediate species and elementary reactions have reached equilibrium state and do not evolve with time anymore. These mechanisms are computationally least expensive, but may cost accuracy. The simplest global mechanism for methane combustion is one-step which directly reacts methane with oxygen to form carbon-dioxide and water. It is generally not advisable to use this mechanism as the predicted temperature values may be erroneous. However, two and four-step mechanisms have been suggested which may provide good initial estimates for most engineering applications. A two-step mechanism has been tested for combustion stability in gas-fueled swirled burner by Franzelli et al [18]. A general four-step mechanism has been proposed by Jones and Lindstedt which can be used for hydrocarbons upto butane (C_4) with some modifications in the rate constants [27].

3

LITERATURE REVIEW

This chapter provides an overview about the previous studies consisting of the CFD analysis of radiant tube heaters. While perusing the scientific literature, the complete and detailed analysis of radiant tubes using proper CFD principles and techniques was found scarce. However, this does not imply that the interest in radiant tubes has diminished, only that people have mostly carried out rough analysis using basic conservation principles and have found the results to be acceptable and sufficient for their respective purposes.

3.1. EARLY WORK

This thesis is concerned with the analysis of single-ended recirculating radiant tubes fired using self-recuperative burners using natural gas as the fuel. The first of such tubes was developed in Germany in the 1940s and further development was carried out in the 1950s, with a proper model being developed in 1955. In the early 1960s, two British gas industry groups were involved in further development of the tubes. Soon, many manufacturers were licensed to produce and develop more tubes and this led to the development of various industrial applications in batch and continuous heat treatment furnaces. These tubes soon gained rapid popularity in the rest of Europe and this led to the ever growing base of metallic and ceramic high-temperature materials being used for their manufacture. Similar developments took place in Japan in the 1970s and 1980s. In the late 1980s, further development took place in the United States when ceramic regenerators were successfully applied to 'U' and 'W' shaped radiant tubes for steel-industry strip line installations. Soon, the Japanese manufacturers took up the regenerative design challenge and now, the use of single-ended self recuperative radiant tubes is considered an "industry standard" application [30].

3.2. COMPUTATIONAL AND EXPERIMENTAL STUDIES

At the turn of the millennium, further studies were done both in the computational and experimental domain. As the computing power increased, complete three-dimensional numerical analyses of the processes inside the radiant tubes has become economically feasible. The same can also be said for sophisticated experimental setups, making accurate measurements possible. This section describes some of the studies done on both the fronts by various researchers.

3.2.1. WORK DONE BY JÄGER ET AL.

One of the earliest studies on radiant tubes was found to be conducted at RWTH Aachen in Germany by Jäger et al. in 2005 [26]. They carried out numerical studies on a radiant tube burner of the capacity range 20-40 kW fired using combustible fuel oil and gas. Their setup (as shown in Figure (3.1a)) was a little different from those analysed in this thesis. It has a long vaporisation tube into which the burner efflux is injected followed by a longer flame tube, with an intermediate flue gas recirculation region. The air inlet is staged, with primary air entering with the fuel in the vaporisation region and secondary air directly entering over the recirculation gap. The ratio of primary and secondary air can be controlled by external means. The secondary air is heated via self-recuperation method as shown in the figure. This setup was analysed using CFD techniques and the variation of NO_x and CO emissions was studied. At a burner capacity of 39 kW and a furnace temperature of 1004°C, the emissions were found to be minimum. The variation of emissions and various temperature values with secondary air fraction ($\Lambda_{air,2}$) is shown in Figure (3.1b). Calculations were also performed for cold flow case, i.e., without combustion, to calculate the amount of flue gas recirculation inside the radiant tube and the results showed a good agreement with experimental data.

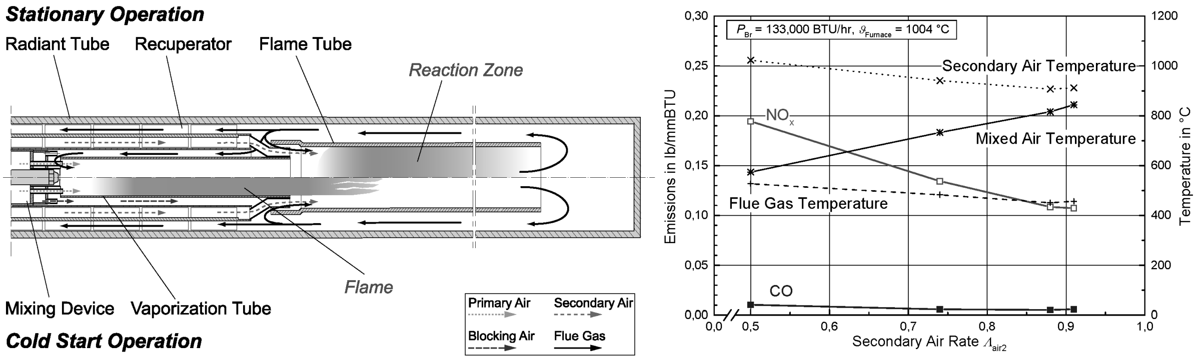

(a) Jäger et al. burner schematic [26]

(b) Jäger et al. results [26]

Figure 3.1: Jäger et al. radiant tube analysis [26]

3.2.2. EXPERIMENTS BY SCRIBANO ET AL.

Another study was conducted by Scribano et al. at Politecnico di Milano in Italy in 2006 [69]. They performed experimental investigation upon a single-ended self-recuperative radiant tube burner using natural gas as fuel. The burner was fired in non-premixed mode, exactly like the ones in this thesis. The input power was varied from 12.8-18 kW and the Equivalence Ratio (ER) was varied from 0.5 (very lean flame) to 0.95 (quasi-stoichiometric condition). The main objective of their study was to find the best operating conditions in terms of optimum ER, thermal power and lower pollutant emissions. A schematic representation of their setup is shown in Figure (3.2).

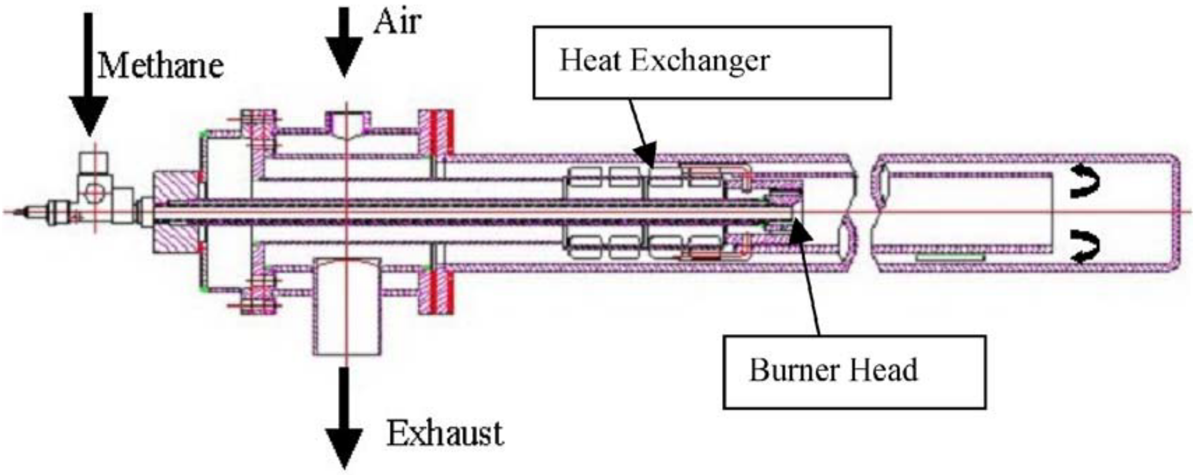

Figure 3.2: Schematic representation of Scribano et al. setup [69]

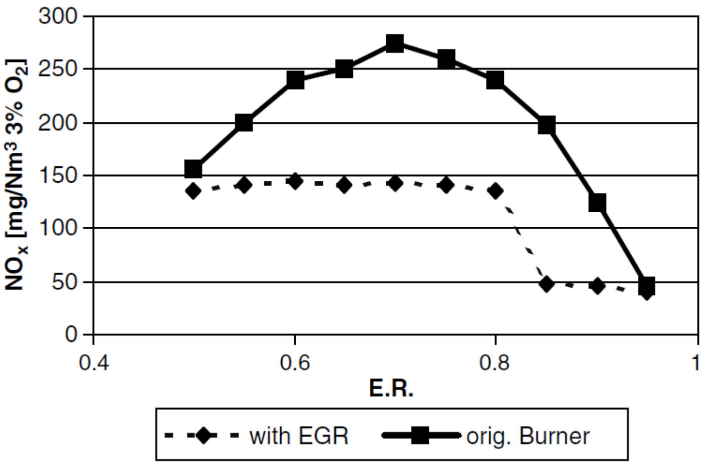

Figure 3.3: Effect of EGR on NO_x emissions [69]

This investigation was also conducted to study the effect of Exhaust Gas Re-circulation (EGR) on the formation of pollutants. The re-circulation is caused due to the jet action of the burner, injecting the fresh mixture into the flame tube at high velocity which causes the entrainment of a fraction of the burnt mixture to be pulled inside the flame tube. As explained in the first chapter, this causes a dilution of the combustion process, leading to the reduction of temperature and consequently, that of NO_x emissions as well. The variation of NO_x and CO emissions with input thermal power and ER is shown in Figure (3.4). These levels of pollutants have been measured for no EGR case. The maximum NO_x emissions were observed for ER = 0.7. As the stoichiometric mixture approaches, the NO_x emissions reduce with a sudden increase of CO emissions, due to the increase in fuel input resulting in increased flame length and incomplete fuel-air mixing. Consequently, the combustion process was modified to include EGR effect and it resulted in the reduction of NO_x emissions by approximately 50%, as shown in Figure (3.3), without compromising the thermal efficiency, CO emissions and surface temperature uniformity of the radiant tube.

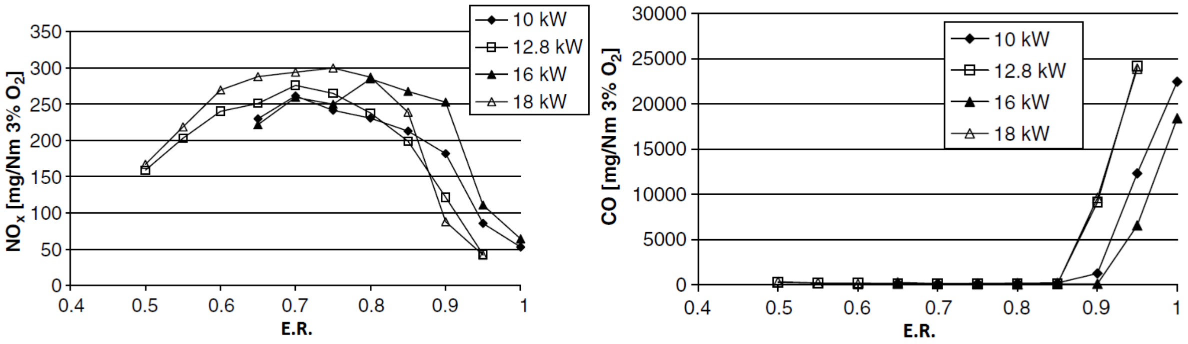

(a) Variation of NO_x emissions [69]

(b) Variation of CO emissions [69]

Figure 3.4: Variation of various pollutants [69]

3.2.3. WORK DONE BY TSIOUMANIS ET AL.

An important CFD study of the flow inside a single-ended radiant tube fired using a self-recuperative burner was conducted by Tsioumanis et al. to improve its lifetime and performance. The study was conducted in two parts: the first one dealing with the analysis of cold flow of air within the tube and the second one dealing with the analysis of combustion of natural gas and pollutant formation. The geometric model of the equipment analysed by them is shown in Figure (3.5).

The first study involves the numerical analysis of air flow inside the burner-tube assembly and its experimental validation [76]. The turbulence modelling was done using three models: standard $k-\varepsilon$ model, RNG $k-\varepsilon$ model and Reynolds stress model. However, the results obatined by the standard $k-\varepsilon$ model had the maximum agreement with the experimentally measured velocity values, the other two exhibited poor agreement. The effect of three physical features along the air inlet passage was also studied: the swirler, intended to increase the swirl of incoming air to increase the heat transfer in the recuperative section; the step ring, intended to remove some swirl and correct some of the circumferential maldistribution created by the swirler coil and the flame tube, intended to split the air flow into primary and secondary flows to stage the combustion process. The calculations were also checked for their robustness by analysing the dependence of results on the mesh size. Various meshes were chosen for this purpose, ranging from 200,000 to 600,000 nodes. However, the dependence was found to be relatively weak as the computed axial velocity exhibited a mean variation of just 4%. Hence, they reported the values obtained for 200,000 node mesh.

The second study involves the numerical analysis of combustion inside the burner-tube assembly and its experimental validation. The previous study showed that the standard $k-\varepsilon$ model had maximum agreement with the experimental data. Hence, this study used the same turbulence model and tested various combustion and radiation models using a mesh of 300,000 nodes. A finer mesh of 400,000 nodes was also tested, but mesh dependence was found to be weak. The burner was fired at the nominal thermal input of 25 kW and a pilot burner of 1 kW was used to ignite the combustion process. Air staging was used to control the peak temperatures and indirectly, the NO_x emissions. The overall equivalence ratio of the mixture was 0.9. A two step mechanism was tested using two combustion models: the Eddy Dissipation model and Turbulent Flame Closure (TFC) Model. Two radiation models were also tested: the Discrete Transfer Radiation Model (DTRM) and Monte Carlo (MC) model. Gray spectral and isotropic scattering options were selected for both the models to aid convergence and reduce computational time. The maximum agreement in terms of NO and CO prediction with experimental data was found with the results obtained using Eddy Dissipation model with temperature limiting subroutine and Discrete Transfer radiation model. The TFC model under-predicted the NO_x formation and grossly over-predicted the CO formation. The Monte Carlo radiation model did not converge properly and had oscillating residuals. After some trials, it did show some convergence, however the results were similar to that of Discrete Transfer model. Hence, the authors reported only the latter. With the models being tested and the best ones chosen, the authors then proceeded to analyse the fluid flow, combustion and heat transfer characteristics in detail [75].

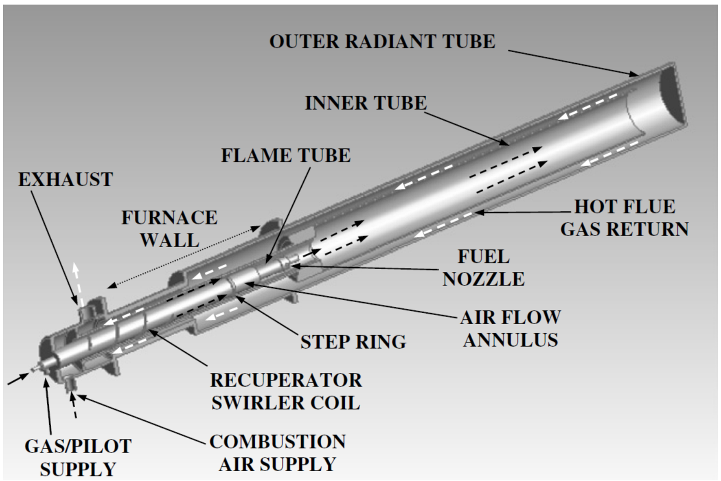

Figure 3.5: Geometric model of equipment [76]

3.2.4. WORK DONE BY AHANJ ET AL.

Another important study was conducted by Ahanj et al. and published in 2012 [1]. Their work analysed not only the fluid flow, combustion and heat transfer process inside the radiant tube but also the radiative heat transfer from the tube into an empty room. They studied the heating from a U-shaped radiant tube heater into a room of dimensions 370 x 205 x 206 cm. The whole domain was meshed into almost 1,220,000 cells with fine meshing inside and around the radiant tube and relatively coarser meshing in the rest of the domain. The standard $k-\varepsilon$ model was used for turbulence modelling with DTRM used for modelling radiation both within and outside the tube. The single step combustion mechanism was used with the Eddy Dissipation model to simulate the combustion process. The whole numerical study was validated with experimentally measured temperature values at 23 points on the radiant tube wall and at 36 points in the room. The numerical results showed good agreement with the experimental data with less than 5% deviation in all the measured values. Next, they also theoretically analysed the effect of air factor and preheat temperature on the radiant tube efficiency. It was reported that the efficiency increased with preheat temperature and decreased with air factor. However, at high preheat temperatures, the effect of air factor on efficiency was found to significantly reduce to almost negligible, with the efficiency being the same for all air factors.

3.2.5. WORK DONE BY WANG ET AL.

A major study was done by Wang et al. in 2014 [80] in which they conducted numerical investigations on a W-shaped self-recuperative radiant tube burner and validated their calculations with experimental data. The schematic diagram of their experimental setup is shown in Figure (3.6a). Their computational domain was half of the actual tube, bounded by a symmetry plane as shown in Figure (3.6b) and divided into 930,000 cells. They used the standard $k-\varepsilon$ model to model turbulence and non-premixed model using the concept of mixture fraction (z) to model combustion. They used the Discrete Ordinates model to simulate radiation with the weighted-sum-of-grey-gases-model (WSGGM) to calculate the absorption coefficients. The NO_x post-processor was used to estimate the NO production levels using Thermal and Prompt NO_x production mechanisms. Using these models, they achieved good agreement of the calculated temperature values with experimental data, although a maximum deviation of 4.1% was also observed. They next studied the effect of air-to-fuel ratio and air staging on the performance of the burner setup with respect to heat efficiency, maximum temperature, difference on the shell wall and NO emission at the outlet. They increased the air-to-fuel ratio from 5 to 15 and found the overall temperature values in the tube to initially increase, reach a maximum at 10 and then decrease gradually. The same behaviour was observed for NO emission but the maximum was achieved at ratio 12, rather than 10. This discrepancy arose due to the formation mechanism used for NO. The effect of air staging was studied by changing the ratio of primary to secondary air flow rate. At zero ratio (i.e. only secondary air) there was a strong re-circulation zone formed at the outlet which restrained the development of the fuel stream. As the ratio increased, the re-circulation zone shrank gradually allowing for the development of the fuel stream. The flame length increased, temperature decreased which lead to significant reduction in NO emissions. Although the heat efficiency also reduced, air staging proved to be important in stabilising the flame and improving the overall performance of the radiant tube burner.

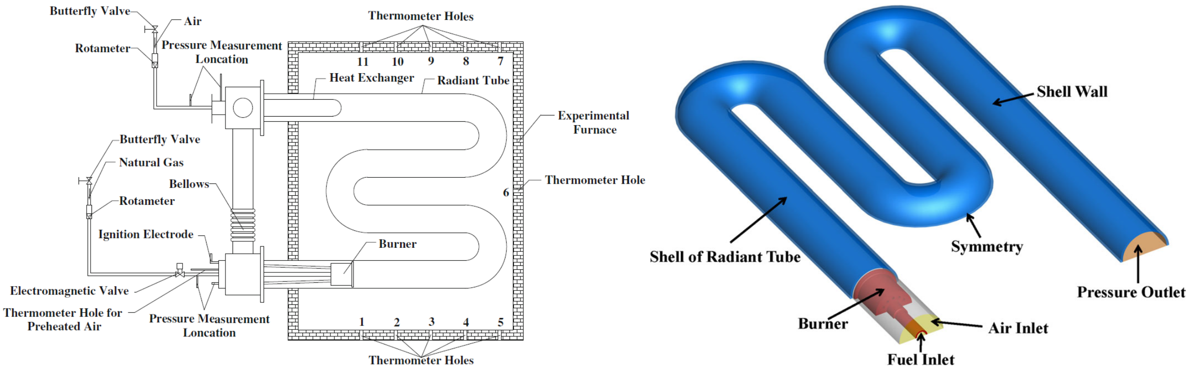

(a) Experimental setup schematic

(b) Computational domain with boundaries

Figure 3.6: Wang et al. equipment [80]

4

DESCRIPTION OF CURRENT CASE

This thesis consists of the analysis of two types of radiant tubes, fired using two different recuperative burners. Both the burners and radiant tubes have been manufactured by the German company WS Wärmeprozesstechnik GmbH. The burners used are REKUMAT® C80 and REKUMAT® C100 self recuperative burners. The respective radiant tubes are REKUMAT® C100 and REKUMAT® C150. Both the setups are single ended recirculating type. Figure (4.1) is a schematic representation of the burners.

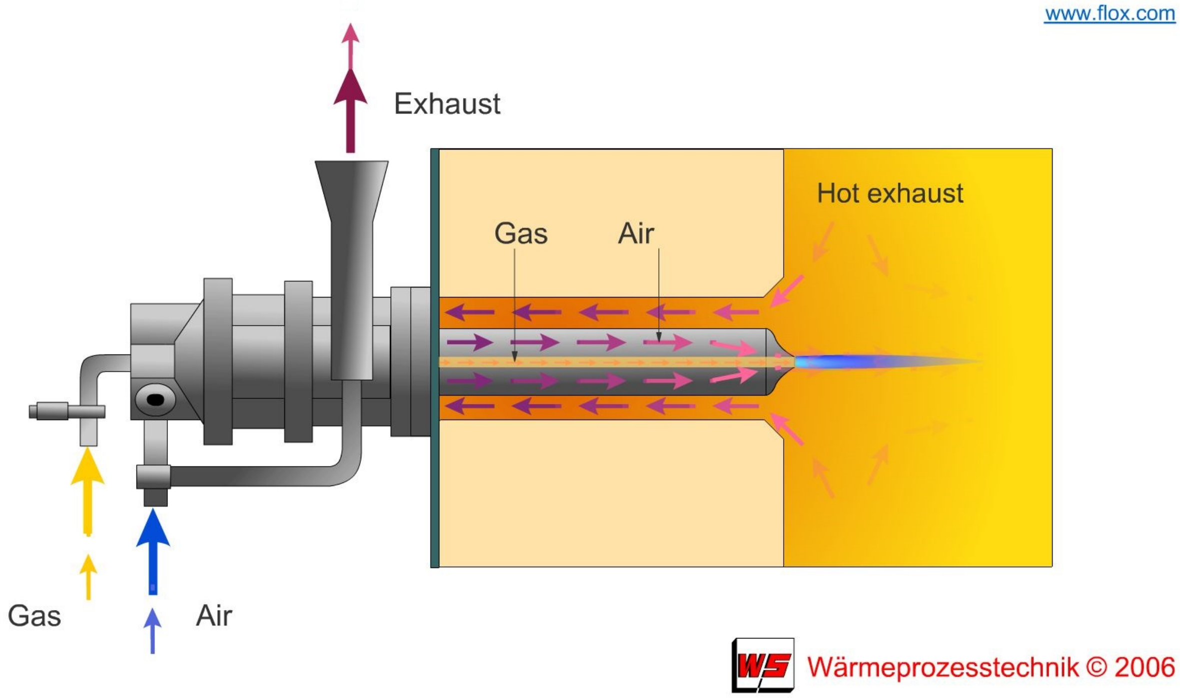

Figure 4.1: Self-recuperative burner schematic (Courtsey: WS Wärmeprozesstechnik GmbH)

Fuel and air are supplied via supply pipes at the specified pressure and temperature. They flow within the burner in concentric tubular fashion and meet towards the tip of the burner. Hence, the combustion technique applied to extract chemical energy from the fuel is non-premixed in nature. The burners are fitted with the respective tubes before installing in the fluidised bed gasifier. A ceramic flame tube is placed within the radiant tube before fitting with the burner. This flame tube forms a passage for the hot combusting fluid and the annular region between the flame tube and the radiant tube forms a passage back towards the burner. The hot exhaust gas flows over the burner and heats the incoming air for higher combustion efficiency and low emissions.

4.1. GIVEN DATA AND ASSUMPTIONS

The company has provided the supply pressure, temperature and supply pipe dimensions for air and fuel (Table (4.1)). Both are supplied at room temperature (300 K) with a maximum velocity of 10 m/s in the supply pipes. Hence, the flow rates for both can be calculated.

Table 4.1: Air and Fuel supply details

Supply pressure	
Air	109325 Pa
Fuel	106325 Pa

Air supply pipe diameter	
C80 burner	22 mm
C100 burner	32 mm

Before beginning the analysis, certain assumptions must be made for ease of calculations. Assumptions regarding the type of analysis, boundary conditions and reaction mechanism must be considered. The following assumptions have been made for this thesis:

- The actual composition of DNG contains hydrocarbons from methane upto hexane [21], as tabulated in Tables (4.2) and (4.3). However, the simulation fuel is assumed to contain just methane, carbon-dioxide and nitrogen. The details of simulation fuel composition calculation are given in **Appendix A**.

Table 4.2: Dutch natural gas composition (mass percent)

Component	**CH_4**	**C_2H_6**	**C_3H_8**	**C_4H_{10}**	**C_5H_{12}**	**C_6H_{14}**	**O_2**	**N_2**	**CO_2**
Actual	69.97	4.63	0.90	0.47	0.16	0.23	0.02	21.52	2.10
Simulation	76.00	0.00	0.00	0.00	0.00	0.00	0.00	21.87	2.13

Table 4.3: Dutch natural gas composition (mole percent)

Component	**CH_4**	**C_2H_6**	**C_3H_8**	**C_4H_{10}**	**C_5H_{12}**	**C_6H_{14}**	**O_2**	**N_2**	**CO_2**
Actual	81.29	2.87	0.38	0.15	0.04	0.05	0.01	14.32	0.89
Simulation	85.13	0.00	0.00	0.00	0.00	0.00	0.00	14.00	0.87

- The reaction proceeds in a single step with the fuel and air reacting to form products, without the formation of any intermediates. Although more complex and accurate mechanisms are available in literature, they would have increased the computation time considerably and were consequently not chosen. Hence, the following simple reaction takes place:

$$CH_4(g) + 2O_2(g) \rightarrow CO_2(g) + 2H_2O(g) \tag{4.1}$$

- Since air is supplied at the maximum supply velocity (10 m/s), its mass flow rate is fixed. The relative air/fuel ratio is maintained by adjusting the fuel supply ratio. This is in contrast to regular burners used in the industry where the fuel supply is kept constant and air supply is varied.

- The radiant tube transfers energy to the fluidised bed maintained at 850°C. Since the mechanism of that transfer and its details were not known at the time of these CFD calculations, the outer surface of the radiant tube is assumed at 850°C.

4.2. DESCRIPTION OF FLOW INSIDE PHYSICAL TUBES

The flow must be studied before the actual simulation so that the calculated results may be as accurate as possible. Two aspects of the flow have been analysed to gain a rough idea of its nature: the extent of the reaction and turbulence level. A rough knowledge of these aspects will help us choose an appropriate turbulence model and estimate the mesh size required for accurate results.

We first estimate the extent to which the combustion reaction proceeds inside the radiant tubes. This is done by calculating the equilibrium constant for the assumed reaction. Since the reaction is homogeneous and completely in gas phase, the equilibrium constant is calculated in terms of partial pressures (and also mole fractions) as follows:

$$K_{eq} = \frac{p_{CO_2}(p_{H_2O})^2}{p_{CH_4}(p_{O_2})^2} = \frac{[X_{CO_2}][X_{H_2O}]^2}{[X_{CH_4}][X_{O_2}]^2} \tag{4.2}$$

Since the partial pressures (or mole fractions) of individual species are not known, the equilibrium constant can't be directly calculated. However, the variation of the constant can be studied with temperature using the following expression [61]:

$$K_{eq} = \left(\frac{p_a}{RT}\right)^{\Sigma_{k=1}^{N} \nu_k} \exp\left(\frac{\Delta S_j^0}{R} - \frac{\Delta H_j^0}{RT}\right) \tag{4.3}$$

The values of K_{eq} have been calculated for reaction (4.1) for a temperature range of 300 - 2500 K as the adiabatic flame temperature of methane does not exceed 2500 K. The high values of K_{eq} shown in figure (4.2) suggest that the reaction goes to almost completion within this temperature range. Even at 2500 K, K_{eq} does not go below 10^5. Hence, we can assume that complete combustion of fuel takes place inside the radiant tubes.

To assess turbulence level, we calculate the Reynolds numbers for the reacted mixture in both the radiant tubes for the same temperature range. Reynolds number has been calculated at three regions of the burner-tube assembly: near the burner tip (considering the inner diameter of the radiant tube), inside the flame tube (considering the inner diameter of the flame tube) and in the annular region between the radiant and flame tubes (as shown in Figure (4.4)). The plots are shown in Figure (4.3). From these plots, it can be seen that the flow is transitioning towards turbulence. The maximum turbulence is encountered within the flame tube. Hence, the meshing of this region would be most important to capture all the effects of fluctuations.

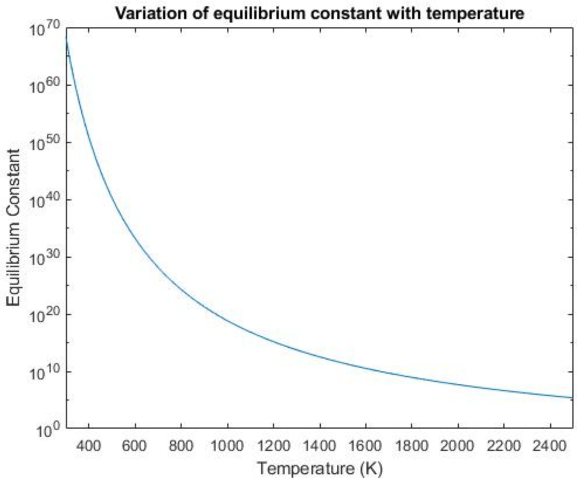

Figure 4.2: Equilibrium constant with temperature

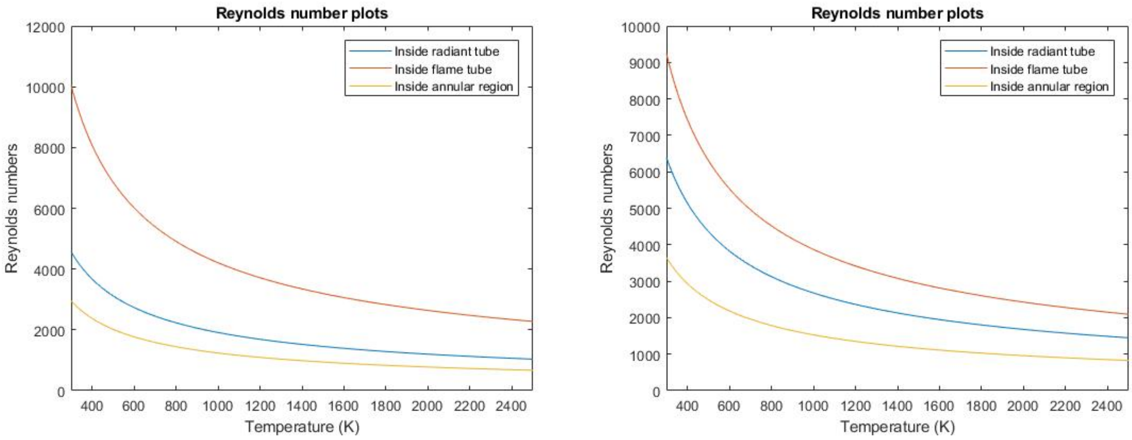

(a) C80-C100 Reynolds number

(b) C100-C150 Reynolds number

Figure 4.3: Reynolds number for both burner-tube assembly

4.3. GEOMETRIC MODELLING

The radiant tubes analysed in this thesis are cylindrical in shape, fitted over the burners. Since the tubes are cylindrical in shape, the flow within the tubes is assumed to be symmetric around the axis. Hence, only one half of the diametrical cross-section of the flow is modelled. The geometric model is hence, a two-dimensional surface bounded by appropriate boundaries. The model was made in ANSYS® DesignModeler. When the burner-tube assembly is installed in the gasifier, the length from the supply inlets until the tip of the burner remains completely insulated. There is no heat released to the outer environment as the fuel and air flow inside the burner and the exhaust gases flow over the burner. Hence, only the region from the tip of the burner to the end of the radiant tube, along with the flame tube is modelled. The tube assembly also has a few protrusions on the inner ceramic flame tube. These protrusions provide support to the flame tube inside the radiant tube and can also be used to fix thermocouples for temperature measurements. However these protrusions do not have much effect on the flow and can safely be ignored in CFD calculations. Hence, the geometric model was designed without these protrusions and only show two concentric tubes as outer radiant tube and inner flame tube.

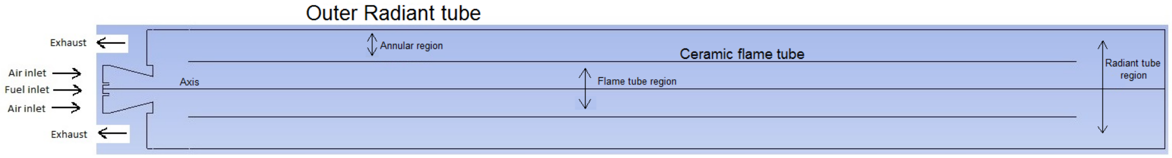

Figure 4.4: Geometric domain for CFD calculations

Figure (4.4) shows the nozzle of the burner, approximated as the frustum of a cone, attached to the outer radiant tube, containing an inner concentric flame tube. Air and fuel enter via their respective inlets and come in contact within the nozzle to begin the reaction. The nozzle concentrates the flow near the axis and directs it into the flame tube, so that the flow may not escape into the exhaust without combusting. As the combusting flow travels along the flame tube, it releases energy which is transferred to the tube walls via convection and radiation. The wall conducts energy and transfers it to the outer concentric flow via convection. Radiative exchange of energy also happens between the flame tube and outer tube. However, the combusting flow is radiatively participating and changes the radiative intensity via absorption and emission. Finally, the flow exits the computational domain via exhaust and heats the incoming air while flowing over the burner.

4.4. MESHING

The mesh was made in the default software provided by ANSYS® Workbench. The mesh mainly consists of quadrilateral elements except for the nozzle region. The element size was estimated using the y^+ values near the outer (radiant tube) and inner (flame tube) wall, calculated as follows:

$$y^+ = \frac{y u_\tau}{\nu} \quad \text{where} \quad u_\tau = \sqrt{\frac{\tau_{wall}}{\rho}} \quad \text{where} \quad \tau_{wall} = \frac{1}{2} C_f \rho (u_\infty)^2 \tag{4.4}$$

The wall viscous stress (τ_{wall}) can be calculated using bulk velocity (u_∞) and Fanning friction factor (C_f) defined as follows [58] [4]:

$$C_f = \begin{cases} 16/Re_D & \text{for } Re_D \le 2300 \\ 0.25(0.79\, ln(Re_D) - 1.64)^{-2} & \text{for } 2300 \le Re_D \le 5 * 10^6 \end{cases} \tag{4.5}$$

y^+ values near unity are ideal for proper analysis of the near wall region as the velocity and temperature gradients are quite sharp in this region. Hence, in our case as well, we have taken $y^+ = 1$ and estimated the mesh size for accurate simulations. As mentioned before, the reacted mixture is used for calculation of flow properties like density and viscosity. Figures (4.5) and (4.6) show the variation of friction factor and cell height (from the wall) for the assumed temperature range for all the three regions of the radiant tube.

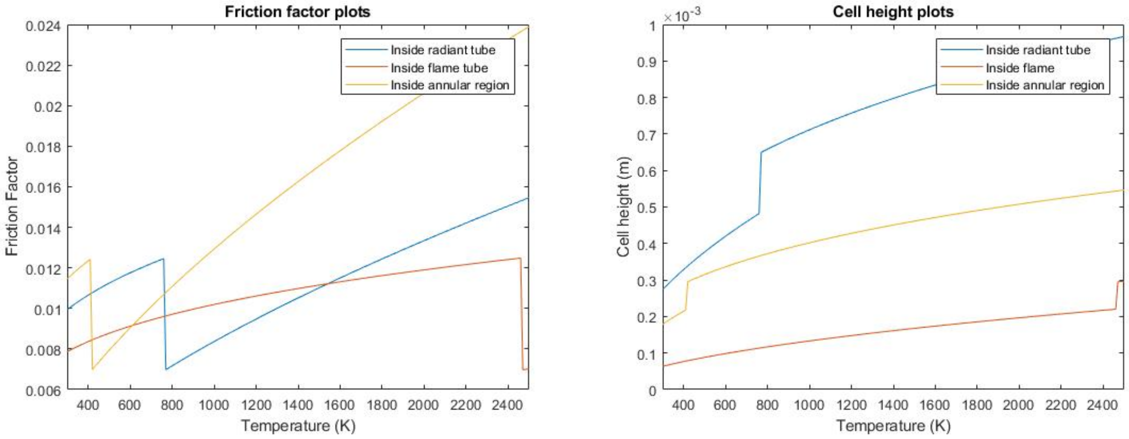

(a) Variation of friction factor

(b) Variation of cell height

Figure 4.5: Mesh size calculation for C80 radiant tube

The kinks in the plots can be explained by the sudden change of friction factor around Reynolds number 2300 (as can be inferred from Eqn. (4.5)). From the plots, it can be seen that mesh size of approximately 0.1 mm would be required for accurate analysis of the radiant tubes. However, the Academic version of ANSYS® Fluent allows a maximum of 512000 cells for CFD simulations. The number of cells in the mesh with 0.1 mm cell size exceeds the maximum limit imposed by the software. Hence, a larger cell size was chosen for the calculations. Table (4.4) provides the details of the meshes for both the burner-tube assemblies. Please note that the values given for cell quality, orthogonal quality and skewness are the average values for the whole mesh. The resulting mesh has proven to be quite fine and has provided accurate results for the simulations.

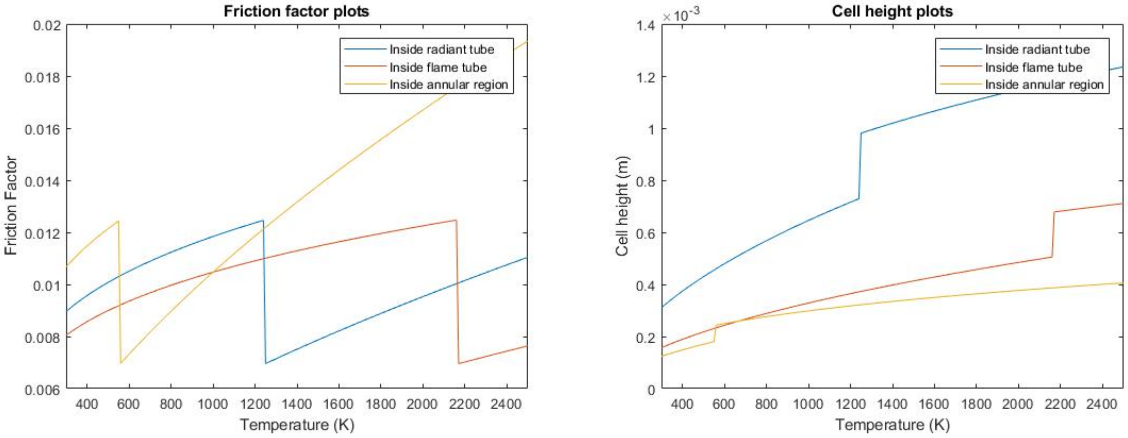

(a) Variation of friction factor

(b) Variation of cell height

Figure 4.6: Mesh size calculation for C100 radiant tube

Table 4.4: Mesh Details

Burner	Element size (mm)	No. of cells	No. of nodes	Cell quality	Orthogonal Quality	Skewness
C80	0.5	152403	154191	0.99867	0.99994	9.8710e-4
C100	0.75	153507	155297	0.99800	0.99991	1.7979e-3

4.5. TURBULENCE AND COMBUSTION MODELS

The calculation of Reynolds number in section (4.2) proves helpful in selecting an appropriate turbulence model for current calculations. From the calculations, it can be assumed that the flow is transitioning towards turbulence. As mentioned before, the air flow rate has been kept constant and the air/fuel ratio has been varied by varying the fuel flow rate. Since the air flow rate is much larger than fuel flow rate, the overall mass flow rate will not significantly change by changing the air/fuel ratio. Hence, the Reynolds number for all the cases would remain almost the same. Hence, a Low-Reynolds model would be most appropriate for analysing such a flow. However, for the present thesis, the standard $k-\varepsilon$ model with standard wall functions has been used for both the tubes. This model is appropriate for fully turbulent flows (i.e. Reynolds number more than 10000 for pipe flows). The standard wall functions give accurate results when y^+ values $30 < y^+ < 500$ [79]. However, it it has been found that although the estimated y^+ values lie near unity, the CFD calculations actually yield y^+ values near 10. This discrepancy can be attributed to the fact that we have assumed completed reaction at stoichiometric level throughout the tube to estimate the required cell height, whereas actual simulations may have unreacted species at different regions of the computational domain at non-stoichiometric overall levels. Since it is the industrial standard to use the standard wall functions, they have been used in-spite of y^+ being in the wrong value range. The law-of-the-wall for mean velocity yields [40]:

$$U^* = \frac{1}{\kappa}\ln(Ey^*) \tag{4.6}$$

where the dimensionless velocity (U^*) and the dimensionless distance from the wall (y^*) are calculated as follows:

$$U^* = \frac{\rho U_P C_\mu^{0.25} k_P^{0.5}}{\tau_{wall}} \quad \text{and} \quad y^* = \frac{\rho C_\mu^{0.25} k_P^{0.5} y_P}{\mu} \tag{4.7}$$

Here, the various symbols have the following meanings:

- κ = von Kármán constant = 0.4187
- E = empirical constant = 9.793
- μ = dynamic viscosity of fluid
- $C_\mu = 0.09$

and U_P, k_P and y_P represent the mean velocity, turbulent kinetic energy and distance from wall of the wall-adjacent cell centroid.

The calculation of equilibrium constant (K_{eq}) in section (4.2) shows that the reaction proceeds almost to completion. Hence, the turbulence-chemistry interaction becomes quite easy to model. For the present thesis, reaction rate approach has been taken to calculate the density, species mass fraction and temperature values. The species net production rates have been calculated using the Eddy-Dissipation model, assuming that the flow and diffusion rates are smaller than the chemical reaction rates. Hence, the reaction in the radiant tubes is turbulence-controlled. As mentioned before, the species production rate is calculated as follows:

$$\bar{\dot{\omega}}_{k,r} = \nu'_{k,r} M_{w,k} A \rho \frac{\varepsilon}{k} \min_{\mathscr{R}} \left(\frac{Y_{\mathscr{R}}}{\nu'_{\mathscr{R},r} M_{w,\mathscr{R}}} \right) \tag{4.8}$$

$$\bar{\dot{\omega}}_{k,r} = \nu'_{k,r} M_{w,k} A B \rho \frac{\varepsilon}{k} \left(\frac{\sum_P Y_P}{\sum_{j=1}^{N} \nu''_{j,r} M_{w,j}} \right) \tag{4.9}$$

where the various symbols have meanings as explained in a previous chapter.

4.6. MATERIAL FOR THE TUBES

The material for the radiant tube and flame tube for both the burner-tube assemblies has been provided in the data sheets given by the company. The outer radiant tube for both the setups is made of austenitic stainless steel 1.4852 made via casting. The composition of this alloys is given below [17]:

Table 4.5: Composition of stainless steel 1.4852 (mass percent)

Iron	**Nickel**	**Chromium**	**Silicon**	**Niobium**	**Manganese**	**Carbon**	**Molybdenum**	**Phosphorus**	**Sulphur**
29.6-40.9	33.0-36.0	24.0-27.0	1.0-2.5	0.8-1.8	0.0-2.0	0.3-0.5	0.0-0.5	0.0-0.04	0.0-0.03

The inner flame tube is made of Siliconized Silicon Carbide (SiSiC), also called Reaction-bonded Silicon Carbide. This material is very durable because it provides excellent high temperature strength, creep resistance and resistance to oxidation as compared to metallic alloys. It can withstand temperatures upto 2250°F and can allow heat fluxes as high as 110 Btu/hr [30]. The properties of these two materials are provided in Table (4.6).

Table 4.6: Material Properties [17] [65] [53]

	1.4852 steel	**SiSiC**
Density (kg/m^3)	7900	3000
Specific heat capacity (J/kgK)	480	1180
Thermal Conductivity (W/mK)	13	140
Radiative emittance	0.4094	0.895

A few points need to be mentioned about the radiative emittance mentioned above. The values have been taken from [53] which provides values for total normal emittance of various substances. However, the textbook does not provide values for "Siliconized silicon carbide" or "Reaction-bonded silicon carbide" per se, rather for "Silicon carbide" only. There is no single value of emittance given, but for a temperature range. The emittance at 150°C is given to be 0.83 and that at 650°C is 0.96.

The temperature average value of 0.895 has been used for CFD calculations.
The radiative emittance of stainless steel 1.4852 is also not available in that textbook. Rather, the values for cleaned steel have been used. The value ranges at temperatures 100°C, 500°C and 1000°C have been provided in Table (4.7):

Table 4.7: Data used for stainless steel 1.4852

Temperature	**100°C**	**500°C**	**1000°C**
Given range	0.21-0.38	0.25-0.42	0.50-0.77
Used value	0.295	0.335	0.635

The average value of the range for each temperature has been calculated and then the temperature average of these values has been calculated and used for CFD calculations. Thus, the radiative emittance for both the materials may have some factual inaccuracies because values interpolated from different materials has been used.

5

RESULTS AND DISCUSSION

This chapter deals with the elaboration of the calculations done within this thesis and presents the results obtained, along with the appropriate discussion. First, the scheme of calculations will be explained, followed by the results and discussion.

5.1. SCHEME OF CALCULATIONS

The main objective of this thesis is to study the heat transfer from both the burner-tube assemblies and to understand its variation with air preheat temperature and air factor. Air factor may be defined as the ratio of mass of actual air to stoichiometric quantity required per unit mass of fuel. As mentioned in the previous chapter, the composition of the fuel used in simulations contains only methane (CH_4), carbon-dioxide (CO_2) and nitrogen (N_2) in a certain ratio (Table (5.1)). The molecular weight of this fuel may be calculated as follows [30]:

Table 5.1: Composition of simulation fuel

Component	**CH_4**	**CO_2**	**N_2**
Mass percent	76.00	2.13	21.87
Mole percent	85.13	0.87	14.00

$$\begin{aligned} \mathrm{MW}_{fuel} &= 0.8513\,\mathrm{MW}_{CH_4} + 0.0087\,\mathrm{MW}_{CO_2} + 0.14\,\mathrm{MW}_{N_2} \\ &= (0.8513 * 16.04) + (0.0087 * 44.01) + (0.14 * 28.014) \\ &= 17.92\ \mathrm{g} \end{aligned}$$

The supply air is assumed to contain only oxygen (23% by mass) and nitrogen (77% by mass). Hence, according to equation (4.1), 17.92 g of fuel would require 233.73 g of air. Air factor is varied from 1.0 to 1.5 in steps of 0.1. Hence, the mass of air required per unit of fuel is tabulated below:

Table 5.2: Air-fuel ratio

Air Factor	**1.0**	**1.1**	**1.2**	**1.3**	**1.4**	**1.5**
Fuel mass (g)	17.92					
Air Mass (g)	233.73	257.11	280.48	303.85	327.23	350.60

As mentioned in the previous chapter, the mass flow rate of air is fixed and that of fuel is varied to achieve the required air factor. Since, the supply pressure, temperature, maximum supply velocity and dimensions of supply pipe of air have been given, the maximum mass flow rate of air can be calculated. Then, using the above ratios, the required fuel flow rate can also be calculated. The density of air at 109325 Pa and 300 K is calculated to be 1.2680 $\mathrm{kg/m^3}$ (using ideal gas assumption). The mass flow rate of air in both the burner-tube assemblies is calculated on the next page:

$$\dot{m}_{C80} = \rho_{air} \frac{\pi D^2_{supply,C80}}{4} v_{max} = 1.268 * \frac{\pi * 0.022^2}{4} * 10 = 0.0048\,\text{kg/s} \tag{5.1}$$

$$\dot{m}_{C100} = \rho_{air} \frac{\pi D^2_{supply,C100}}{4} v_{max} = 1.268 * \frac{\pi * 0.032^2}{4} * 10 = 0.0102\,\text{kg/s} \tag{5.2}$$

The mass flow rates for fuel for all air factors and both the burner-tube assemblies is tabulated below:

Table 5.3: Fuel flow rates (in kg/s)

Air factor	**1.0**	**1.1**	**1.2**	**1.3**	**1.4**	**1.5**
C80	3.6961e-4	3.3601e-4	3.0801e-4	2.8468e-4	2.6436e-4	2.4672e-4
C100	7.8298e-4	7.1180e-4	6.5248e-4	6.0229e-4	5.5927e-4	5.2199e-4

Since the effect of air preheat is also to be studied, the preheat temperature of air incoming into the computational domain has been varied for both the burner-tube assemblies. According to the data sheets of the burners, the preheat temperature for C80 burner has been varied from 300°C to 700°C and that of C100 burner has been varied from 300°C to 800°C in steps of 100°C. Hence, the bulk of the analysis consists of 30 calculations for C80 burner and 36 calculations for C100 burner. The results of all these calculations have been reported and discussed next.

5.2. MAIN CALCULATION RESULTS

This section presents the results for both burner-tube assemblies. The variation of the following quantities with air factor and air preheat temperature have been presented:

- Maximum calculated temperature
- Maximum calculated velocity
- Total Heat output (from outer wall)
- Radiative heat output
- Radiative heat fraction
- Radiant tube efficiency
- Fuel consumption and wastage

A complete understanding of the variation of maximum calculated temperature requires the analysis of the maximum theoretical limit on combustion products, i.e. adiabatic flame temperature, and its variation with air factor and preheat temperature.

5.2.1. VARIATION OF ADIABATIC FLAME TEMPERATURE

The theoretical limit on the maximum achievable temperature during a combustion reaction is calculated using adiabatic conditions. It can be calculated under constant pressure or constant volume conditions. The enthalpy (or internal energy, in case of constant volume assumption) of the reactants is equated to that of the products. Since, the thermodynamic state of reactants is known, the thermodynamic state of products can be calculated. The quantity thus obtained is called the Adiabatic Flame Temperature. This temperature may vary with the relative amounts of reactants and their respective temperatures. As mentioned in equation (4.1), the species participating in the reaction are CH_4, O_2, CO_2 and H_2O. However, the computational domain also has CO_2 and N_2 incoming via the fuel stream and N_2 via the oxidiser stream. These extra species will also affect the adiabatic flame temperature and the actual calculated temperature. Hence, the first step is to analyse the variation of adiabatic flame temperature with air factor and preheat temperature. In the present case, constant pressure condition has been assumed and required quantities calculated. As can be seen from figure (5.1), the adiabatic flame temperature increases with increasing preheat temperature. This is because the enthalpy of the reactants increases with increasing preheat temperatures. Hence, the products have to be at successively higher temperatures to match the enthalpy of the reactants. It also must be noted that the adiabatic flame temperature decreases with increasing air factor. As the air factor increases, the relative amount of air increases and combustion becomes progressively lean. Hence, the fuel becomes the limiting reagent and the product mixture consists of oxidiser components as well. These extra oxidiser components must also be heated to the product temperature. Hence, the energy that is used for heating the combustion product species must now be divided to heat this extra oxidiser as well. Therefore, the overall temperature of the product mixture decreases, resulting in the decrease of adiabatic flame temperature.

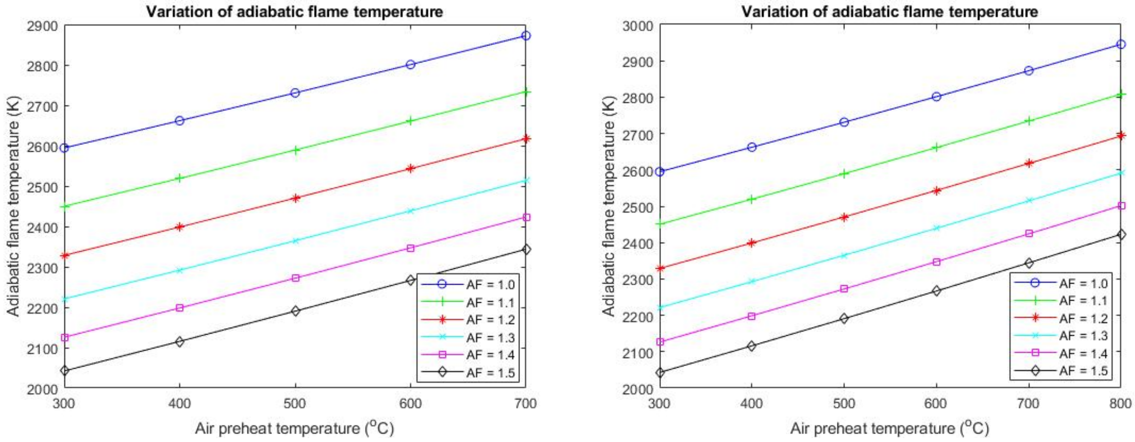

(a) C80-C100 burner-tube assembly

(b) C100-C150 burner-tube assembly

Figure 5.1: Variation of Adiabatic flame temperature

5.2.2. VARIATION OF MAXIMUM CALCULATED TEMPERATURE

The maximum calculated temperature provides an estimate of the extent to which the reaction proceeds in the computational domain. The behaviour of maximum calculated temperature is expected similar to adiabatic flame temperature, as both quantities depend on the extent of progress of reaction. As can be seen from figure (5.2), the maximum calculated temperature does indeed increase with the air preheat temperature. The reason for this behaviour is the same as that explained for adiabatic flame temperature. However, the maximum calculated temperature is found to increase with increasing air factor, in stark contrast to adiabatic flame temperature. The calculation of adiabatic flame temperature involves an important assumption that all reactants react completely till the limiting reagent is consumed, causing no wastage of air or fuel. However, in real situations, the reactants will react only if their molecules collide in proper orientation. Thus there may be many fuel molecules which may never react and go out through the exhaust stream. As the air factor increases, the relative number of oxidiser molecules increases and so does the probability that a given fuel molecule will react with the required number of oxidiser molecules. Hence, the maximum calculated temperature increases with increasing air factor.

The behaviour of maximum calculated temperature can also be understood in terms of numerical modelling. For any RANS model, as the turbulence level increases, the mean values of flow properties would decrease, to accommodate the effects of increased fluctuations. In our case, the amount of fuel inlet decreases for the same air inlet to achieve leaner combustion mixtures. Thus, the total inlet rate decreases for the same size of the computational domain, leading to decrease in turbulence with increasing air factor. Hence, the maximum calculated temperature increases with increasing air factor. The variation of turbulence has been explained in **Appendix B**.

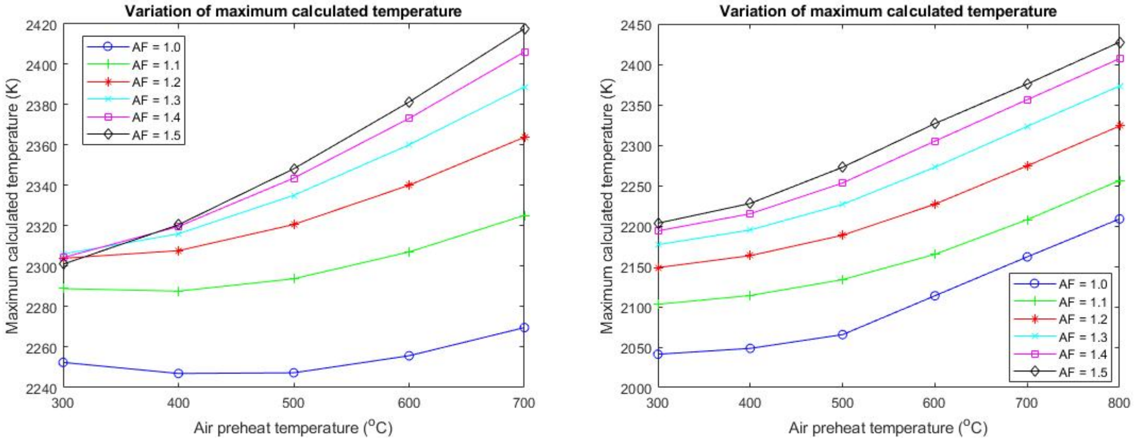

(a) C80-C100 burner-tube assembly (b) C100-C150 burner-tube assembly

Figure 5.2: Variation of maximum calculated temperature

However, the C80-C100 burner-tube assembly exhibits an anomaly for air factors 1.4 and 1.5 at 300°C air preheat and also for stoichiometric mixture at 400 and 500°C air preheat. This anomaly can be attributed to numerical errors that may have crept up during the calculation process.

TEMPERATURE CONTOURS

This section presents temperature contours at highest air preheat temperature for C100-C150 burner-tube assembly for three air factors, 1.0, 1.2 and 1.5. The changes with air factor are distinctly visible.

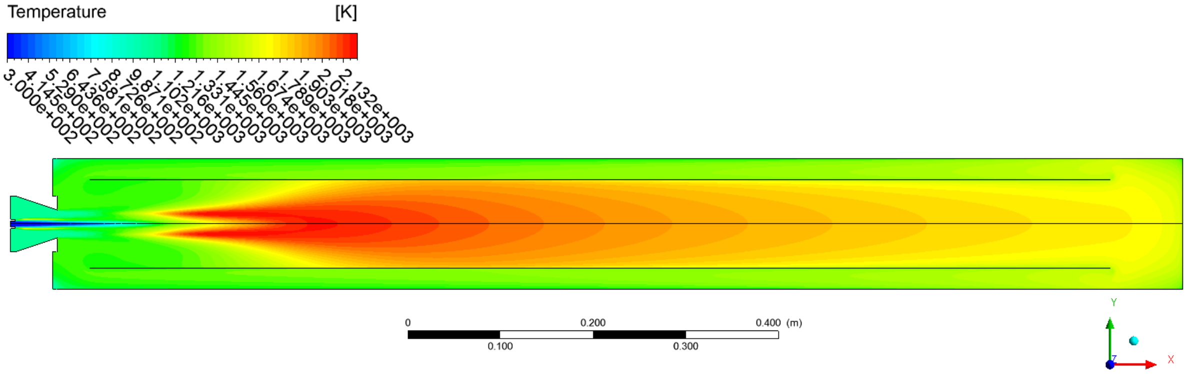

Figure 5.3: Temperature contours at air factor 1.0

As can be seen from the contours, the hot gaseous region is the largest for stoichiometric mixture and decreases as the mixture becomes lean. However, the maximum temperature increases with air factor. This means that the combustion is concentrated to a small region for lean mixture and the extent of reaction is more than for stoichiometric mixture. This can be explained because the fuel input has been decreased for lean mixture. These contours help us appreciate the difference in the maximum calculated values for different air factors. The effect of air preheat temperatures on maximum calculated temperatures is self-explanatory, it does not require the aid of temperature contours. These contours also help us appreciate the power and usefulness of CFD procedures.

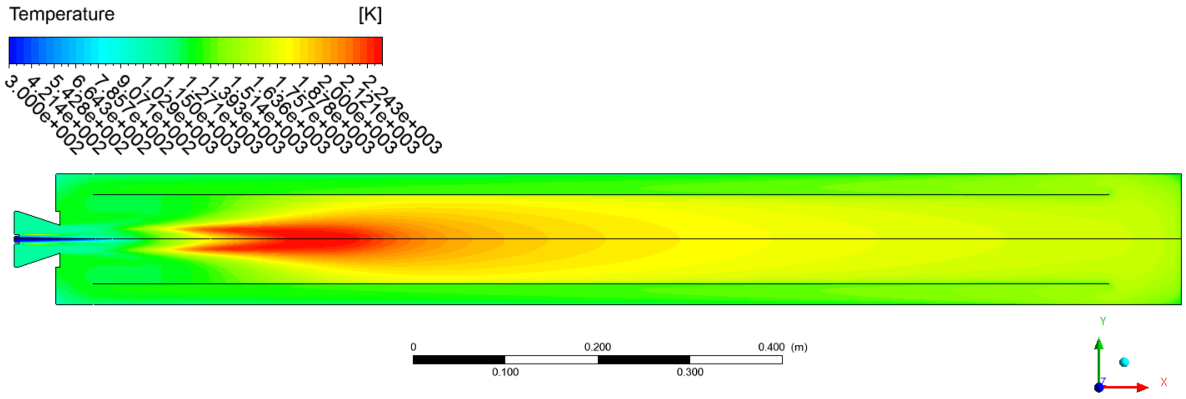

Figure 5.4: Temperature contours at air factor 1.2

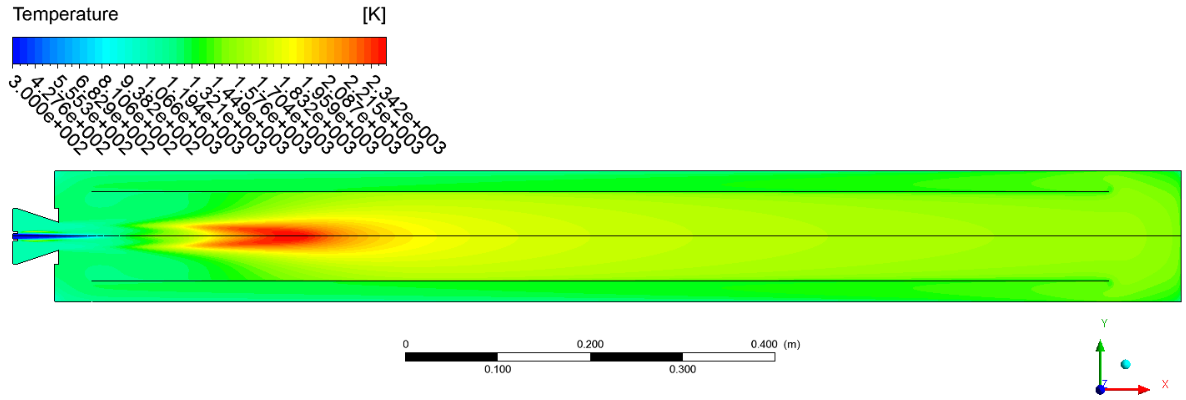

Figure 5.5: Temperature contours at air factor 1.5

5.2.3. VARIATION OF MAXIMUM CALCULATED VELOCITY

The variation in maximum calculated velocity will help in understanding the variation of turbulence in the tubes and indirectly, that of maximum calculated temperature. As the total mass flow decreases with increasing air factor, the maximum calculated velocity is expected to decrease. The variation is shown in Figure (5.6). The variation for C100-C150 setup is more prominent than that for C80-C100 setup.

The maximum calculated velocity indeed decreases with increasing air factor. It also increases with increasing air preheat temperature. This can be attributed to decreasing fluid density with increasing temperature, leading to increase in velocity to accommodate the total mass flow.

5.2.4. VARIATION OF TOTAL HEAT OUTPUT

The main purpose of using radiant tube heaters is to heat the fluidised bed in the gasifier. Hence, the analysis of the variation of the total heat output with air factor and preheat is of utmost importance. Figure (5.7) shows the variation of heat output with both the variables. The heat output is increasing with the air preheat temperature because successively greater energy is input into the radiant tube in the form of sensible enthalpy of air. However, the heat output is found to decrease with increasing air factor. This can be attributed to two factors:

- Hot unused air in exhaust stream: As the air factor increases, the amount of air per unit of fuel increases. This results in an increase of hot unused air that goes out of the exhaust.
- Reduction of reaction heat source: It has been found that the energy released from the combustion reaction reduces with increase in air factor. This is shown in Figure (5.8).

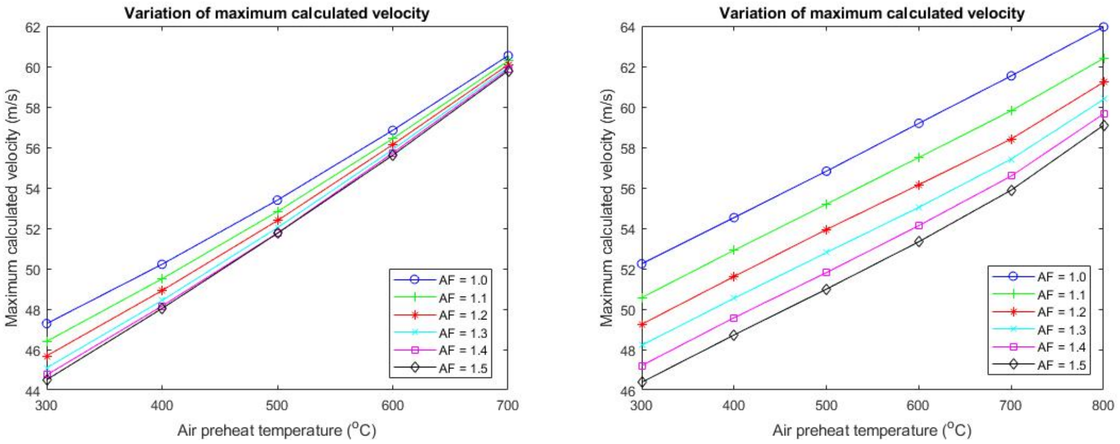

(a) C80-C100 burner-tube assembly (b) C100-C150 burner-tube assembly

Figure 5.6: Variation of maximum calculated temperature

The reaction heat source decreases with increasing air factor because the fuel inlet progressively decreases for constant air inlet (Table (5.3)). The increase in heat output from the radiant tube for constant reaction heat source (with respect to air preheat temperature) can again be attributed to two factors:

- Increase in convective heat transfer: As the temperature increases, the density of the combusting fluid decreases. Hence, the velocity of the fluid has to increase to maintain the mass flow. Since convection is directly proportional to the velocity of the fluid, it has an increasing contribution in the heat output.
- Increase in radiative heat transfer: As the temperature increases, heat transfer by radiation becomes increasingly prominent. The inner surface of the radiant tube receives energy in the form of radiation emitted by the ceramic wall and the hot combusting fluid itself. Hence, the total heat output from the radiant tube increases.

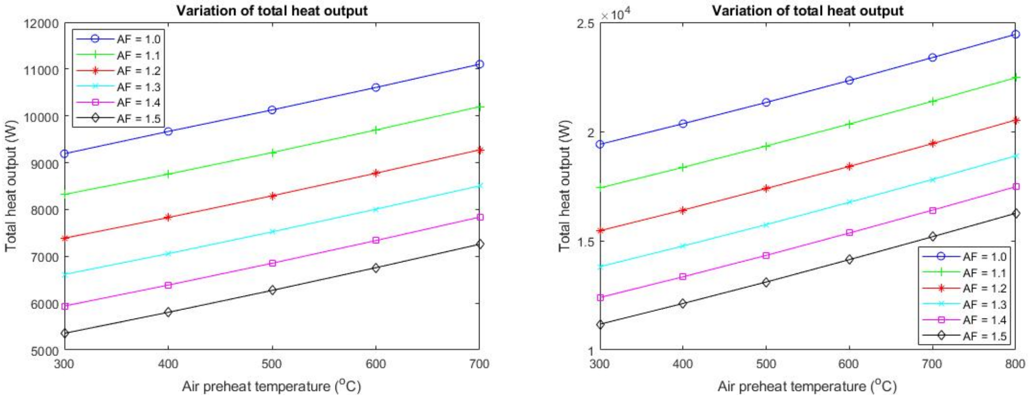

(a) C80-C100 burner-tube assembly (b) C100-C150 burner-tube assembly

Figure 5.7: Variation of total heat output

5.2.5. VARIATION OF RADIATIVE HEAT OUTPUT

A major section of heat transfer takes place via radiation in combustion systems. As the temperature increases, radiative transfer becomes increasingly more prominent as it depends on the fourth

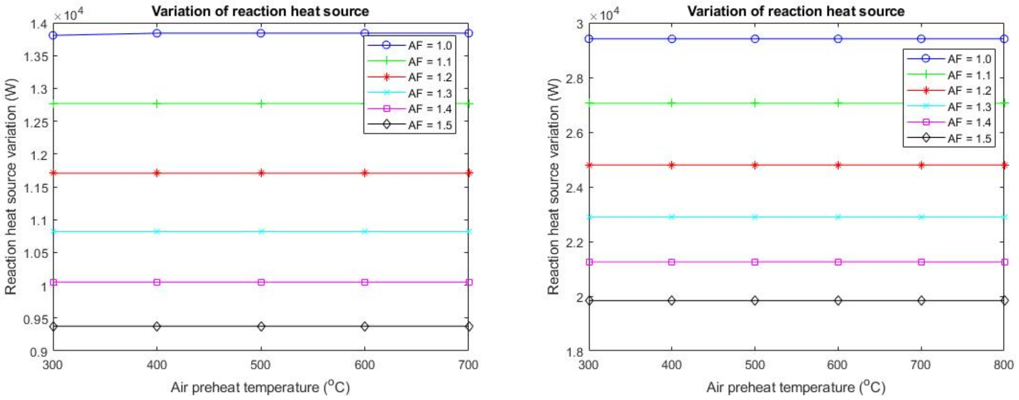

(a) C80-C100 burner-tube assembly

(b) C100-C150 burner-tube assembly

Figure 5.8: Variation of reaction heat source

power of temperature. Figure (5.7) shows the variation of total heat output from the radiant tube. This includes convective as well as radiative heat transfer to the inner surface of the radiant tube. Figures (5.9) and (5.10) show the variation of radiative heat transfer with air factor and preheat temperature. This energy is being transferred to the inner surface of the radiant tube via radiation emitted by the combusting fluid as well as by the hot ceramic wall. As expected, the amount of energy transferred does increase with air preheat temperature. However, the relative proportion of radiative transfer decreases with air preheat temperature. As the temperature increases, the velocity of the combusting fluid also increases due to decrease in density. This leaves less time for the fluid to emit radiation. However, at higher temperatures the fluid does emit more radiation.
However, radiative heat transfer and its relative proportion both decrease with increasing air factor. As mentioned previously, air is radiatively non-participating at such high temperatures. The only contribution to radiation is by CO_2 and H_2O molecules. As the air factor increases, the relative percentage of air increases. In this thesis, that has been achieved by lowering the amount of fuel inlet. Hence, for successively higher air factors, less CO_2 and H_2O is produced. Hence, the contribution to radiation decreases with increasing air factor.

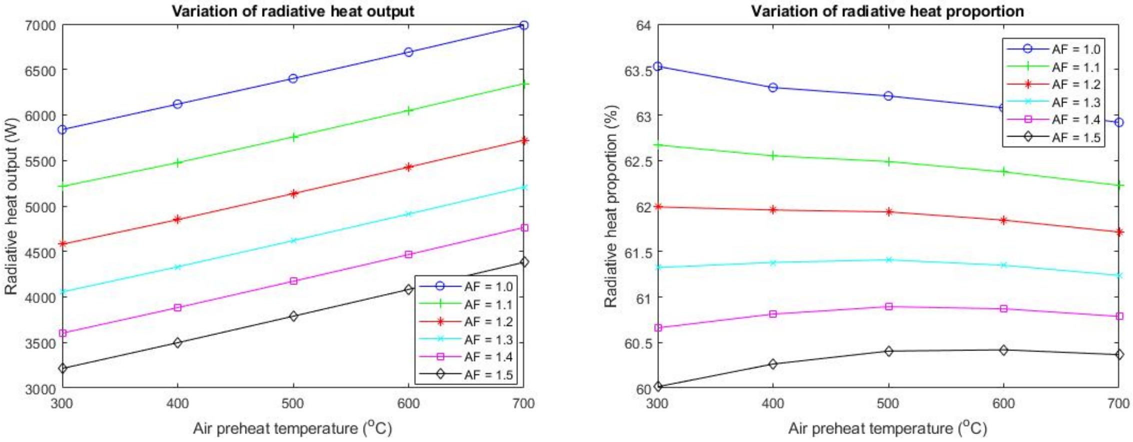

(a) Variation of radiative heat output

(b) Variation of radiative heat proportion

Figure 5.9: Radiative heat transfer in C80-C100 burner-tube assembly

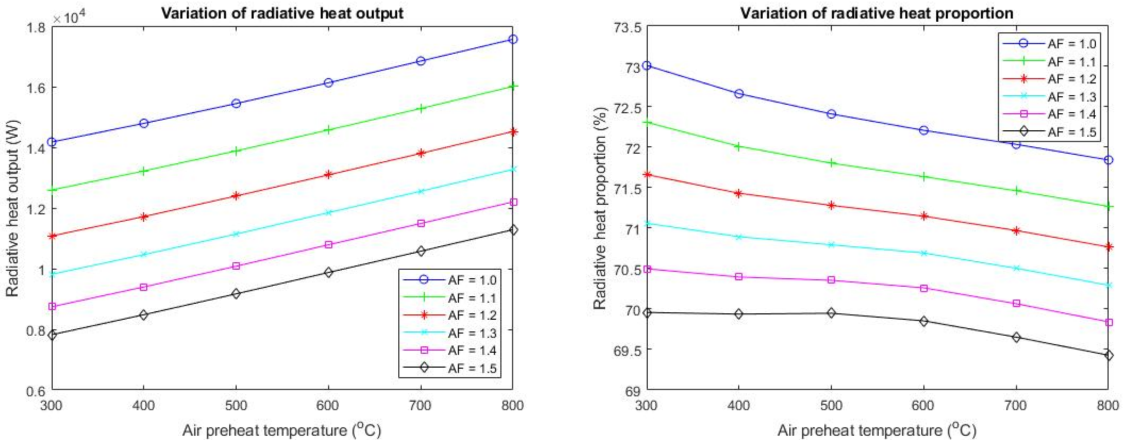

(a) Variation of radiative heat output (b) Variation of radiative heat proportion

Figure 5.10: Radiative heat transfer in C100-C150 burner-tube assembly

5.2.6. RADIANT TUBE EFFICIENCY

The goal of designing any component, system or process is to maximise its efficiency. The same applies to our radiant tube setup as well. As mentioned previously, one of the objectives of this thesis has been to assess the efficiency of both the burner-tube assemblies and study its variation. As shown in Figure (4.1), the hot combusting gases flow over the burner and heat the air flowing inside. This portion forms the passage of the flow after the region marked "Outlet" in Figure (4.4). Therefore, the outlet flow and inlet air form a counter-flow concentric tube heat exchanger. The assumption involved here is that this heat exchanger is 100% efficient. The efficiency of the burner-tube assembly is then defined as follows:

$$\eta = 1 - \frac{\dot{Q}_{loss}}{\dot{Q}_{source}} \tag{5.3}$$

where $\dot{Q}_{loss}$ is the power loss via the "Exhaust" stream marked in Figure (4.1) and $\dot{Q}_{source}$ is the reaction heat source in the radiant tube. The reaction heat source is constant with air preheat temperature and decreasing with air factor. The incoming air from the supply pipes has a small finite enthalpy which increases as it passes through the burner. The difference between the air supply enthalpy and air inlet enthalpy into the computational domain (called air preheat power ($\dot{Q}_{preheat}$)) is subtracted from the outgoing power via the "Outlet" (Figure (4.4)) to get the power loss ($\dot{Q}_{loss}$).

$$\dot{Q}_{preheat} = \dot{Q}_{inlet} - \dot{Q}_{supply} \tag{5.4}$$

$$\dot{Q}_{loss} = \dot{Q}_{Outlet} - \dot{Q}_{preheat} \tag{5.5}$$

As shown in Figure (5.11), the efficiency decreases with air factor. This can be attributed to the fact that the reaction heat source decreases with air factor, which leads to increase in the negative fraction of Equation (5.3). The efficiency is found to increase with increasing air preheat temperature. This can be explained by re-writing Equation (5.3) after substituting Equations (5.4) and (5.5):

$$\eta = 1 - \frac{\dot{Q}_{outlet} - \dot{Q}_{inlet} + \dot{Q}_{supply}}{\dot{Q}_{source}} \tag{5.6}$$

The supply enthalpy ($\dot{Q}_{supply}$) from the air source remains constant as the supply pressure and temperature are fixed. The air inlet power into the computational domain $\dot{Q}_{inlet}$ increases with increasing preheat temperature. The outgoing power from the computational domain $\dot{Q}_{outlet}$ has been found to remain almost constant with air factor and preheat temperature as shown in Figure (5.12). These factors contribute to the increase of efficiency with air preheat temperature.

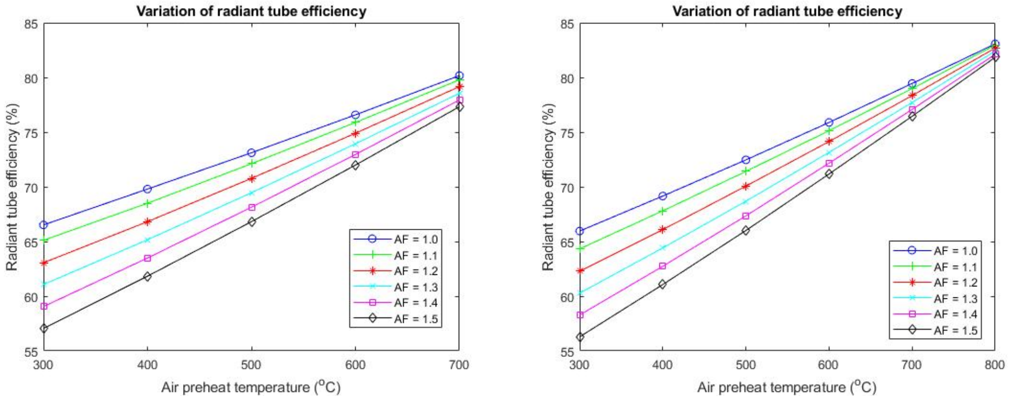

(a) C80-C100 burner-tube assembly

(b) C100-C150 burner-tube assembly

Figure 5.11: Radiant tube efficiency

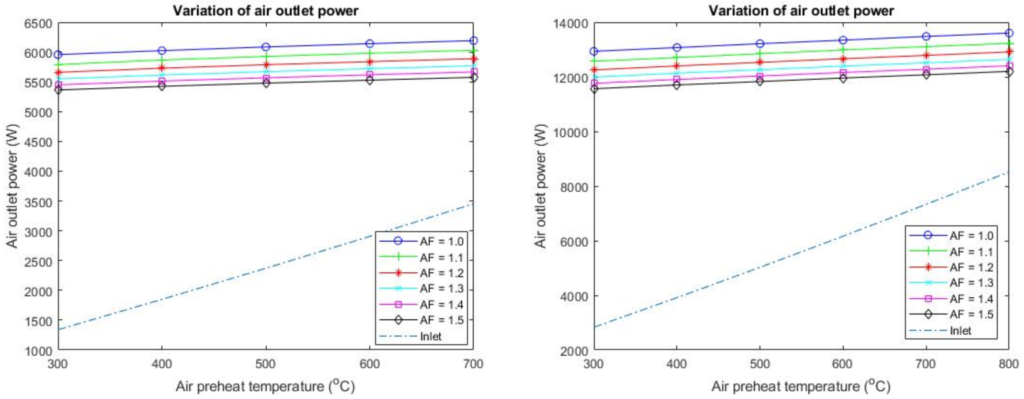

(a) C80-C100 burner-tube assembly

(b) C100-C150 burner-tube assembly

Figure 5.12: Air outlet power

5.2.7. FUEL CONSUMPTION AND WASTAGE

It is one of the primary goals of any burner designer to reduce the wastage of fuel to a minimum, so is it one of the objectives of this thesis as well. However, it has been found from the calculations that the maximum fuel wastage is incurred for stoichiometric mixture. This serves as a deterrent to using the assemblies at stoichiometric ratio. The variation of methane fraction at outlet for both the assemblies is shown in Figure (5.13). The maximum wastage is at stoichiometric ratio, followed by other lean mixtures which are relatively constant. This problem can also be depicted by the oxygen fraction at the outlet, shown in Figure (5.14). The least oxygen outlet is for stoichiometric mixture, as it should be, but not a positive number. It must also be noted that the difference between stoichiometric and other lean mixtures is of couple of orders of magnitude. The problem is compounded by the fact that the reaction rate is maximum for stoichiometric mixture and gradually decreases for lean mixtures, as shown in Figure (5.15). However, it can be explained by the fact that the residence time is minimum for stoichiometric mixture and gradually increases for lean mixtures, as shown in Figure (5.16). This is because the velocity is maximum for stoichiometric mixtures and gradually decreases for lean mixtures. As the reaction time for fluid particles increases, the reaction goes towards completion and the maximum temperature also increases. Hence, the problem of fuel wastage can be solved by operating the assemblies at lean conditions

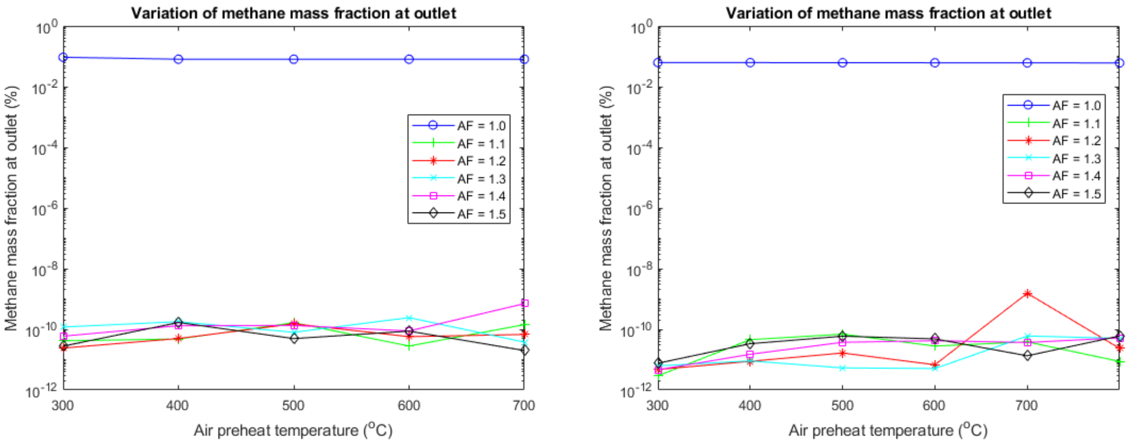

(a) C80-C100 burner-tube assembly (b) C100-C150 burner-tube assembly

Figure 5.13: Methane fraction at outlets

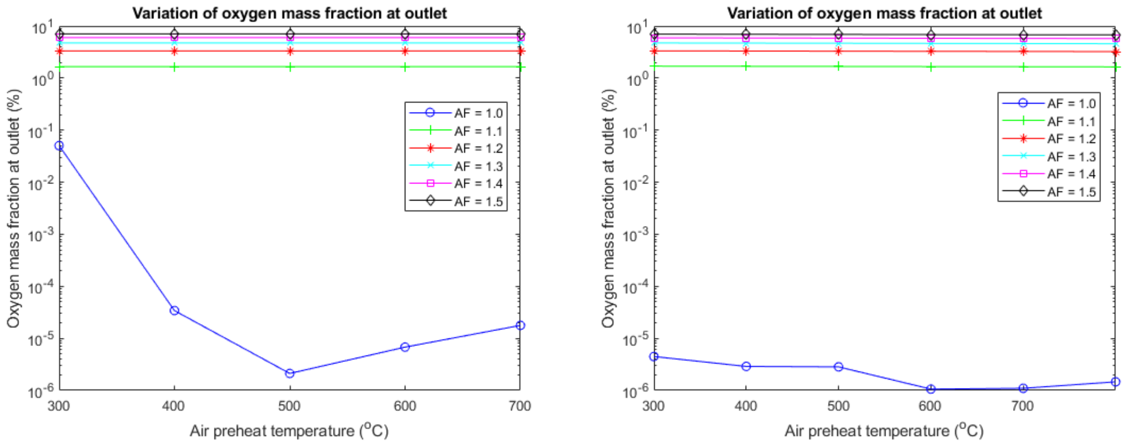

(a) C80-C100 burner-tube assembly (b) C100-C150 burner-tube assembly

Figure 5.14: Oxygen fraction at outlets

5.3. GRID DEPENDENCE TEST RESULTS

An important aspect of any CFD analysis is to check the variation of the results with mesh size. If the variation is scientifically within acceptable limits, then the results are considered acceptable themselves. This section presents the variation of results with mesh size for both burner-tube assemblies. According to company specifications, the exhaust gas must contain 2-5% O_2 by mass. According to stoichiometric calculations, this is achieved at air factor 1.2, with O_2 level being just under 2% for 1.1 and just over 5% for 1.3. Hence, the calculations have been performed for air factor 1.2 at all air preheat temperatures. The computational domain is the same as described in the previous chapter and four different mesh sizes have been tested upon. The meshes thus generated have been named as "Coarser", "Coarse", "Medium" and "Fine" mesh. The details of these four have been tabulated in Tables (5.5) and (5.6). The mesh for both the assemblies involves mostly quadrilateral elements, approximately square in shape. Hence, the cell and orthogonal quality are near unity and skewness is near zero. It must be noted that the values reported in the tables are the average values of the respective parameters. The cell and orthogonal quality indicate of the idealness of the cell shapes. For a triangular cell, the ideal shape is an equilateral triangle and for a quadrilateral cell, the ideal shape is equiangular. Skewness indicates of the deviation of cells from ideal shape.

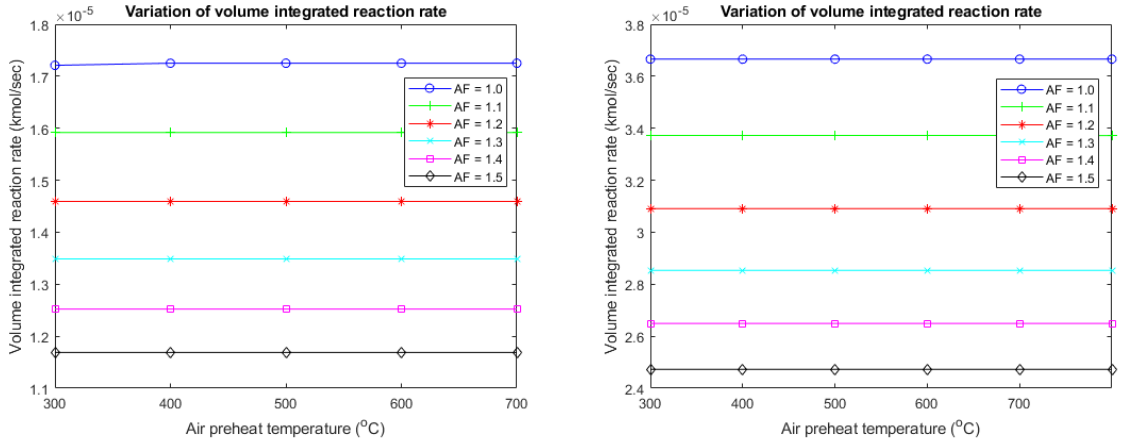

(a) C80-C100 burner-tube assembly (b) C100-C150 burner-tube assembly

Figure 5.15: Reaction rates for both assemblies

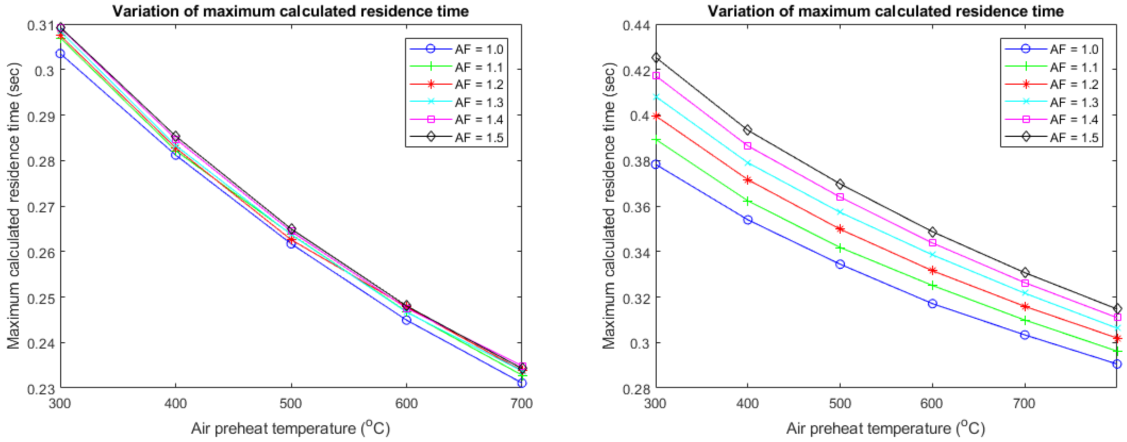

(a) C80-C100 burner-tube assembly (b) C100-C150 burner-tube assembly

Figure 5.16: Residence time for both assemblies

Table (5.4) shows the generally accepted spectrum of these mesh metrics.

Table 5.4: Acceptable mesh metric spectrum

Quality Parameter	Excellent	Very good	Good	Acceptable	Bad	Inacceptable
Cell Quality	0.98-1.00	0.70-0.95	0.20-0.69	0.15-0.20	0.001-0.14	0.000-0.001
Orthogonal Quality	0.98-1.00	0.70-0.95	0.20-0.69	0.15-0.20	0.001-0.14	0.000-0.001
Skewness	0.00-0.25	0.25-0.50	0.50-0.80	0.80-0.94	0.95-0.97	0.98-1.00

The calculations for "Fine" mesh have been performed differently than for the other three meshes. Since the element size is smallest, the ‘Enhanced Wall Treatment’ approach offered by ANSYS® Fluent has been chosen. This involves integrating the conservation equations right upto the wall, without the need for any wall functions. Owing to the small size of the cells and their relatively large number, this method is expected to produce accurate results as the number of cells are assumed to be large enough to accurately capture the large gradients of velocity, temperature, species and other flow properties. The results of the calculations have been presented in Figures (5.17) to (5.22).

The results for C80-C100 setup show quite some variation with different meshes. For this setup, the

Table 5.5: C80 Mesh Details

Mesh	Element Size (mm)	No. of Cells	No. of Nodes	Cell Quality	Orthogonal Quality	Skewness
Coarser	1.00	38253	39151	0.99879	0.99990	8.3502e-4
Coarse	0.75	68324	69524	0.99808	0.99991	1.5632e-3
Medium	0.50	152403	154191	0.99867	0.99994	9.8710e-4
Fine	0.30	423048	426043	0.99884	0.99995	7.7601e-4

Table 5.6: C100 Mesh Details

Mesh	Element Size (mm)	No. of Cells	No. of Nodes	Cell Quality	Orthogonal Quality	Skewness
Coarser	1.25	55266	56347	0.99856	0.99989	1.0317e-3
Coarse	1.00	87568	88920	0.99880	0.99990	7.8566e-4
Medium	0.75	153507	155297	0.99800	0.99991	1.7979e-3
Fine	0.50	350111	352813	0.99899	0.99994	5.7019e-4

"Coarser", "Coarse" and "Medium" meshes produce similar results but the "Fine" mesh produces distinctly different results. The maximum relative variation can be seen in the velocity plots, approximately 8% for least air preheat, but decreases with increasing air preheat. Although the variation in the temperature and heat output is not more than 5% for all the cases, the "Fine" mesh results can be distinctly seen from the others. This distinction is more prominent for the variation in radiative heat proportion. Another observation to be made is that the maximum calculated temperature values for "Fine" mesh cut through all the other mesh values. Similar behaviour is observed for velocity values as well. This departure of the "Fine" mesh results from other three can be attributed to the use of ‘Enhanced Wall Treatment’ for "Fine" mesh and standard wall functions for other three.

The variation in the results for C100-C150 setup is less as compared to C80-C100 setup, although the "Fine" mesh results can be distinctly seen in this case as well. This difference in the variation between both setups may be attributed to the difference in increase in the number of cells from "Coarser" to "Fine" mesh. The number of cells increases by almost 11 times for C80-C100 setup but only by 6 times for C100-C150 setup. Thus, if the mesh for C100-C150 setup is further refined, the results may be similar to that obtained for C80-C100 setup.

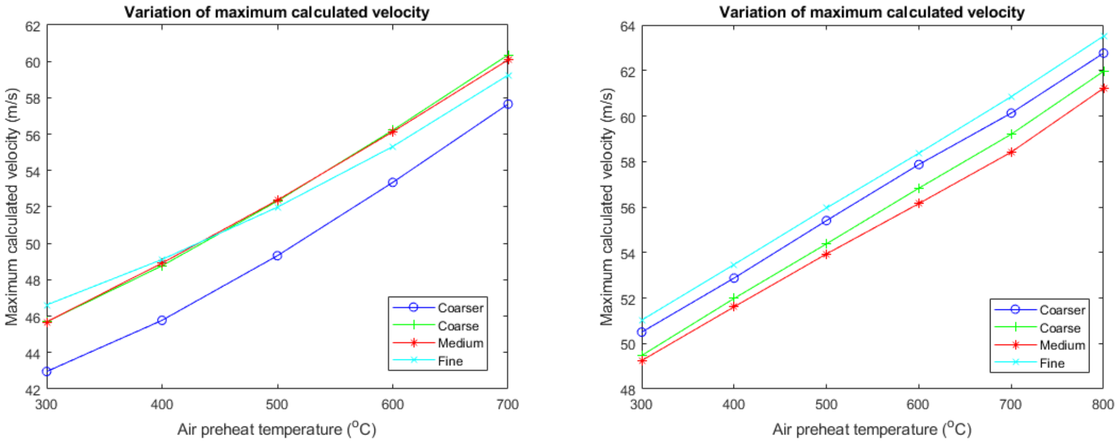

(a) C80-C100 burner-tube assembly

(b) C100-C150 burner-tube assembly

Figure 5.17: Maximum velocity comparison

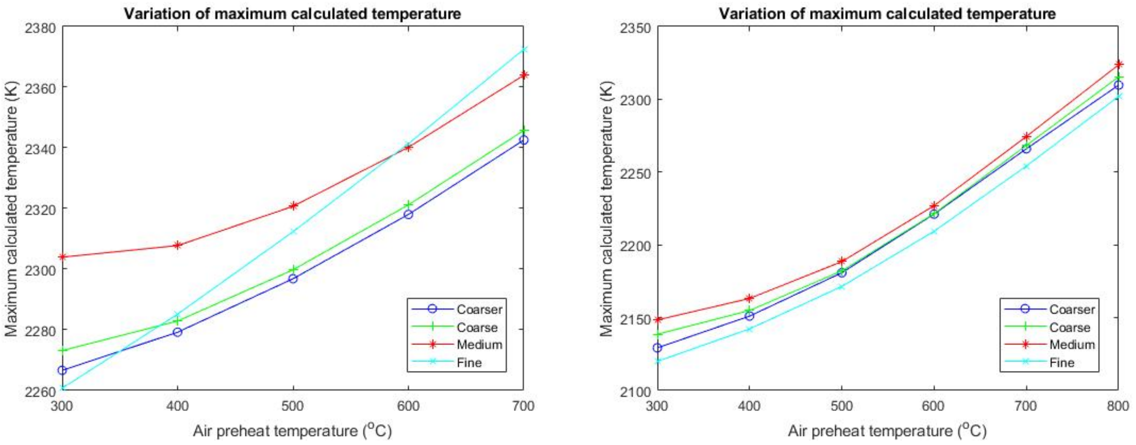

(a) C80-C100 burner-tube assembly

(b) C100-C150 burner-tube assembly

Figure 5.18: Maximum temperature comparison

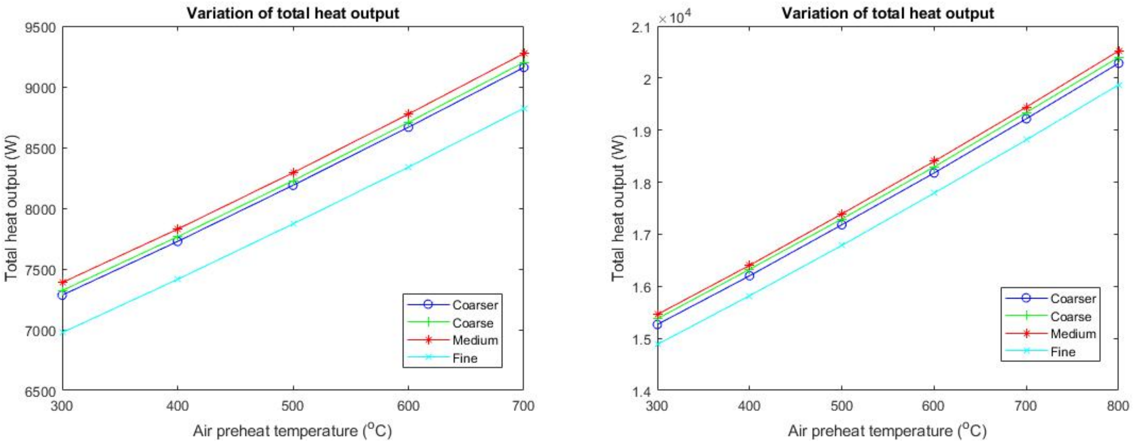

(a) C80-C100 burner-tube assembly

(b) C100-C150 burner-tube assembly

Figure 5.19: Heat output comparison

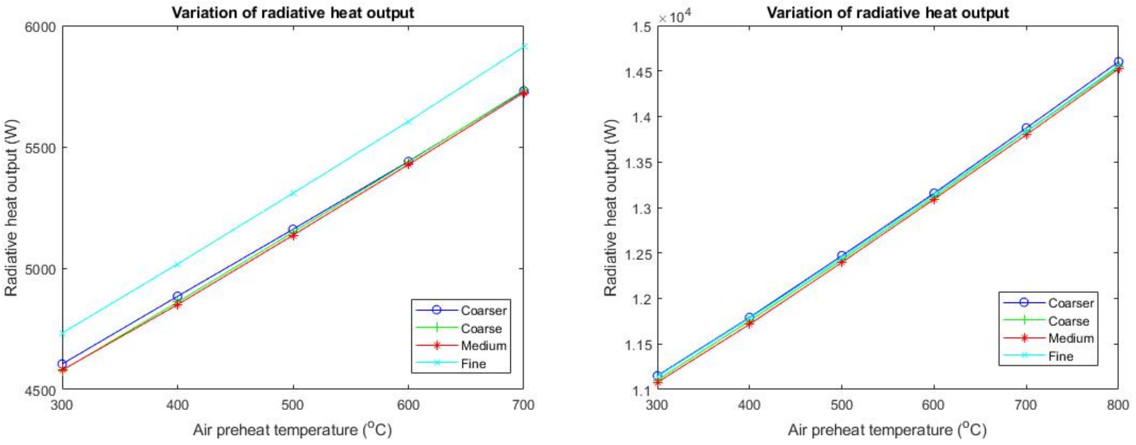

(a) C80-C100 burner-tube assembly

(b) C100-C150 burner-tube assembly

Figure 5.20: Radiative heat comparison

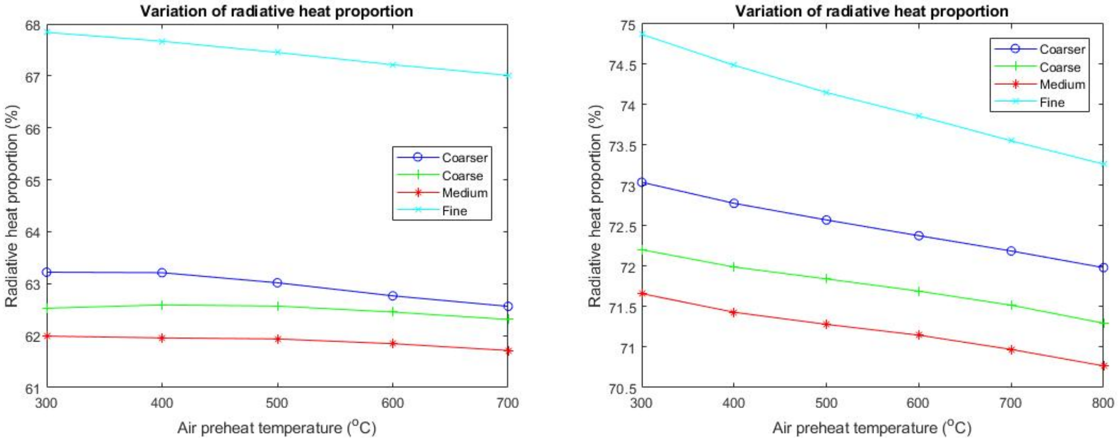

(a) C80-C100 burner-tube assembly (b) C100-C150 burner-tube assembly

Figure 5.21: Radiative proportion comparison

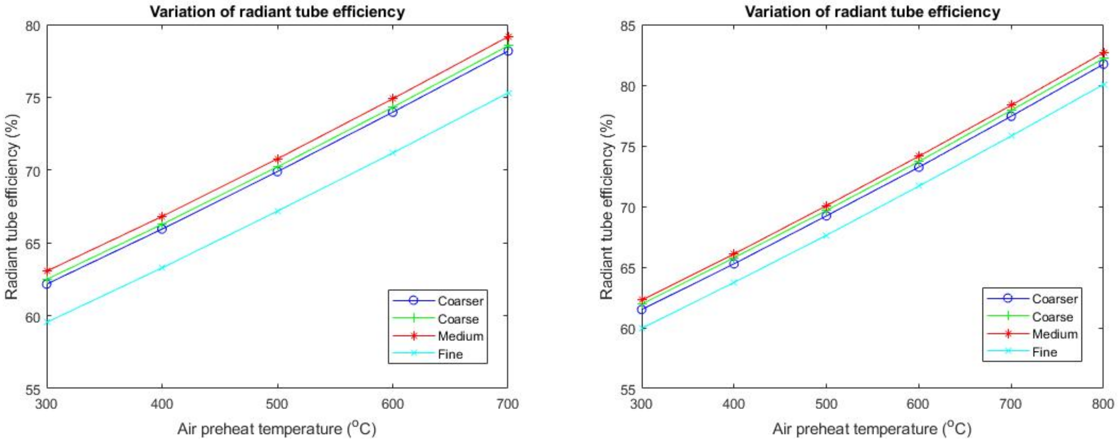

(a) C80-C100 burner-tube assembly (b) C100-C150 burner-tube assembly

Figure 5.22: Radiant tube efficiency comparison

6

CONCLUSIONS AND RECOMMENDATIONS

The results of all the calculations have been reported and have been checked for their sensitivity to mesh size. This chapter presents the conclusions drawn from the analysis of both the burner-tube assemblies and the scope of further research on the equipment to understand its working better.

6.1. CONCLUSIONS

As mentioned previously, the main objective of this thesis was to analyse the variation of heat output and various related quantities with mixture stoichiometry and air preheat for both the burner-tube assemblies. The motivation behind this study was to select the optimum operating condition for the equipment. After studying all the results presented in the previous chapter, we can conclude the following:

- **Operating conditions**: In terms of heat output and efficiency, both the setups must be operated at stoichiometric condition with maximum air preheat. However, as mentioned in the previous chapter, the equipment must be operated at lean condition of air factor 1.2, which will lead to reduction in both heat output and efficiency. The loss of heat output is more prominent than that of efficiency. At maximum air preheat, the power loss for C80-C100 setup is around 2000 W and that for C100-C150 burner is around 4000 W.

- **Less fuel wastage**: An advantage of using the equipment at lean condition rather than at stoichiometry is the reduction in wastage of fuel. As explained in the previous chapter, the wastage of fuel is found maximum at stoichiometric ratio. The outlet stream contains maximum methane mass fraction for both the setups. This is only considering the simulation fuel. The actual loss using natural gas is expected to be more than 0.06%.

- **Grid independence**: The grid dependence test hasn't shown much deviation with grid size for all preheat temperatures. The maximum calculated deviation is of temperature for C80-C100 setup, a value approximately 1.75%, which is within scientifically acceptable limits. Hence, it may be concluded that the simulations are robust enough at this level.

6.2. RECOMMENDATIONS

The calculations performed in this thesis only give a rough estimate of the operation of the equipment. Hence, there is much scope of further research to properly understand the working of the equipment. This research may be divided into two categories: improvements in CFD calculation and experimental validation of CFD results.

6.2.1. CFD IMPROVEMENTS

A lot of simplifying assumptions were made while conducting the calculations in this thesis. The next logical step is to examine the validation of each assumption and model the reality as accurately as possible. The following steps may be taken to improve the CFD calculations:

- **Geometry and mesh improvement**: A proper 3D model must be made for analysing the effect of the protrusions of the ceramic tube on the flow and heat transfer. However, such a model would require an extremely fine mesh, well beyond the capabilities of ANSYS® Academic version. Hence, other softwares can be used which don't impose such restrictions.

- **Use of detailed chemical mechanism**: This thesis involves the use of the single step chemical mechanism for methane combustion. However, the actual combustion process takes place in multiple steps as a lot of intermediates are involved. These intermediates are expected to affect the maximum temperature achieved, as they do for hydrogen combustion [60]. Hence, the use of a proper multi-step mechanism will improve the results as the flame chemistry has a huge impact on the turbulence levels.

- **Accurate turbulence prediction**: As mentioned in section (4.2), the flow is transitioning towards turbulence. However, the standard $k-\varepsilon$ turbulence model with standard wall functions was used to model turbulence in both the burner-tube assemblies. The use of an appropriate low-Reynolds number model would yield accurate results as turbulence also has a huge impact on the flame structure. Also, the use of a fine mesh would enable the analysis of the near wall flow without any wall functions, using direct integration of the conservation equations right upto the wall.

- **Pollutant prediction**: As the environmental regulations become increasingly stringent, the main goal for combustion systems design will be to reduce pollutant formation. So is the case for these burner-tube assemblies as well. An accurate prediction of various pollutants is necessary to control their formation.

- **Accurate analysis of air preheat**: This thesis assumes the incoming air to be at the required preheat temperature by simply using the appropriate boundary condition at air inlet as shown in Figure (4.4). However, in practice, the air preheat is controlled by the flow of exhaust gases over the burner containing the incoming air. This heat exchange will not be 100% accurate as assumed in this thesis. Hence, proper analysis of this heat exchange is necessary to accurately predict the air preheat.

- **Heat transfer outside the radiant tube**: A major shortcoming of this thesis is the use of constant temperature boundary condition at the outer wall. This is due to the lack of the knowledge about the heat transfer mechanism from the radiant tube to the fluidised bed. An accurate knowledge about that mechanism would greatly help in analysing the heat transfer from the radiant tube as the appropriate boundary conditions would then be known.

- **Use of proper material properties**: As mentioned in section (4.6), the exact properties for both the materials used in the tubes have not been used, only interpolated estimates from similar materials. Hence, the knowledge of exact material properties would further enhance the accuracy of the results.

- **Use of natural gas composition**: The exact composition of natural gas is not used for calculations in this thesis, only methane (CH_4) as the combustible gas with two inert gases. This was done to simplify the chemical mechanism to a single step and to avoid the calculations for higher hydrocarbons. The next step would be use the exact composition of Dutch Natural Gas. The use of detailed chemical mechanism would enable such calculations.

The most important recommendations with their priority levels have been given in Table (6.1). The other recommendations may be considered as subsets of these main recommendations. For instance, the use of a detailed chemical mechanism would automatically enable the use of actual natural gas composition, as higher hydrocarbons have been considered in such detailed mechanisms. The use of such accurate mechanisms would automatically result in accurate temperature predictions, which would indirectly also control the pollutant predictions. Also, if the accurate boundary conditions are used for outer wall, the total heat transfer from the radiant tubes will be properly predicted and the outgoing power (from 'Outlet' in Figure (4.4)) will be controlled. Hence, it would prove beneficial in analysing the air preheat.

Table 6.1: Important recommendations

Priority	**Recommendation**	**Details**
1.	Geometry and mesh improvement	Use 3D model and the finest mesh possible
2.	Detailed chemical mechanism	Use proper mechanism with intermediates
3.	Accurate turbulence prediction	Use an appropriate low-Re model without wall functions
4.	Accurate heat transfer prediction	Analyse heat transfer from radiant tube to fluidised bed for appropriate boundary condition at outer wall

6.2.2. EXPERIMENTAL VALIDATION

Even the most sophisticated CFD analysis will only give a numerical estimate of the required parameters. Without experimental validation, the results provided by any CFD analysis are just numbers, which may be presented in a colourful fashion. Hence, the most important step towards a proper understanding of any phenomenon is to validate the CFD results with experimental data. With the availability of precisely measured experimental data, various numerical models may be validated. In case of any disagreement between numerical and experimental data, other appropriate numerical models may be chosen or developed for further use.

The validation of any CFD results for radiant tube heaters would consist of comparing the temperature, species and velocity fields against experimental data. The following steps may be taken to validate any such CFD analysis in an orderly fashion:

- **Temperature validation**: It is the easiest way to validate any CFD analysis. Comparing the experimentally measured temperature values with calculated values provides a good estimate of the accuracy of the calculations. As explained in a previous chapter, each inner flame tube has distinct protrusions along its circumference. These protrusions can be used to fix thermocouples for temperature measurements. Further, more sophisticated techniques like Na-Line-Reversal method, CARS spectroscopy and Laser-induced Fluorescence may be used for accurate measurements.

- **Exhaust gas validation**: It involves the analysis of the exhaust gas and use the data to validate the calculated exhaust mixture. Pollutant predictions can also be validated using the exhaust gas data. It must be noted that if the temperature predictions are accurate, the pollutant predictions are expected to be accurate as well.

- **Velocity validation**: It involves comparing the measured the velocity values to calculated values. Since velocity measurements inside a closed cylindrical tube are difficult, only relatively crude instruments like hot-wire anemometer can be used. The use of such instruments at various points may give some estimate of the velocity field, which can then be used for validation.

However, it must be noted that the most accurate understanding of any phenomenon would always include the two-way interaction between numerical and experimental data. As the experimental techniques become sophisticated, advanced numerical modelling may be required for predictions. Similarly, as the numerical data becomes precise, its accuracy must be checked with advanced measurement techniques. For example, the accurate prediction of velocity and temperature fields using DNS approach may require extremely sophisticated data recorded in real time which includes temporal variation, and vice versa as well.

BIBLIOGRAPHY

[1] M D Ahanj, M Rahimi, and A A Alsairafi. “CFD modeling of a radiant tube heater”. In: *International Communications in Heat and Mass Transfer* 39.3 (2012), pp. 432–438.

[2] ANSYS®. *ANSYS Fluent Theory Guide*. 2013.

[3] P Basu. *Biomass gasification, pyrolysis and torrefaction: practical design and theory*. Academic press, 2018.

[4] T L Bergman et al. *Introduction to heat transfer*. John Wiley & Sons, 2011.

[5] C T Bowman et al. *GRI 2.11 Mechanism homepage*. URL: `http://combustion.berkeley.edu/gri-mech/new21/version21/text21.html` (visited on 08/14/2018).

[6] R C Brown. *Thermochemical processing of biomass: conversion into fuels, chemicals and power*. John Wiley & Sons, 2011.

[7] S Chandrasekhar. “Radiative heat transfer”. In: *Dover Publications, New York, USA* 11 (1960), pp. 11–12.

[8] W C Chang and J Y Chen. *Reduced Mechanisms based on GRI-Mech 1.2*. URL: `http://firebrand.me.berkeley.edu/griredu.html` (visited on 08/14/2018).

[9] J Y Chen. “Development of reduced mechanisms for numerical modelling of turbulent combustion”. In: *Workshop on Numerical Aspects of Reduction in Chemical Kinetics*. CERMICS-ENPC Cite Descartes Champus sur Marne, France. 1997.

[10] E H Chui and G D Raithby. “Computation of radiant heat transfer on a nonorthogonal mesh using the finite-volume method”. In: *Numerical Heat Transfer* 23.3 (1993), pp. 269–288.

[11] E H Chui, G D Raithby, and P M J Hughes. “Implementation of the finite volume method for calculating radiative transfer in a pulverized fuel flame”. In: *Combustion Science and Technology* 92.4-6 (1993), pp. 225–242.

[12] E H Chui, G D Raithby, and P M J Hughes. “Prediction of radiative transfer in cylindrical enclosures with the finite volume method”. In: *Journal of Thermophysics and Heat transfer* 6.4 (1992), pp. 605–611.

[13] P J Coelho and M G Carvalho. “A conservative formulation of the discrete transfer method”. In: *Journal of Heat Transfer* 119.1 (1997), pp. 118–128.

[14] A Coppalle and P Vervisch. “The total emissivities of high-temperature flames”. In: *Combustion and Flame* 49.1-3 (1983), pp. 101–108.

[15] M K Denison and B W Webb. “A spectral line-based weighted-sum-of-gray-gases model for arbitrary RTE solvers”. In: *Journal of Heat Transfer* 115.4 (1993), pp. 1004–1012.

[16] E Effelsberg and N Peters. “Scalar dissipation rates in turbulent jets and jet diffusion flames”. In: *Symposium (International) on Combustion*. Vol. 22. 1. Elsevier. 1989, pp. 693–700.

[17] *EN 1.4852 (GX40NiCrSiNb35-26) Cast Stainless Steel*. URL: `www.makeitfrom.com/material-properties/EN-1.4852-GX40NiCrSiNb35-26-Cast-Stainless-Steel` (visited on 05/23/2018).

[18] B Franzelli et al. “Large eddy simulation of combustion instabilities in a lean partially premixed swirled flame”. In: *Combustion and flame* 159.2 (2012), pp. 621–637.

[19] M Frenklach et al. *GRI 1.2 Mechanism homepage*. URL: `http://combustion.berkeley.edu/gri_mech/new21/version12/text12.html` (visited on 08/14/2018).

[20] M Frenklach et al. *GRI-Mech–An Optimized Detailed Chemical Reaction Mechanism for Methane Combustion*. Tech. rep. Gas Research Institute, 1995.

[21] T M Geerssen. *Physical Properties of Natural Gases*. N.V. Nederlandse Gasunie, 1980.

[22] P Glarborg et al. “Kinetic modeling of hydrocarbon/nitric oxide interactions in a flow reactor”. In: *Combustion and flame* 115.1-2 (1998), pp. 1–27.

[23] I R Gran and B F Magnussen. “A numerical study of a bluff-body stabilized diffusion flame. Part 2. Influence of combustion modelling and finite-rate chemistry”. In: *Combustion Science and Technology* 119.1-6 (1996), pp. 191–217.

[24] J R Howell and M Perlmutter. “Monte Carlo solution of radiant heat transfer in a nongrey nonisothermal gas with temperature dependent properties”. In: *AIChE Journal* 10.4 (1964), pp. 562–567.

[25] D J Hyde and J S Truelove. “The discrete ordinates approximation for multidimensional radiant heat transfer in furnaces”. In: *AERE R-8502, AERE Harwell, UK* (1977).

[26] F K Jäger et al. “CFD modelling of a radiant tube burner for liquid and gaseous fuels”. In: *Progress in Computational Fluid Dynamics, an International Journal* 5.7 (2005), pp. 406–413.

[27] W P Jones and R P Lindstedt. “Global reaction schemes for hydrocarbon combustion”. In: *Combustion and flame* 73.3 (1988), pp. 233–249.

[28] W P Jones and J H Whitelaw. “Calculation methods for reacting turbulent flows: a review”. In: *Combustion and flame* 48 (1982), pp. 1–26.

[29] W de Jong and J R van Ommen. *Biomass as a Sustainable Energy Source for the Future: Fundamentals of Conversion Processes.* AiChE-Wiley, 2015.

[30] C E Baukal Jr. *Industrial Burners Handbook.* CrC press, 2004.

[31] A Kazakov and M Frenklach. *DRM Mechanisms homepage.* URL: `http://www.me.berkeley.edu/drm/` (visited on 08/14/2018).

[32] S E Kim, D Choudhury, and B Patel. “Computations of complex turbulent flows using the commercial code FLUENT”. In: *Modeling complex turbulent flows.* Springer, 1999, pp. 259–276.

[33] S W Kim. “Calculation of divergent channel flows with a multiple-time-scale turbulence model”. In: *AIAA journal* 29.4 (1991), pp. 547–554.

[34] A Y Klimenko and R W Bilger. “Conditional moment closure for turbulent combustion”. In: *Progress in energy and combustion science* 25.6 (1999), pp. 595–687.

[35] H A M Knoef. *Handbook Biomass Gasification.* Enschede, The Netherlands: Biomass Technology Group, 2012.

[36] A N Kolmogorov. “The Local Structure of Turbulence in Incompressible Viscous Fluid for Very Large Reynolds’ Numbers”. In: *Akademiia Nauk SSSR Doklady* 30 (1941), pp. 301–305.

[37] P K Kundu, I M Cohen, and D R Dowling. *Fluid Mechanics.* Academic Press, 2015.

[38] C K G Lam and K A Bremhorst. “A Modified Form of the k-ε Model for Predicting Wall Turbulence”. In: *Journal of Fluids Engineering* 103.3 (1981), pp. 456–460.

[39] K D Lathrop and B G Carlson. *Discrete ordinates angular quadrature of the neutron transport equation.* Tech. rep. Los Alamos Scientific Lab., N. Mex., 1964.

[40] B E Launder and D B Spalding. *Lectures in Mathematical Models of Turbulence.* England: Academic Press, 1972.

[41] F C Lockwood and N G Shah. “A new radiation solution method for incorporation in general combustion prediction procedures”. In: *Symposium (international) on combustion.* Vol. 18. 1. Elsevier. 1981, pp. 1405–1414.

[42] Anne Loppinet-Serani, Cyril Aymonier, and François Cansell. “Current and foreseeable applications of supercritical water for energy and the environment”. In: *ChemSusChem: Chemistry & Sustainability Energy & Materials* 1.6 (2008), pp. 486–503.

[43] T Lu and C K Law. “A criterion based on computational singular perturbation for the identification of quasi steady state species: A reduced mechanism for methane oxidation with NO chemistry”. In: *Combustion and Flame* 154.4 (2008), pp. 761–774.

[44] B Magnussen. “On the structure of turbulence and a generalized eddy dissipation concept for chemical reaction in turbulent flow”. In: *19th Aerospace Sciences Meeting.* 1981, p. 42.

[45] B F Magnussen and B H Hjertager. “On mathematical modeling of turbulent combustion with special emphasis on soot formation and combustion”. In: *Symposium (international) on Combustion.* Vol. 16. 1. Elsevier. 1977, pp. 719–729.

[46] T Mendiara et al. “An augmented reduced mechanism for methane combustion”. In: *Energy & fuels* 18.3 (2004), pp. 619–627.

[47] F R Menter. “Eddy viscosity transport equations and their relation to the $k-\varepsilon$ model”. In: *Journal of fluids engineering* 119.4 (1997), pp. 876–884.

[48] F R Menter. “Improved Two-Equation $k-\varepsilon$ Turbulence Models for Aerodynamic Flows”. In: *NASA Technical Memorandum* 103975 (1992).

[49] F R Menter. “Performance of popular turbulence model for attached and separated adverse pressure gradient flows”. In: *AIAA journal* 30.8 (1992), pp. 2066–2072.

[50] F R Menter. “Two-equation eddy-viscosity turbulence models for engineering applications”. In: *AIAA journal* 32.8 (1994), pp. 1598–1605.

[51] F R Menter, M Kuntz, and R Langtry. “Ten years of industrial experience with the SST turbulence model”. In: *Turbulence, Heat and Mass Transfer* 4.1 (2003), pp. 625–632.

[52] T A Milne, R J Evans, and N Abatzaglou. *Biomass gasifier”Tars”: their nature, formation, and conversion.* Tech. rep. National Renewable Energy Laboratory, Golden, CO (US), 1998.

[53] M F Modest. *Radiative Heat Transfer.* Academic press, 2013.

[54] M F Modest. “The weighted-sum-of-gray-gases model for arbitrary solution methods in radiative transfer”. In: *Journal of heat transfer* 113.3 (1991), pp. 650–656.

[55] A A Msaad et al. “Reduced detailed mechanism for methane combustion”. In: *Energy and Power Engineering* 4.01 (2012), p. 28.

[56] V C Patel, W Rodi, and G Scheuerer. “Turbulence Models for Near-Wall and Low Reynolds Number Flows: A Review”. In: *AIAA journal* 23.9 (1985), pp. 1308–1319.

[57] N Peters. “Laminar diffusion flamelet models in non-premixed turbulent combustion”. In: *Progress in energy and combustion science* 10.3 (1984), pp. 319–339.

[58] B S Petukhov. “Heat transfer and friction in turbulent pipe flow with variable physical properties”. In: *Advances in heat transfer.* Vol. 6. Elsevier, 1970, pp. 503–564.

[59] H Pitsch, M Chen, and N Peters. “Unsteady flamelet modeling of turbulent hydrogen-air diffusion flames”. In: *Symposium (international) on combustion.* Vol. 27. 1. Elsevier. 1998, pp. 1057–1064.

[60] H Pitsch and N Peters. “A consistent flamelet formulation for non-premixed combustion considering differential diffusion effects”. In: *Combustion and Flame* 114.1-2 (1998), pp. 26–40.

[61] T Poinsot and D Veynante. *Theoretical and numerical combustion.* RT Edwards, Inc., 2005.

[62] S B Pope. “Computationally efficient implementation of combustion chemistry using in-situ adaptive tabulation”. In: *Combustion Theory and Modelling* 1.3 (1997), pp. 41–63.

[63] L Prandtl. “Investigations on turbulent flow”. In: *Journal of Applied Mathematics and Mechanics* 5 (1925), p. 136.

[64] R Pritchard, J J Guy, and N E Connor. *Industrial gas utilization: engineering principles and practice.* Bowker Publishing, 1977.

[65] *Reaction Bonded Silicon Carbide.* URL: `www.makeitfrom.com/material-properties/Reaction-Bonded-Silicon-Carbide` (visited on 05/23/2018).

[66] REN21. *Renewables 2017 Global Status Report.* 2017.

[67] R Sankaran et al. “Structure of a spatially developing turbulent lean methane–air Bunsen flame”. In: *Proceedings of the combustion institute* 31.1 (2007), pp. 1291–1298.

[68] S Sarkar et al. “The analysis and modelling of dilatational terms in compressible turbulence”. In: *Journal of Fluid Mechanics* 227 (1991), pp. 473–493.

[69] G Scribano, G Solero, and A Coghe. “Pollutant emissions reduction and performance optimization of an industrial radiant tube burner”. In: *Experimental Thermal and Fluid Science* 30.7 (2006), pp. 605–612.

[70] T S Shih et al. “A new $k-\varepsilon$ eddy viscosity model for high reynolds number turbulent flows”. In: *Computers & Fluids* 24.3 (1995), pp. 227–238.

[71] G P Smith et al. *GRI 3.0 Mechanism homepage*. URL: http://combustion.berkeley.edu/gri-mech/version30/text30.html (visited on 08/14/2018).

[72] I F Smith, Z F Shen, and J N Friedman. “Evaluation of coefficients for the weighted sum of gray gases model”. In: *Journal of heat transfer* 104.4 (1982), pp. 602–608.

[73] M D Smooke, I K Puri, and K Seshadri. “A comparison between numerical calculations and experimental measurements of the structure of a counterflow diffusion flame burning diluted methane in diluted air”. In: *Symposium (International) on Combustion*. Vol. 21. 1. Elsevier. 1988, pp. 1783–1792.

[74] P R Spalart and S R Allmaras. “A one-equation turbulence model for aerodynamic flows”. In: *30th Aerospace Sciences Meeting and Exhibit*. 1992, p. 439.

[75] N Tsioumanis, J G Brammer, and J Hubert. “Flow processes in a radiant tube burner: Combusting flow”. In: *Energy Conversion and Management* 52.7 (2011), pp. 2667–2675.

[76] N Tsioumanis, J G Brammer, and J Hubert. “Flow processes in a radiant tube burner: Isothermal flow”. In: *Fuel* 87.1 (2008), pp. 103–111.

[77] United Nations, Department of Economic and Social Affairs, Population Division. *World Population Prospects, Key findings and advance tables*. 2015.

[78] United States Energy Information Administration. *International Energy Outlook 2017*. 2017.

[79] H K Versteeg and W Malalasekera. *An Introduction to Computational Fluid Dynamics: The Finite Volume Method*. England: Pearson Education Limited, 2007.

[80] Y Wang et al. “Numerical Simulation of the Thermal Process in a W-Shape Radiant Tube Burner”. In: *JOM* 66.7 (2014), pp. 1253–1264.

[81] D C Wilcox. *Turbulence Modelling for CFD*. DCW Industries, 2006.

[82] V Yakhot et al. “Development of turbulence models for shear flows by a double expansion technique”. In: *Physics of Fluids A: Fluid Dynamics* 4.7 (1992), pp. 1510–1520.

[83] O Zeman. “Dilatation dissipation: the concept and application in modeling compressible mixing layers”. In: *Physics of Fluids A: Fluid Dynamics* 2.2 (1990), pp. 178–188.

A

SIMULATION FUEL COMPOSITION

The fuel used in actual burners in the current setup is Dutch Natural Gas. Besides methane, it contains small amounts of ethane, propane, butane, pentane and hexane. The actual composition is given in Table (A.1) [21]:

Table A.1: Dutch Natural Gas Composition

Component	**CH_4**	**C_2H_6**	**C_3H_8**	**C_4H_{10}**	**C_5H_{12}**	**C_6H_{14}**	**O_2**	**N_2**	**CO_2**
Mass percent	69.97	4.63	0.90	0.47	0.16	0.23	0.02	21.52	2.10
Mole percent	81.29	2.87	0.38	0.15	0.04	0.05	0.01	14.32	0.89

The CFD analysis using such a fuel would be highly complex and time consuming. Hence, some simplification has been done for convenience purposes. It has been assumed that all the heating value of the fuel is contributed only by methane, instead of all the higher hydrocarbons as well. The lower heating value (LHV) of the hydrocarbons is tabulated in Table (A.2) [21]:

Table A.2: LHV of various hydrocarbons

Component	**CH_4**	**C_2H_6**	**C_3H_8**	**C_4H_{10}**	**C_5H_{12}**	**C_6H_{14}**
LHV (MJ/kg)	50.016	47.489	46.357	45.742	45.351	45.105

To arrive at the required composition, we take the following three-step approach:

- Calculate the LHV of fuel using values given in Table (A.2) using the equation below:

$$\Delta H = \sum_{i=1}^{N} \Delta H_i y_i \tag{A.1}$$

  where ΔH_i is the LHV and y_i is the mass fraction of component i.

- Calculate the mass fraction of CH_4, assuming that this simulation fuel has the same heating value as the actual fuel, using the equation below:

$$Y_{CH_4} = \frac{\Delta H}{\Delta H_{CH_4}} \tag{A.2}$$

- Calculate the mass fractions of the remaining inert species (N_2, CO_2 and O_2) assuming the same ratio as the actual fuel using the equation below:

$$Y_j = (1 - Y_{CH_4}) \left[\frac{y_j}{\sum_{j=1}^{M} y_j} \right] \tag{A.3}$$

where Y_j is the simulation mass fraction and y_j is the actual mass fraction of inert species j, M is the number of inert species.

The composition of the simulation fuel is tabulated in Table (A.3):

Table A.3: Simulation fuel composition

Component	**CH_4**	**CO_2**	**N_2**
Mass percent	76.00	2.13	21.87
Mole percent	85.13	0.87	14.00

It must be noted that there are three inert components in the actual fuel (N_2, CO_2 and O_2) but only two in the simulation fuel (N_2 and CO_2), due to the following reasons:

- Since the amount of oxygen was negligible as compared to other two, it is assumed to be non existent during simulations.
- If oxygen is assumed to be present, the type of combustion changes to partially premixed, as opposed to non-premixed. To avoid this situation, oxygen is assumed to be non-existent in the fuel during simulations.

B

VARIATION OF TURBULENCE

As explained in section (5.2.2), the turbulence level of the flow affects the maximum calculated temperature. The variation of velocity, which has already been shown in Figure (5.6), is the first step in understanding the variation in overall turbulence levels. This appendix deals with the analysis of other turbulence parameters and their respective variation.

Two other major parameters to gauge the overall turbulence level of the flow are turbulent kinetic energy (k) and its dissipation rate (ε). The turbulence level is expected to decrease with increasing air factor, thereby reducing the maximum calculated values of k and ε. The variation of both these parameters in both the tubes is shown in Figures (B.1) and (B.2). As can be seen from the figures, the turbulence level does indeed decrease with increasing air factor. The maximum decrease in kinetic energy is approximately 7.5% for C80-C100 setup and approximately 17% for C100-C150 setup. The maximum decrease in turbulent dissipation rate is approximately 20% for C80-C100 setup and approximately 44% for C100-C150 setup. It must be noted that these maximum values have been found for least air preheat temperature for both the setups. As the fluid heats up, the decrease in turbulence with air factor becomes relatively smaller. Thus, it may be concluded that the effect of temperature on turbulence is far greater than that of air factor.

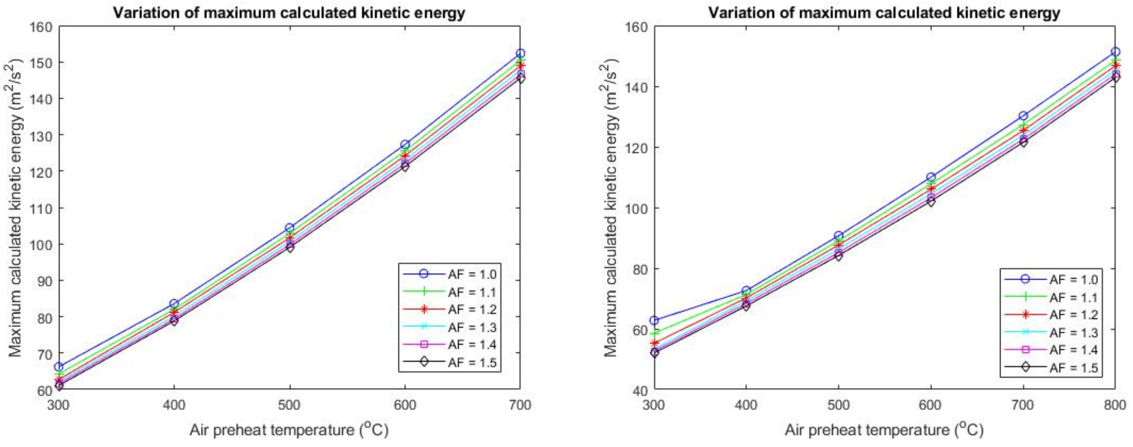

(a) C80-C100 burner-tube setup

(b) C100-C150 burner-tube setup

Figure B.1: Variation of turbulent kinetic energy

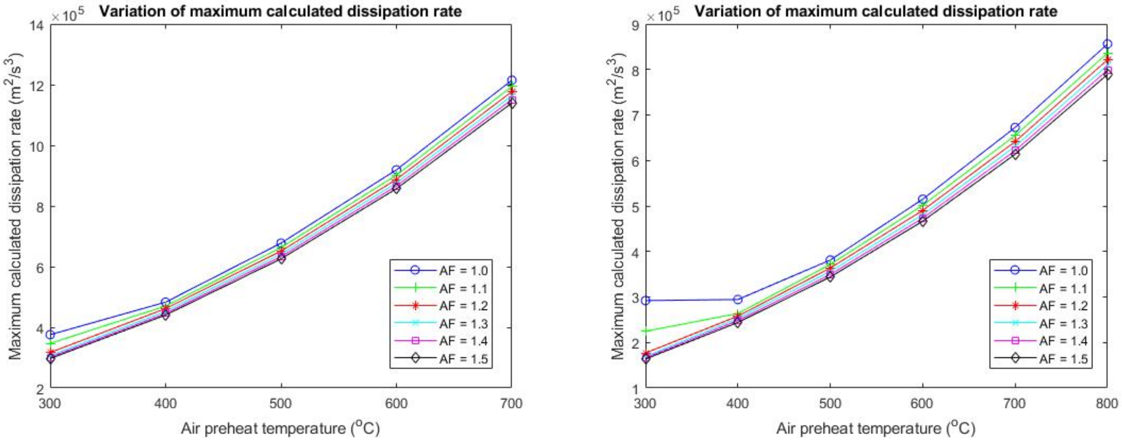

(a) C80-C100 burner-tube setup

(b) C100-C150 burner-tube setup

Figure B.2: Variation of dissipation rate

However, the anomaly observed in temperature values for C80-C100 setup (as mentined in section (5.2.2)) is not reflected in these turbulence variation plots. Hence, the anomaly may indeed be attributed to numerical errors that may have crept up during the calculations.